General Disclaimer

One or more of the Following Statements may affect this Document

- This document has been reproduced from the best copy furnished by the organizational source. It is being released in the interest of making available as much information as possible.

- This document may contain data, which exceeds the sheet parameters. It was furnished in this condition by the organizational source and is the best copy available.

- This document may contain tone-on-tone or color graphs, charts and/or pictures, which have been reproduced in black and white.

- This document is paginated as submitted by the original source.

- Portions of this document are not fully legible due to the historical nature of some of the material. However, it is the best reproduction available from the original submission.

NASA Contractor Report 177338

An Experimental Investigation of the Chopping of Helicopter Main Rotor Tip Vortices by the Tail Rotor

Ali R. Ahmadi

Contract NAS2-11313
September 1984

NASA

NASA CONTRACTOR REPORT 177338

AN EXPERIMENTAL INVESTIGATION OF THE CHOPPING OF HELICOPTER MAIN ROTOR TIP VORTICES BY THE TAIL ROTOR

Ali R. Ahmadi
Bolt Beranek and Newman Inc.
Cambridge, Massachusetts 02238

Prepared for

Ames Research Center
under Contract NAS2-11313

National Aeronautics and
Space Administration

Ames Research Center
Moffett Field, California 94035

SUMMARY

The chopping of helicopter main rotor tip vortices by the tail rotor was experimentally investigated. This is a problem of blade-vortex interaction (BVI) at normal incidence where the vortex is generally parallel to the rotor axis. The experiment used a model rotor and an isolated vortex and was designed to isolate BVI noise from other types of rotor noise. Tip Mach number, radial BVI station, and free stream velocity were varied. Fluctuating blade pressures, farfield sound pressure level and directivity, velocity field of the incident vortex, and blade-vortex interaction angles were measured.

Blade-vortex interaction was found to produce impulsive noise which radiates primarily ahead of the blade. For interaction away from the blade tip, the results demonstrate the dipole character of BVI radiation. The direction of minimum noise radiation, previously found to be in the plane of the blade, is found to be considerably shifted downstream of that direction. This shift is believed to be due to unsteady drag radiation caused by stronger BVIs in the present study. For BVI close to the tip, three-dimensional relief effect reduces the intensity of the interaction, despite larger BVI angle and higher local Mach number. Furthermore, in this case, the radiation pattern is more complex due to diffraction at and pressure communication around the tip.

Fluctuating blade pressures measured near the leading edge showed impulsive features due to BVI. Away from the tip, the peak-to-peak amplitude of fluctuating pressure on the suction side of the blade was larger than that on the pressure side, as expected. However, this trend was reversed near the blade tip. Furthermore, peak-to-peak amplitude of the fluctuating pressure on the pressure side near the tip was consistently the largest of all measured blade pressures for all conditions tested.

TABLE OF CONTENTS

TABLE OF CONTENTS (cont'd)

LIST OF SYMBOLS

b	Number of rotor blades
BPF	Blade passage frequency, Hz
c_R	Rotor chord length, m
c_W	Vortex generator chord length, m
C_T	Rotor thurst coefficient
d	Vortex core diameter, m
$\|\hat{D}\|$	Amplitude of unsteady drag of rotor blade section, Newton
D_o	Free jet nozzle exit diameter, m
D_R	Rotor diameter, m
h/R	Vortex generator tip-rotor tip separation distance normalized with rotor radius, positive for vortex generator tip outside of rotor disk
LE	Leading Edge
$\|\hat{L}\|$	Amplitude of unstedy lift of rotor blade section, Newton
M_T	Rotor tip Mach number
p	Pressure, Pascal
$p_{B,F}$	Fluctuating component of blade surface pressure
r/c_W	Radial distance normalized with vortex generator chord length
r/R	Radial distance normalized with rotor radius
r_I/R	Radial blade-vortex interaction station
R	Rotor radius, m
S	Rotor disk area, m^2
SPL	Sound pressure level, dB re 20 μPa
t	Time, sec
T_J	$\equiv (\frac{1}{2} \rho U_\infty^2)(\pi D_0^2/4)$, Newton
T_R	Total rotor thrust, Newton
v_i	Induced velocity at rotor disk, m/s
v_θ	Vortex azimuthal velocity, m/s
V_T	Tip speed, m/s
x/c_R	Chordwise distance from rotor blade leading edge normalized with rotor blade chord
u	Velocity component parallel to rotor axis, m/s
U_∞	Free stream velocity, m/s

LIST OF SYMBOLS (Cont'd)

V_∞	Component of free stream velocity parallel to rotor disk, m/s
α_R	Rotor collective pitch, degree
α_W	Vortex generator geometric angle of attack, degree
β	Blade-vortex interaction angle in a vertical plane (see Figure 1b), degree
γ	Blade-vortex interaction angle in a horizontal plane (see Figure 1a), degree
Γ	Tip vortex circulation, m^2/s
λ	Rotor inflow ratio
μ	Advance ratio
Ω	Rotor radian frequency, rad/s
ρ	Fluid density, kg/m^3
σ	Rotor solidity
θ	Microphone azimuthal position in a horizontal plane, measured from upstream direction (see Figure 1a), degree
$(\overline{\ })$	Ensemble averaged quantities

1. INTRODUCTION

Background

The most intense and annoying type of noise generated by a helicopter is impulsive in nature and generated by both the main and tail rotors. One of the main causes of impulsive rotor noise is blade-vortex interaction (BVI) which also causes high unsteady loads at the blades, hub, and control linkages, with the associated stresses and vibration. For these reasons, BVI aeroacoustics and aerodynamics have been and remain the subject of intense research (Ref. 1).

For the main rotor, BVI occurs when a blade passes close to a (main rotor) trailing vortex Here, the vortex is essentially parallel to the plane of blade motion. The significant BVI for the tail rotor, on the other hand, occurs when the main rotor tip vortices pass through the tail rotor disk, a situation which exists under most flight conditions. Here, the vortices are generally perpendicular to the rotor disk and hence are chopped by the blades. Because of the orientation of the vortex, herein, we refer to this type of interaction as "BVI at normal incidence". This main rotor/tail rotor interaction has been studied by only a few investigators (Refs. 2-4). These (experimental) studies are primarily concerned with the effect on tail rotor noise of: tail rotor position with respect to the main rotor, tail rotor direction of rotation, and main rotor tip vortex modifications. The results show an increase in tail rotor noise due to the interaction.

The only detailed study of noise radiation due to BVI at normal incidence is the recent work of Schlinker and Amiet (Ref. 5), who considered the interaction of an isolated vortex with a rotor. They developed an aeroacoustic theory (linearized, inviscid, compressible) for a blade of infinite span interacting with a straight vortex filament at normal incidence. To validate the theory, they conducted an experiment consisting of an

isolated tip vortex interacting with the rotor at normal incidence at a radial station removed from the tip: $r_I/R = 0.80$. Acoustic spectra, pressure signature, and directivity were measured. The theory shows the sensitivity of noise radiation to isolated changes in the governing parameters and predicts the SPL for the acoustic spectra and directivity patterns to within 5 dB at low frequencies.

Present Work

The main objective of the present work was to conduct a detailed experimental investigation of noise radiation and fluctuating blade pressures due to BVI at normal incidence near and away from the blade tip. The experiment which used an isolated vortex and a model rotor was designed to isolate BVI noise from other types of rotor noise. Figure 1 shows the configuration of the experiment where a two-bladed model rotor of 0.61 m diameter was operated with its axis parallel to the free stream direction. An isolated tip vortex was generated by an upstream semispan wing (vortex generator), convected downstream, and ingested by the rotor.

Choice of this simplified experimental configuration was primarily motivated by a desire to isolate and study in detail BVI at normal incidence. To ensure that the experiment was representative of the problem of chopping of main rotor tip vortices by the tail rotor, the model rotor was designed on the basis of a survey of the geometry of two-bladed tail rotors. Furthermore, all of the relevant similarity parameters for a tail rotor were matched. The only limitation of the experiment is the absence of helicopter forward motion effect, i.e., $\mu = 0$. The experiment thus represents the hover condition. However, forward motion of the helicopter may not significantly affect the present results, since it primarily shifts the position of the main rotor wake as it passes over the tail rotor disk.

The key parameters that were varied during the tests were tip Mach number M_T, radial BVI station r_I/R, and free stream velocity U_∞. An array of nine microphones located on a horizontal circular arc of 1.5 m radius (Figure 1), measured the SPL and directivity of the resulting impulsive noise. Four miniature blade-mounted pressure transducers measured the resulting fluctuating pressures at the blades near the leading edge. The velocity field of the incident vortex was measured with a miniature hot wire. Blade-vortex interaction angles were measured by the use of flow visualization and photography.

At the present time, no theoretical results are available for comparison with the present measurements of BVI near the blade tip where three-dimensional effects must be accounted for.

The present results may also be useful in the study of 1) counterrotating propellers and propfans where tip vortices from the front blade row may get ingested by the second blade row under certain flight conditions, and 2) pusher propellers ingesting tip vortices and wakes of upstream lifting surfaces such as canards, flaps and stabilizers.

2. EXPERIMENTAL APPROACH AND INSTRUMENTATION

2.1 Acoustic Wind Tunnel Facility

The experiments were conducted in the BBN high-speed acoustic wind tunnel in Cambridge. The facility is described in some detail in Refs. 6 and 7. The tunnel which is of the open-jet type consists of a long free jet enclosed in a large 7m x 13 m x 6 m test chamber, as shown in Figure 2. The tunnel can be operated in either open- or closed-circuit mode. For the present tests, it was operated in open-circuit mode to maintain constant flow temperature needed for Mach number similarity and hot wire anemometry. Flow temperature in the test section was continuously monitored by a thermocouple sensor.

The tunnel, which is powered by a 600 hp diesel engine, achieves a maximum velocity of 46 m/s for the 1.5 m^2 round nozzle used in the present tests. The overall turbulence level is 0.23%. The cell-like walls of the chamber which are covered with foam provide a cut-off frequency of 160 Hz.

The facility is equipped with a rotor spinner rig capable of operating at speeds up to 9000 rpm. The unit is driven by a hydraulic motor (maximum power output of 15 hp) and contains thrust and torque measurement systems. The unit is equipped with a 16-channel Freon TF-cooled high-speed slip ring. The spinner was mounted on its sting support and aligned with the free jet axis, at a height of 2.4 m above the chamber floor (Figure 3).

For the present tests it was important to position some of the farfield microphones as far upstream of the rotor disk as possible (see Ref. 5). This placed some of the rotor-microphone lines of sight close to the free jet nozzle exit flange. To minimize diffraction and scattering effects at the flange, foam wedge acoustic treatments were designed and installed at the nozzle flange, as shown in Figures 3 and 4.

2.2 Model Rotor and Vortex Generator

Rotor Similarity Parameters

In order to ensure that the present test configuration represented the chopping of the helicopter main rotor tip vortices by the tail rotor, the following dimensional and nondimensional similarity parameters appropriate to a tail rotor were matched.

1. Rotor tip speed, V_T = 183 - 213 m/s
2. Advance ratio, $\mu = V_\infty/(\Omega R)$ = 0 - 0.4
3. Blade loading, C_T/σ = 0.1 max
4. Disk loading, T_R/S = 239 - 479 Pa
5. Inflow ratio, $\lambda = (U_\infty + v_i)/(\Omega R)$ = 0.05 - 0.1 (hover)

where V_∞ is the component of free stream velocity parallel to the rotor disk, $C_T = T_R/[\rho\pi R^2(\Omega R)^2]$ is rotor thrust coefficient and $\sigma = bc/\pi R$ is rotor solidity. In addition, to ensure aerodynamic similarity and to eliminate vortex shedding noise, boundary layer trip strips were installed on the suction and pressure sides of the blades. The tripping device consisted of strips of pinked tape 0.2 mm in thickness installed at the quarter chord position. This efficient tripping device was first reported in Ref. 8 and later applied to a rotor in Ref. 9.

To match the rotor similarity parameters, rotor thrust was calculated using the extended blade-element theory of Ref. 10 with Prandtl-Betz tip loss correction and Prandtl-Glauert compressibility correction. For Test Condition 1 (see Table 2), the result was in good agreement with those of the lifting-surface theory of Ref. 11 with Prandtl-Glauert compressibility correction. The lifting-surface theory was also used to calculate radial blade thrust distribution and rotor torque.

For the present test configuration $V_\infty = 0$. Hence, the rotor advance ratio $\mu = 0$ for all conditions tested.

Rotor/Vortex Generator Relative Size and Spacing

Relative size of the model rotor and vortex generator was determined from a survey of light helicopters with two-bladed tail rotors. Parameters of interest were tail rotor solidity σ, blade aspect ratio AR, and the ratio of main rotor chord to tail rotor chord λ_1. The selected values were approximately the average values from the survey: $\sigma = 0.127$, AR = 5.00, and $\lambda_1 = 2.75$.

According to the wake rollup theory of Ref. 12, the wake of the vortex generator is essentially rolled up at a distance of 2.5 c_w downstream of the trailing edge. It is also known that tip vortices of helicopter main rotors roll up faster than those of fixed wing aircraft. Thus, the model rotor was placed three chord lengths downstream of the vortex generator trailing edge.

Model Rotor

Since the goal of the present work was to gain a better understanding of blade-vortex interaction at normal incidence, a simple generic model rotor was designed and constructed, with the following characteristics (see Figure 5):

- Number of blades: 2
- Diameter: 0.6 m
- Blade section: NACA 0012
- Blade planform: rectangular
- Twist: 0
- Collective pitch: 9° (fixed)
- Chord length: 6.1 cm (constant)
- Blade tip: flat (square cutoff)
- Blade aspect ratio: 5
- Rotor solidity: 0.127

- Direction of rotation: CW looking upstream
- Hub diameter: 6.4 cm

Selection of a design with constant collective pitch was determined by the low sensitivity of blade-vortex interaction noise to blade collective pitch, as determined in Ref. 5.

Vortex Generator

The vortex generator consisted of a semi-span wing with the following characteristics:

- Airfoil section: NACA 0012
- Planform: rectangular
- Twist: 0
- Span: 0.8 m
- Chord: 16.8 cm (2.75 times rotor blade chord)
- Tip geometry: rounded (NACA 0012 half body of revolution)

The vortex generator was mounted on a support system which allowed it to be moved vertically to adjust the blade-vortex interaction station r_I/R, and to adjust its angle of attack.

To ensure aerodynamic similarity, a boundary layer trip strip consisting of pinked aluminum tape 0.4 mm thick was installed at the quarter chord position on both sides of the vortex generator as well as around the tip. To check for fully attached flow at all angles of attack a row of tufts was installed on the suction side near the trailing edge. An internal tube carried the "smoke" to the tip of the vortex generator where it was injected through a thin stainless steel tube of 1.6 mm diameter into the evolving vortex core. The position of the tube could be adjusted as necessary.

2.3 Instrumentation

Flow Field Measurements

The velocity field of the incident vortex and the velocity defect in the wake of the vortex generator were measured at the location of the rotor disk, i.e., three chord lengths downstream of the vortex generator, by the use of a hot wire. The rotor was removed during these tests.

Because of the large velocity gradients and the small size of the vortex core, a single miniature 45° slanted hot wire of 5 μm diameter and 1.22 mm length was employed. The sensor was mounted on a long and slender probe support which was aligned with the free stream to minimize disturbances to the vortex. Using a traversing mechanism, the probe was slowly (0.85 mm/sec) and continuously traversed through the flow field twice, with a rotation of 180°. It is well known that the two components of velocity at each point are then obtained from the sum and difference of the mean linearized voltages of the sensor for the two orientations.

Acoustic Measurements

Preliminary acoustic measurements of blade-vortex interaction showed that the impulsive noise was radiated primarily ahead of the blade chopping the vortex and that it was more intense for microphone positions farthest removed from the rotor disk (i.e., θ). These tests also showed that BVI noise was somewhat more intense in a horizontal plane passing through the rotor center than one passing through the BVI location. The foam wedge acoustic treatment for the free jet nozzle flange made it possible to locate microphones as far as 40° upstream of the rotor disk without any significant interference from the nozzle.

Farfield sound pressure level and directivity of blade-vortex interaction were measured by an array of nine 1.27 cm B&K microphones mounted at grazing incidence on a horizontal circular

arc of 1.5 m radius centered at the rotor center, as shown in Figure 1. The microphones have a flat response over the 160 Hz - 20 kHz range of the present study. They were located at 10° increments from θ = 50° through 130°, i.e., from 40° upstream to 40° downstream of the rotor disk.

Fluctuating Blade Pressure Measurements

Four miniature blade-mounted pressure transducers (BMT) measured the fluctuating blade pressures. The BMTs (Kulite Model LQ-5-080) had a sensor area 1 mm in diameter (1.6% of blade chord) and were mounted in pairs on opposite sides of the blades. Guided by the full-scale unsteady blade loads data of Ref. 13, the BMT's were located as close to the leading edge as possible: 10% of chord from the leading edge. One pair of BMTs was located at r/R = 0.90 on one blade and the other pair at r/R = 0.975 on the other, corresponding to the two BVI stations investigated. BMT designations are listed in Table 1. To ensure accurate measurement of BVI-induced fluctuating pressures, the BMTs (and their leads) were mounted flush with the blade surface and strain isolated from the blades per manufacturer's directions (see also Ref. 14). Close-up views of two of the BMTs are shown in Figures 6 and 7.

Since the BMTs were only used to measure fluctuating blade pressures (not steady), only a dynamic calibration consisting of 144 dB at 250 Hz was used. Calibration was applied to the BMTs on the blades, so as to have a complete system calibration. The BMT data was analyzed up to 20 kHz, which is about 1/10 the first resonant frequency of the BMT.

Data Processing and Analysis

Microphone and BMT signals were amplifed and then recorded on magnetic tape. The dynamic response of the FM tape recorder (Honeywell Model 5600E) was flat over the 160 Hz - 20 kHz range of interest. Acoustic and blade pressure waveforms were ensemble

averaged using a dual channel analyzer (HP MOdel 5423A) with a resolution of 512 lines. The acoustic waveforms were ensemble averaged over a time window of 10 msec with a time increment between digital samples of 19.5 μsec, ensuring good resolution. For the blade pressure data, the time window was 20 msec and the time increment was 39.1 μsec. All ensemble averages were obtained from 50 consecutive samples. The rotor spinner tachometer signal was used to trigger the sampling. Acoustic and blade pressure data were analyzed using a spectrum analyzer (Nicolet Scientific Model 446A) with a resolution of 400 lines, at constant bandwidth. The data processing and analysis equipment are shown in Figure 8.

Flow Visualization and Photography

Two of the important parameters which determine the strength of blade-vortex interaction are 1) radial blade-vortex interaction station, r_I/R, and 2) blade-vortex interaction angles, β and γ. During the present tests, these parameters were set and measured by flow visualization and photography. To visualize the flow, oil vapor was injected through a thin tubing (1.6 mm diameter) at the wing tip into the evolving vortex core, where it tends to stay confined.

Flow visualization of blade-vortex interaction was recorded by two Hasselblad cameras positioned in the rotor disk. One camera, with a horizontal line of sight, was positioned for measuring the vertical angle β and the other, with a vertical line of sight, for measuring the horizontal angle γ. Shutter speed of the cameras was generally 1/8 sec, a time increment in which the rotor undergoes about a dozen revolutions. Back lighting of the oil vapor was provided by a 1000 W collimated light source.

3. TEST PROGRAM AND QUALIFICATION TESTS

3.1 Selection of Test Conditions

The strength of blade-vortex interaction is primarily determined by: 1) tip Mach number M_T, 2) blade-vortex interaction angles β and γ, 3) radial interaction station r_I/R, and 4) vortex strength and core size. In the present study, the first three of these parameters were varied while the vortex strength was maintained nearly constant. Vortex core diameter increased with increasing angle of attack.

The study focused on BVI at two radial stations: $r_I/R = 0.90$ and 0.975. The first corresponds to the radial station of maximum spanwise loading for the present rotor, as determined by lifting-surface theory calculations (Ref. 11). The other station is the one for which the vortex core is just inboard of the tip.

Three tip Mach numbers were selected for the tests: $M_T = 0.55$, 0.59, and 0.63. Blade-vortex interaction noise for $M_T < 0.55$ was studied in Ref. 5. For $M_T > 0.63$, thickness noise and transonic effects prevent isolation of blade-vortex interaction phenomenon (see experimental data in Refs. 15-17).

To create strong BVIs, simultaneous with increasing tip Mach number, free stream velocity was reduced from $U_\infty = 9.1$, 8.2, 7.3 m/s to increase the rotor slipstream contraction and hence β. This would also decrease the incident vortex strength. To maintain the vortex strength at approximately the same value, the vortex generator angle of attack was increased simultaneously from $\alpha_W = 12°$, 13.3°, 15°.* The necessary incremental changes in angle of attack were calculated from two-dimensional airfoil theory applied at a section away from the tip. This is justified because 1) all trailing vorticity outboard of the section of

*The flow remained fully attached even at the larger angles of attack, as demonstrated by flow visualization. This is due to large induced downwash (low aspect ratio) which reduces the effective angle of attack.

maximum loading rolls up to form the tip vortex and 2) the trailing wake is essentially rolled up three chord lengths downstream of the vortex generator trailing edge where the rotor is located.

3.2 Qualification Tests

Anechoic Test Environment

To verify that the test environment for the present experimental setup was anechoic a series of "doubling-of-distance" tests (i.e., 6 dB reduction in SPL for every doubling of distance) were conducted. An acoustic source consisting of an acoustic driver and a cylindrically symmetric horn was positioned, with its axis vertical, at the blade-vortex interaction location (rotor in horizontal position). Three 1.27 cm B&K microphones were positioned along a horizontal radial line emenating from the rotor center. One-third octave band analyses of the measured SPLs were used to assess the acoustic environment. This procedure was repeated for various microphone locations and verified that good anechoic environment existed in the test area down to 160 Hz.

Background Noise

To measure background noise levels for the tests, the rotor and the vortex generator were removed and SPL was measured by all 9 microphones, with the wind tunnel and the rotor spinner operating. The background noise tests are summarized below.

Background Noise Test	Rotor Spinner Rotation Rate	Corresponding Tip Mach No.	Free Stream Velocity	Corresponding Test Condition
1	100 Hz	0.55	9.1 m/s	1, 4
2	107 Hz	0.59	9.1 m/s	2, 5
3	114 Hz	0.63	9.1 m/s	3, 6

The measured background noise levels are shown in Figs. 9-11 for the microphone position $\theta = 50°$, which was typical of all microphone locations. Background noise was generally 20 dB below the rotor noise levels for all test conditions.

Steadiness of the Experiment

The following data analysis "experiments" demonstrate the steadiness of the tests, i.e., rotor rotation rate, free stream velocity and vortex position and characteristics. Figure 12 shows a long-time-average (3 min 25 sec) rotor acoustic spectrum at 1.25 Hz bandwidth for a typical test. The sharpness of the rotor tones demonstrates the steadiness of the rotor rotation rate. Figure 13 shows a superposition of three short-time-average (0.32 sec) rotor acoustic spectra from the beginning, middle, and end of the same test record. It is seen that the corresponding tone levels are generally within 1 dB of each other, demonstrating the overall steadiness of the experiment.

Narrowband Random Tones

Figure 14(a) shows a high resolution spectrum of a selected rotor tone from Figure 13. It is seen that what appears to be a discrete tone in Figure 13 actually consists of narrowband random tones. Inflow turbulence is ruled out as the cause using arguments similar to those of Ref. 5 (whose vortex generator is similar to that of the present tests) and the inherent low turbulence levels of the BBN acoustic wind tunnel. Figure 14(b) shows a high resolution spectrum of the corresponding tone in rotor spinner tachometer signal. Similarity of the structure of the two tones demonstrates that the narrowband random peaks in the acoustic spectrum are caused by small variations (fraction of a Hertz) in spinner rotation rate.

Shear Layer Injestion

To ensure that the free jet turbulent shear layer was not injested by the rotor during the tests two steps were taken: 1) a simplified analysis to predict the onset of shear layer injestion for given operating conditions and 2) actual verification by flow visualization during the tests. The analysis was developed using the continuity of mass and an actuator disk model of the rotor for incompressible flow.

For a rotor of diameter D_R with axis aligned with that of a free jet, a distance x downstream of the nozzle exit of diameter D_o, a relationship is developed for the onset of shear layer injestion with (T_R/T_J) as a parameter. T_R is rotor thrust and T_J is free jet "thrust" defined as $(1/2\ \rho U_o^2)\ (\pi D_o^2/4)$. The result is given by

$$\frac{D_R}{D_o} = \left\{ \frac{\left[1 - 0.2\ \left(\frac{x}{D_o}\right)\right]^4}{\frac{1}{4}\left(\frac{T_R}{T_J}\right) + \left[1 - 0.02\ \left(\frac{x}{D_o}\right)\right]^2} \right\}^{1/2}$$

This relationship is plotted for a range of values of (T_R/T_J) in Figure 15. Thus, according to the theory, for a given (T_R/T_J), operating points under the corresponding curve will not encounter injestion, with the curve itself representing the onset of injestion. It is seen that with increasing (T_R/T_J) smaller rotors must be used and they must be placed closer to the nozzle exit.

Since the above analysis does not account for unsteady undulations of the shear layer boundary and the non-uniform thrust and induced velocity distributions on the rotor disk, the actual boundaries of incipient shear layer injestion are expected to be below those indicated in Figure 15.

The above considerations were used as a guide in selecting the rotor size and position in the free jet: $D_R/D_o = 0.50$ and $x/D_o = 0.57$. The calculated value of (T_R/T_J) for Test Condition

1 (r_I/R = 0.90, M_T = 0.55, U_∞ = 9.1 m/s) and the selected size and position of the rotor are also shown in Figure 15.

Shear Layer Refraction and Scattering of Sound

Effect of free jet shear layer refraction and scattering of sound for the present tests was insignificant since the free stream Mach number was below 0.1 (see Ref. 18).

4. EXPERIMENTAL RESULTS AND DISCUSSION

4.1 Vortex Flow Field Measurements

Figures 16 and 17 show, respectively, the azimuthal and axial velocity fields of the vortex (data filtered) for Test Condition 1 (U_∞ = 9.1 m/s, α_W = 12°, vortex generator AR = 1.7). The maximum azimuthal velocity is seen to be about 0.45 U_∞ and the diameter of the viscous core of the vortex is 0.083 c_W. The velocity distribution about the vortex center is not perfectly symmetric. This near-wake asymmetry, which has been observed by other investigators (see, e.g., Ref. 19), is due to the rollup of the trailing vortex sheet. The axial velocity distribution through the vortex center displays a maximum velocity defect of 0.07 U_∞, which is not significant, and a similar asymmetry due to wake rollup.

The velocity field of the incident vortex was not measured for the other two test conditions. However, the above measurements for Test Condition 1 (r_I/R = 0.90, M_T = 0.55, U_∞ = 9.1 m/s) are expected to be representative of the other test conditions as well, since the strength of the tip vortex was kept nearly constant for all test conditions, as pointed out in the above. Flow visualization results seem to indicate that vortex core diameter increased with vortex generator angle of attack (while free stream velocity was reduced).

The axial velocity defect in the wake of the vortex generator at zero angle of attack, at a spanwise station 0.15 c_W inboard of the tip was 0.12 U_∞ (maximum). At nonzero angles of attack, this velocity defect as well as the width of the wake would be somewhat larger.

Effect of rotor slipstream contraction

Since the incident vortex velocity field and core size were measured (at the rotor disk) with the rotor removed, the measured results must be corrected for the effect of rotor slipstream

contraction. A simplified analysis based on Kelvin's thecrem and the continuity equation (see Ref. 5) shows that the effect of flow contraction is to

1) reduce the vortex core diameter (proportional to the flow contraction ratio),

2) increase the axial velocity in the vortex core (proportional to the inverse square of the contraction ratio).

The product of vortex core radius and maximum azimuthal velocity (i.e., circulation) remains constant.

Thus, for example, for Test Condition 2 (r_I/R = 0.90, M_T = 0.59, U_∞ = 8.2 m/s), flow contraction reduces vortex core diameter by 14%, which tends to make the interaction somewhat more impulsive, and increases the vortex core axial velocity by 36%. However, since the axial flow velocity outside the core increases by about the same amount, the relative magnitude of the velocity defect in the core remains approximately the same (0.07 U_∞ max).

4.2 Flow Visualization Results

Blade-vortex interaction angles β and γ were measured from photographs of flow visualization of vortex core, as described in Sec. 2.3. Figure 18 shows an example of flow visualization for Test Condition 3 (r_I/R = 0.90, M_T = 0.63, U_∞ = 7.3 m/s) in side view from which β was measured. Figure 19 shows an example for Test Condition 1 (r_I/R = 0.90, M_T = 0.55, U_∞ = 9.1 m/s) in bottom view from which γ was measured. Figure 20 shows a closeup of the side view for Test Condition 3.

Measured values of β and γ for the six test conditions are given in Table 2. It is seen that large values of β were measured in the tests, β = 20° - 39°. Values of γ on the other hand, were γ = 3° ± 0.5° for all test conditions. Since γ is

caused by the downwash field of the wing, it suggests that tip vortex strength (and the vortex generator load distribution) were nearly constant at the three sets of angle of attack and free stream velocity, as pointed out in Sec. 3.1. Furthermore, because of the small values of γ, its effect on blade-vortex interaction is expected to be insignificant. The intensity of the interaction depends primarily on the vertical angle β.

Figures 18 and 20 show an apparent enlargement of the vortex core immediately downstream of the rotor disk. This phenomenon was observed for all test conditions reported herein, but not for some exploratory test conditions with small values of β. A recent computational study (Ref. 20) of parallel blade-vortex interaction at low Reynolds number has shown vortex core enlargement (diffusion) due to the interaction. This phenomena is not well understood at the present time. The apparent enlargement of the core in Figure 20 may be due to the action of centrifugal forces on "smoke" particles entrained into the rotor blade boundary layer, since the enlargment is primarily radially outward. That is, it may not represent actual vortex core enlargement. However, for another test condition (not reported herein) the enlargement was in all directions.

4.3 Farfield SPL and BVI Signature

Rotor acoustic waveforms for vortex-present ($\alpha_W > 0$) and vortex-absent ($\alpha_W = 0$) cases were ensemble averaged. An example is shown in Figure 21 (a, b), where it is seen that the vortex creates an impulsive feature in the waveform. To obtain the net effect of the vortex, i.e., the BVI signature, the waveform for vortex-absent case was subtracted from that for the vortex-present case to remove the rotor loading noise and that due to the vortex generator viscous wake. The resulting BVI signature, Figure 21(c), has the impulsive character and the shape and sign expected on physical grounds, as explained by Figures 22 and 23. Figure 22 schematically depicts the velocity field, normal to the

rotor disk, induced by the vortex azimuthal velocity because of the oblique intersection of the vortex with the rotor disk. Figure 23 from Ref. 1 shows, qualitatively, the resulting blade angle of attack and lift fluctuations, and the farfield acoustic pressure. Their explanation (based on the Ffowcs Williams and Hawkings formulation) is for the case where the incident vortex is parallel to the plane of the blade, but from a potential flow viewpoint, it is valid for the present case as well.

Figure 24 shows a comparison of BVI signatures at $\theta = 50°$ for Test Conditions 1, 2 and 3 ($r_I/R = 0.90$). As expected, the peak amplitude of BVI signature increases with increasing M_T and β (see Table 2), indicating stronger BVIs. Figure 25 shows a similar trend for Test Conditions 4, 5 and 6 ($r_I/R = 0.975$) except all peak amplitudes are smaller than their counterparts at $r_I/R = 0.90$. This is due to three-dimensional relief effect at the rotor tip which reduces the intensity of BVI radiation.

Figure 26 shows the complete set of BVI signatures* ($\theta = 50°$-$130°$) for Test Condition 2 ($r_I/R = 0.90$, $M_T = 0.59$, $U_\infty = 8.2$ m/s). It is seen that BVI radiation is more intense for azimuths farthest removed from the rotor disk, with minimum radiation occurring near $\theta = 100°$. The significance of the orientation of this radiation pattern is discussed in Sections 4.5 and 4.6.

4.4 Rotor Acoustic Spectra

The effect of BVI on rotor aeroacoustics is also seen from a comparison of rotor acoustic spectra for vortex-present and vortex-absent cases. Figures 27-32 show the spectra, respectively, for Test Conditions 1-6, for $\theta = 50°$. In each case, it is seen that BVI significantly alters the acoustic spectra by increasing the rotor tone levels over a wide frequency range.

---

*The shape and antisymmetry of the BVI signatures (about the point of peak amplitude) is consistent with the recent analytical time-domain calculations of Ref. 25.

Except for the first few harmonics of BPF which are dominated by the rotational noise, the higher harmonics show 5-15 dB increase, extending up to 10-15 kHz. A comparison of the spectra for Test Conditions 1-3 (r_I/R = 0.90) shows that, with increasing M_T and β, the BVI induced tone levels are larger and extend to higher frequencies, in other words, a stronger BVI. A similar observation is made for Test Condition 4-6 (r_I/R = 0.975), except these show weaker BVIs compared with their counterparts at r_I/R = 0.90 (as explained earlier); compare, for example, Figures 27 and 30.

A complete set of acoustic spectra (θ= 50°-130°) for Test Condition 2 (r_I/R = 0.90, M_T = 0.59, U_∞ = 8.2 m/s) is presented in Figures 33-41. They show that, with increasing θ, 1) rotor loading noise increases reaching a maximum level at the rotor disk and then dropping off, and 2) BVI tone levels decrease reaching a minimum at about θ = 100° and then increase again. These features are seen more clearly in the directivity patterns in the next section.

4.5 Directivity Patterns

Blade-vortex interaction directivity patterns were obtained by plotting the measured tone levels as a function of microphone position θ for selected harmonics of BPF. Figures 42-47 show the results, respectively, for Test Conditions 1-6, for 1, 5, 10, 15, 25 and 35 x BPF harmonics. Tone levels used in the directivity plots have been corrected for proximity to the broadband level. Tones within 1 dB of the broadband level have been corrected and also denoted by a special symbol indicating that the actual level is expected to be somewhat lower than that shown.

For each test condition, the first few harmonics are dominated by rotor loading noise. For blade-vortex interaction away from the tip (r_I/R = 0.90), the BVI-induced higher harmonics display a minimum near θ = 100° with nearly equal tone levels on either side, as seen in Figures 42-44. For Test Condition 2

(r_I/R = 0.90, M_T = 0.59, U_∞ = 8.2 m/s), this direction is θ = 97°. This can also be seen in the radiation pattern of BVI signatures summarized in Figure 48, where there is a minimum at about θ = 100° and a polarity reversal about that point at nearly constant amplitude. This demonstrates the dipole character of the radiation pattern. The direction of minimum SPL, previously found (Ref. 5) to be in the plane of the blade (i.e., θ = 81°) for interaction farther away from the tip is found to be significantly shifted downstream of that direction by 15-20°. It is shown in the next section that this shift is probably caused by unsteady drag radiation due to stronger BVIs in the present study.

For blade-vortex interaction away from the tip (r_I/R = 0.975), the directivity patterns for the higher harmonics do not show a dipole radiation pattern but a more complex one with minima occurring at θ = 80° - 120°. The added complexity is believe to be due to a more complex (than dipole) source near the tip and diffraction at the tip.

4.6 Unsteady Drag Radiation

The present results thus confirm the dipole character of the BVI radiation pattern for interactions not very close to the rotor tip (r_I/R = 0.90). However, the direction of minimum radiation, previously found to be in the plane of the blade for intraction farther away from the tip (theory and experiments of Ref. 5), i.e., θ = 81°, is found to be significantly shifted downstream, by 15° - 20°. This is believed to be due to unsteady drag dipole radiation caused by stronger BVIs in the present study. It can be shown that when unsteady drag dipole radiation is combined with unsteady lift dipole radiation, which is expected to be in phase with it, they give rise to a rotated dipole radiation pattern, as shown in Figure 49. The dipole rotation angle $\phi = \tan^{-1}(|\hat{D}|/|\hat{L}|)$, where $|\hat{D}|$ and $|\hat{L}|$ are, respectively, the amplitudes of unsteady drag and lift of the

rotor blade section encountering the vortex. For Test Condition 2 (r_I/R = 0.90, M_T = 0.59, U_∞ = 8.2 m/s), $\phi \approx 16°$. This corresponds to $|\hat{D}| \approx 0.3\ |\hat{L}|$, which is a large amplitude for unsteady drag. Lack of unsteady drag dipole radiation in the measurements of Ref. 5 is believed to be due to weaker BVIs: M_T = 0.39 - 0.55, r_I/R = 0.80, β = 0° - 14.6°. Also their theoretical predictions are based on an acoustic theory which does not include the effect of unsteady drag.

4.7 Fluctuating Blade Pressures

Unsteady blade pressure waveforms (with steady component removed) were obtained for vortex-present and vortex-absent cases. Figure 50(a,b) shows an example. As for the acoustic waveforms in Section 4.3, here the net effect of the vortex on the fluctuating blade pressure is obtained by subtracting the waveform for the vortex-absent case from that with the vortex present. The result is shown in Figure 50(c), where it is seen that interaction with the vortex produces a highly impulsive pressure at the blade. The shape and sign of the fluctuating blade pressure due to BVI is as expected on physical grounds (see Figures 22 and 23).

The regular small-amplitude waveforms seen in Figures 50(a,b) are due to certain blade natural frequencies* communicated to the BMT through residual base strain. It is seen, however, that frequencies and amplitudes of these for the vortex-present and absent cases are nearly the same and hence cancel each other, as seen in Figure 50(c). This was especially true for test conditions with large M_T and β (i.e., Test Conditions 2,3,5 and 6).

---

*The associated aerodynamic contribution is expected to be small since no transverse blade motion could be seen with the aid of a strobe tach at frequencies up to BPF.

The fluctuating blade pressure at BMT 1 (r/R = 0.975 pressure side) consistently showed the highest peak-to-peak amplitude for all test conditions. This is in part due to the large values of local Mach number and β at this station. Another potential contributor is the anticipated large induced upwash near the blade tip (possibly logarithmically infinite at the tip, see Refs. 21-23) which would shift the stagnation point on the pressure side of the blade farther away from the leading edge and hence closer to BMT 1 (x/c_R = 10%) where it oscillates about its mean position due to interaction with the vortex.

Figure 51 shows the fluctuating blade pressure at BMT 1 (r/R = 0.975, pressure side) for Test Conditions 1, 2 and 3 (r_I/R = 0.90). It is seen that the peak-to-peak amplitude increases with increasing M_T and β, as expected. Figure 52 shows a similar trend for Test Conditions 4, 5 and 6 (r_I/R = 0.975), except all peak-to-peak amplitudes are smaller than their counterparts for r_I/R = 0.90 due to three dimensional relief effect at the blade tip.

Figure 53 shows the fluctuating blade pressures at all four BMTs for Test Condition 2 (r_I/R = 0.90, M_T = 0.59, U_∞ = 8.2 m/s). The expected polarity reversal for each pair is apparent. We note that, away from the tip (r/R = 0.90), BMT 4 (suction side) shows a larger peak-to-peak amplitude than BMT 3 (pressure side), as expected (due to compressibility effect). Near the tip (r/R = 0.975), however, BMT 1 (pressure side) shows a larger peak-to-peak amplitude than BMT 2 (suction side), as explained in the above. This pattern was generally observed for all conditions tested. A similar trend is seen in the full-scale "Operational Loads Survey" data (Ref. 13), where, at stations removed from the tip, the peak-to-peak amplitude of fluctuating blade pressure on the suction side (near the leading edge) is larger than that on the pressure side. However, as the blade tip is approached the amplitudes approach each other. (The station closest to the tip is r/R = 0.955.) Presumably, at stations

closer to the tip, the trend is reversed, as observed in the present tests.

4.8 Fluctuating Blade Pressure Spectra

The effect of BVI on blade pressures is also seen from a comparison of fluctuating blade pressure spectra for vortex-present and vortex-absent cases. Figures 54-59 show these results, respectively, for Test Conditions 1-6, at BMT 1 (r/R = 0.975, pressure side). In each case, it is seen that blade-vortex interaction significantly alters the spectra by increasing the tone levels (at the shaft rotation rate) over a wide frequency range. For the conditions tested BVI generally increased the tone levels by 5-15 dB, with the increase extending up to 5-10 kHz. The unusually high peaks in the spectra, e.g., at 1.4 and 4.4 kHz in Figure 54, are blade natural frequencies communicated to the BMT through residual base strain, as pointed out in Section 4.7. Comparisons of the above spectra lead to similar conclusions, as in Section 4.4 for the rotor acoustic spectra.

A complete set of fluctuating blade pressure spectra (BMT 1 - BMT 4) for Test Condition 2 (r_I/R = 0.90, M_T = 0.59, U_∞ = 8.2 m/s) is presented in Figures 60-63. They demonstrate, for Test Condition 2, our earlier point that BMT 1 consistently showed the most intense pressure fluctuations of the four BMTs.

5. CONCLUSIONS AND RECOMMENDATIONS

Acoustic radiation:

1) Blade-vortex interaction produces harmonic noise which extends to high frequencies and radiates primarily ahead of the blade.
2) For blade-vortex interaction away from the tip (r_I/R = 0.90), the directivity pattern and acoustic signatures demonstrate the dipole character of the radiation. The direction of minimum noise radiation, previously found to be in the plane of the blade for interaction farther away from the tip, is found to be significantly shifted downstream of that direction. The reason for this shift is believed to be unsteady drag dipole radiation which combines with unsteady lift dipole radiation to produce a rotated dipole radiation pattern. The rotation angle is determined by the ratio of the amplitudes of unsteady drag to unsteady lift. The large dipole rotation angles observed ($\Delta\theta \approx 16°$) suggest large unsteady drag amplitudes, $|\hat{D}| \approx 0.3\ |\hat{L}|$.
3) For blade-vortex interaction in the immediate vicinity of the tip (r_I/R = 0.975), the radiation pattern is more complex due to diffraction at and pressure communication around the tip.
4) The effect of blade-vortex interaction on rotor acoustic spectra is to increase rotor tone levels by 5 - 15 dB. This increase extends to high frequencies (up to 10 - 15 kHz).
5) Blade-vortex interaction at the radial station of maximum blade loading (r_I/R = 0.90) was more intense than that near the blade tip, where the three-dimensional relief effect reduces the intensity of the interaction.
6) Present results show no significant effect due to the chopping of the incident vortex. However, the results

are expected to be significantly affected in the presence of large axial velocity in the vortex core.

Fluctuating blade pressures:

1) Blade-vortex interaction produces highly impulsive pressures at the blade surface near the leading edge.
2) The effect of blade-vortex interaction on fluctuating blade pressure spectra is to increase tone levels by 5 - 15 dB. This increase extends to high frequencies (up to 5 - 10 kHz).
3) Away from the tip (r/R = 0.90), the peak amplitude of fluctuating blade pressure on the suction side (BMT 4) was generally larger than that on the pressure side (BMT 3), as expected. However, near the tip (r/R = 0.975), this trend was reversed for BMT 1 and BMT 2.
4) For all test conditions, the peak fluctuating blade pressure on the pressure side near the tip (BMT 1) showed the largest peak amplitude.

Theory: The following theoretical developments are recommended for comparison with the present results.

1) To predict the noise radiation due to strong blade-vortex interaction (unsteady lift and drag radiation) at stations away from the tip, the two-dimensional theory of Ref. 5 should be extended to include the effect of unsteady drag radiation.
2) To predict the aeroacoustics of BVI in the immediate vicinity of the tip, a first step would be application of the three-dimensional theory of Ref. 24 for the interaction of an oblique sinusoidol gust with a blade tip (quarter-infinite flat plate).

REFERENCES

1. Schmitz, F.H. and Yu, Y.H. (1983), "Helicopter Impulsive Noise: Theoretical and Experimental Status," NASA TM-84390.

2. White, R.P. Balcerak, J.C., and Pegg, R.J. (1976), "A Parametric Model Study of the Noise Generated by the Aerodynamic Interaction of the Tail Rotor with the Wake of the Main Rotor," AHS Mid-East Region Symposium of Rotor Technology, Essington, PA.

3. Leverton, J.W., Pollard, J.S., and Willis, C.R. (177), "Main Rotor/Tail Rotor Interactions," Vertica, Vol. 1, No. 3, pp. 213-221.

4. Pegg, R.J. and Shidler, P.A. (1978), "Exploratory Wind Tunnel Investigation of the Effect of the Main Rotor Wake on Tail Rotor Noise," NASA CP- 2052, Part 1, pp. 205-219.

5. Schlinker, R.H. and Amiet, R.K. (1983), "Tail Rotor Blade-Vortex Interaction Noise," AIAA Paper 83-0720.

6. Kadman, Y. and Hayden, R.E. (1976), "Factors in the Design and Performance of Free-Jet Acoustic Wind Tunnels," Progress in Astronautics and Aeronautics, Vol 46, pp. 247-258.

7. Hayden, R.E. and Theobald, M.A. (1982), "Aeroacoustic Facility Installation Effects on the Generation and Propagation of Propeller-Generated Noise," BBN Report No. 5126.

8. Hama, F.R. (1957), "An Efficient Tripping Device," J. Aeronautical Sci., 24, pp. 236-237, March.

9. Paterson, R.W. and Amiet, R.K. (1979), "Noise of a Model Helicopter Rotor Due to Injestion of Turbulence," NASA CR-3213.

10. Gessow, A. and Myers, G.C., Jr., Aerodynamics of the Helicopter, Ungar Publishing Co., New York.

11. Greeley, D.S. and Kerwin, J.E. (1982), "Numerical Methods for Propeller Design and Analysis in Steady Flow," SNAME Transactions, Vol. 90, pp. 415-453.

12. Spreiter, J.R. and Sacks, A.H. (1951), "The Rolling Up of the Trailing Vortex Sheet and Its Effect on the Downwash Behind Wings," J. Aeronautical Sci., January.

13. Shockey, G.A., Williamson, T.W. and Cox, C.R. (1977), "AH-1G Helicopter Aerodynamic and Structural Loads Survey," USAAMRDL-TR-76-39, Bell Helicopter Textron, February

14. Englund, D.R., Grant, H.P. and Lanati, G.A. (1979), "Measuring Unsteady Pressure on Rotating Compressor Blades," NASA TM-79159.

15. Schlichting, H. and Truckenbrodt, E. (1979), Aerodynamics of the Airplane, McGraw-Hill, Inc., New York.

16. Abbott, I.H. and von Doenhoff, A.E. (1959), Theory of Wing Sections, Dover Publications, Inc., New York.

17. Kuethe, A.M. and Schetzer, J.D. (1959), Foundations of Aerodynamics, 2nd edition, John Wiley & Sons, Inc., New York.

18. Schlinker, R.H., and Amiet, R.K. (1980), "Shear Layer Refraction and Scattering of Sound," AIAA Paper 80-0973.

19. Lee, H. and Schetz, J.A. (1983), "Computational and Experimental Study of Tip Vortices," AIAA Paper 83-1868.

20. Hardin, J.C. and Lamkin, S.L. (1984), "Aeroacoustic Interaction of a Distributed Vortex with a Lifting Joukowski Airfoil," AIAA Paper 84-2287.

21. Jordan, P.F. (1971a), "The Parabolic Wing Tip in Subsonic Flow," AIAA Paper No. 71-10.

22. Jordan, P.F. (1971b), "Span Loading and Formation of Wake," in Aircraft Wake Turbulence and Its Detection, J.H. Olsen, A. Goldberg and M. Rogers, eds. Plenum Press, pp. 207-227.

23. Landahl, M.T. (1968), "Pressure Loading Functions for Oscillating Wings with Control Surfaces," AIAA J., 6, No. 2, February, pp. 345-348.

24. Martinez, R. and Widnall, S.E. (1983), "Aerodynamic Theory for Wing with Side Edge Passing Subsonically Through a Gust," AIAA J., 21, No. 6, June.

25. Lee, D.J. and Roberts, L. (1985), "Interaction of a Turbulent Vortex with a Lifting Surface," AIAA Paper No. 85-0004.

TABLE 1

LOCATION OF BLADE MOUNTED PRESSURE TRANSDUCERS (BMT) ON ROTOR BLADES

Transducer	Rotor Blade	Blade Surface	Radial Location r/R	Chordwise Distance From LE, x/c_R
BMT 1	1	pressure side	0.975	0.10
BMT 2	1	suction side	0.975	0.10
BMT 3	2	pressure side	0.90	0.10
BMT 4	2	suction side	0.90	0.10

TABLE 2

TEST CONDITIONS

Test Condition	r_I/R	M_T	U_∞(m/s)	α_W	β	γ	$\frac{\Gamma}{2\pi C_W U_\infty}$	d/c_W	h/R
1	0.90	0.55	9.1	12°/0°	20°	3°	0.018	0.083	0
2	0.90	0.59	8.2	13.3°/0°	23°	3°	(0.018)	-----	0.05
3	0.90	0.63	7.3	15°/0°	35°	3°	(0.018)	-----	0.21
4	0.975	0.55	9.1	12°/0°	25°	3°	0.018	0.083	0.12
5	0.975	0.59	8.2	13.3°/0°	30°	3°	(0.018)	-----	0.15
6	0.975	0.63	7.3	15°/0°	39°	3°	(0.018)	-----	0.25

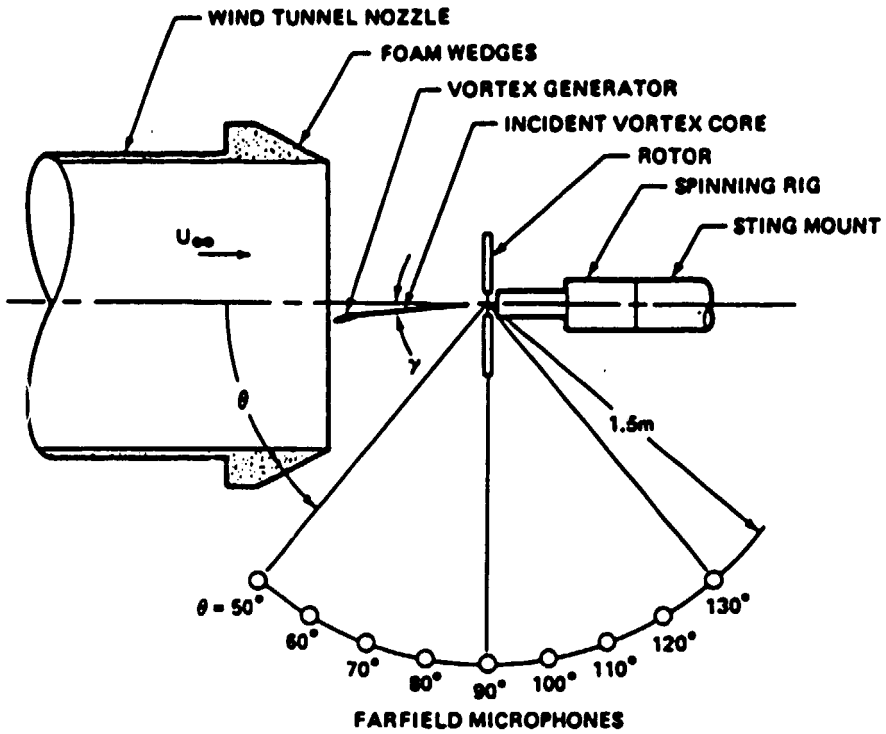

a) Planview

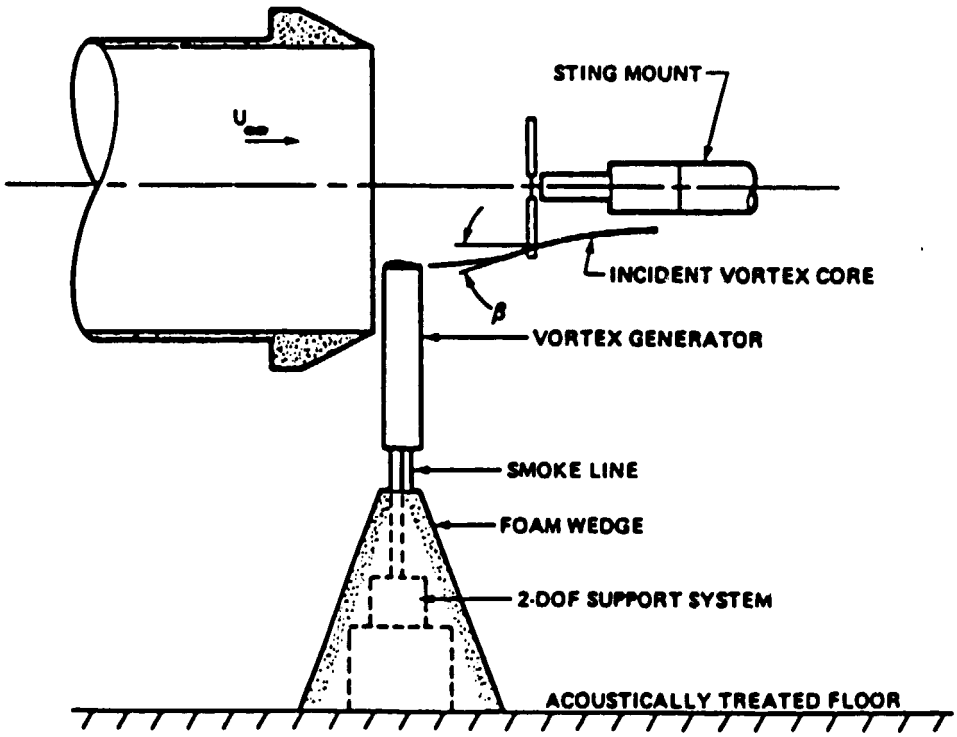

b) Sideview

FIG. 1. SCHEMATIC OF EXPERIMENTAL SETUP.

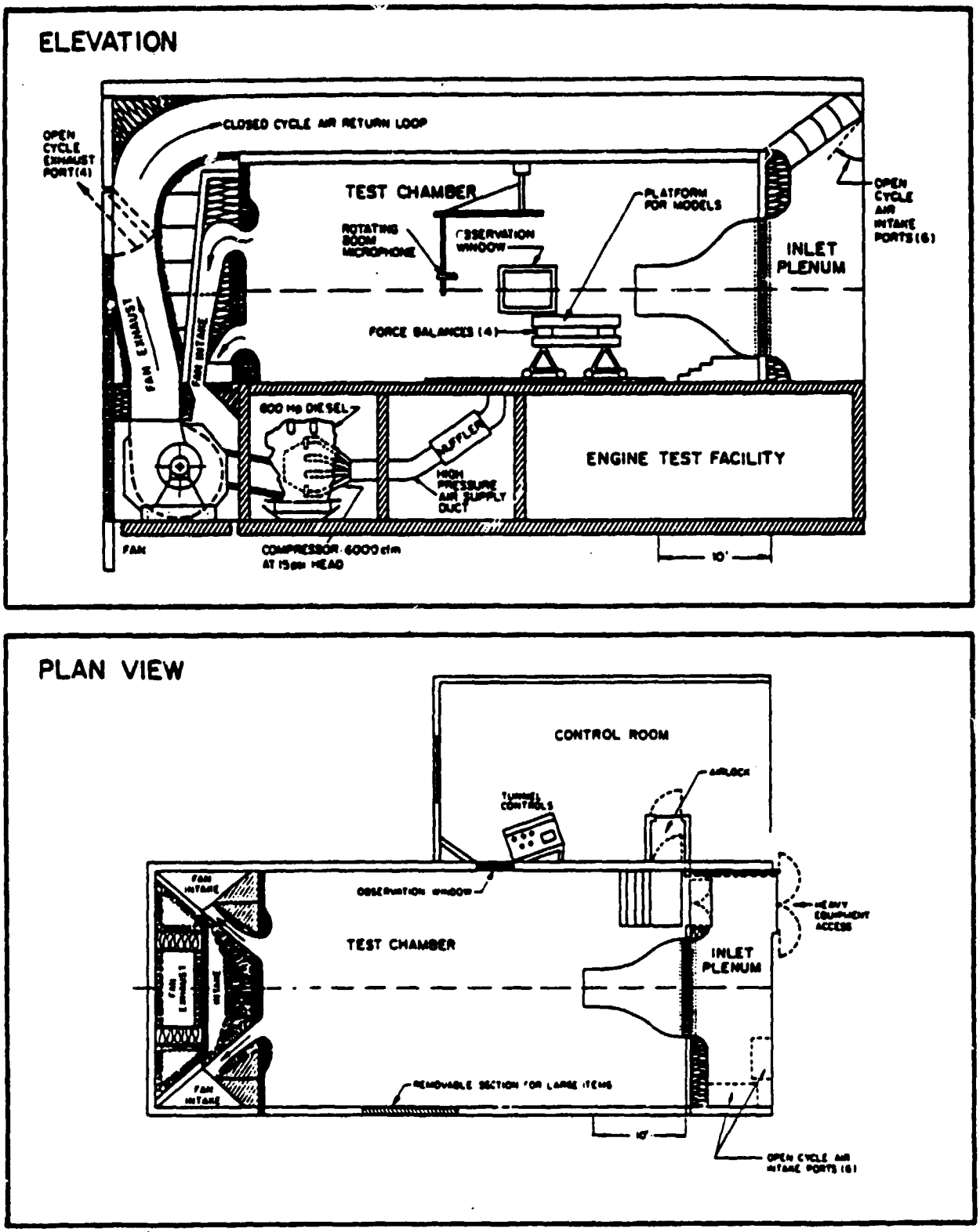

FIG. 2. BBN HIGH-SPEED ACOUSTIC WIND TUNNEL.

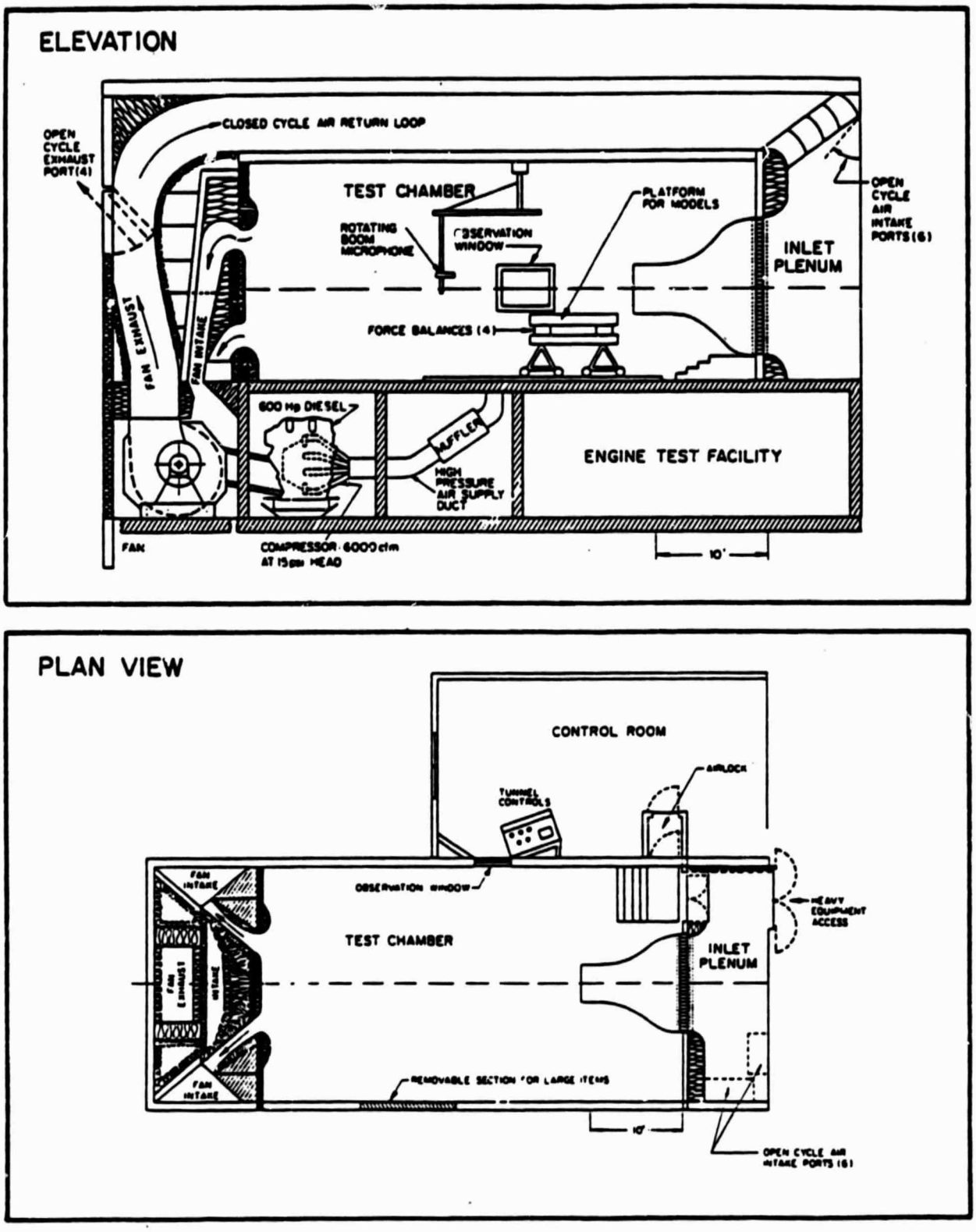

FIG. 2. BBN HIGH-SPEED ACOUSTIC WIND TUNNEL.

FIG. 3. ARRANGEMENT OF THE EXPERIMENT IN THE WIND TUNNEL CHAMBER.

FIG. 4. ACOUSTIC TREATMENT OF THE OPEN JET NOZZLE FLANGE AND THE VORTEX GENERATOR.

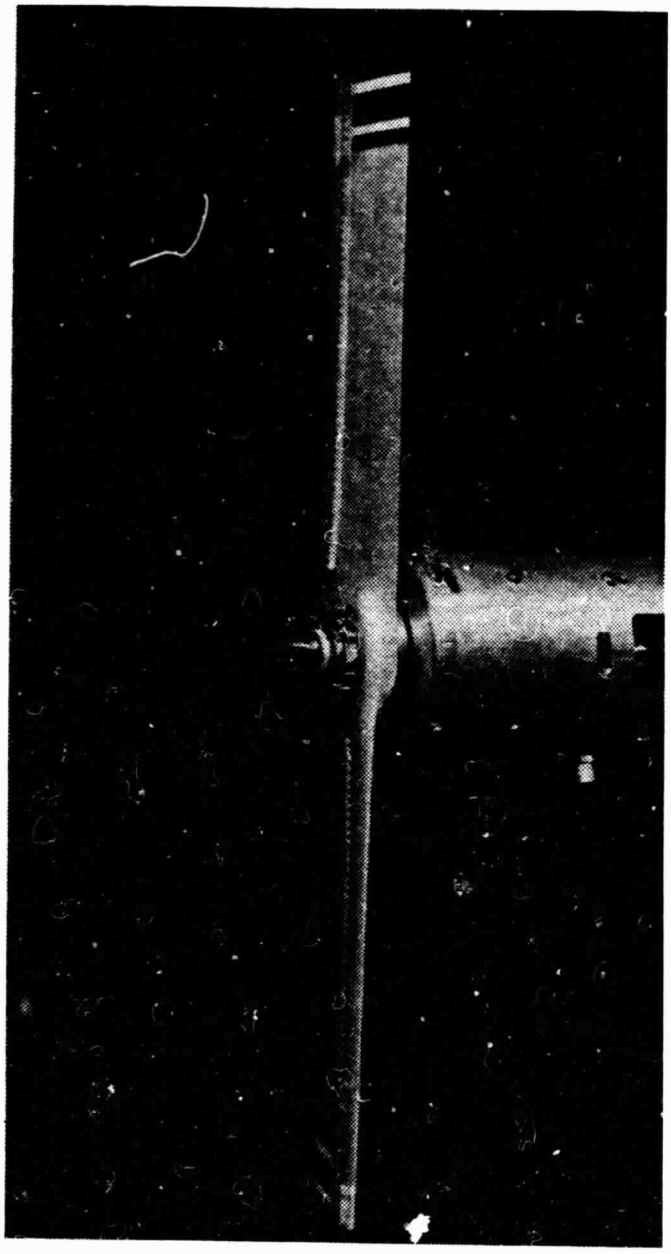

FIG. 5. MODEL ROTOR MOUNTED ON THE SPINNER RIG.

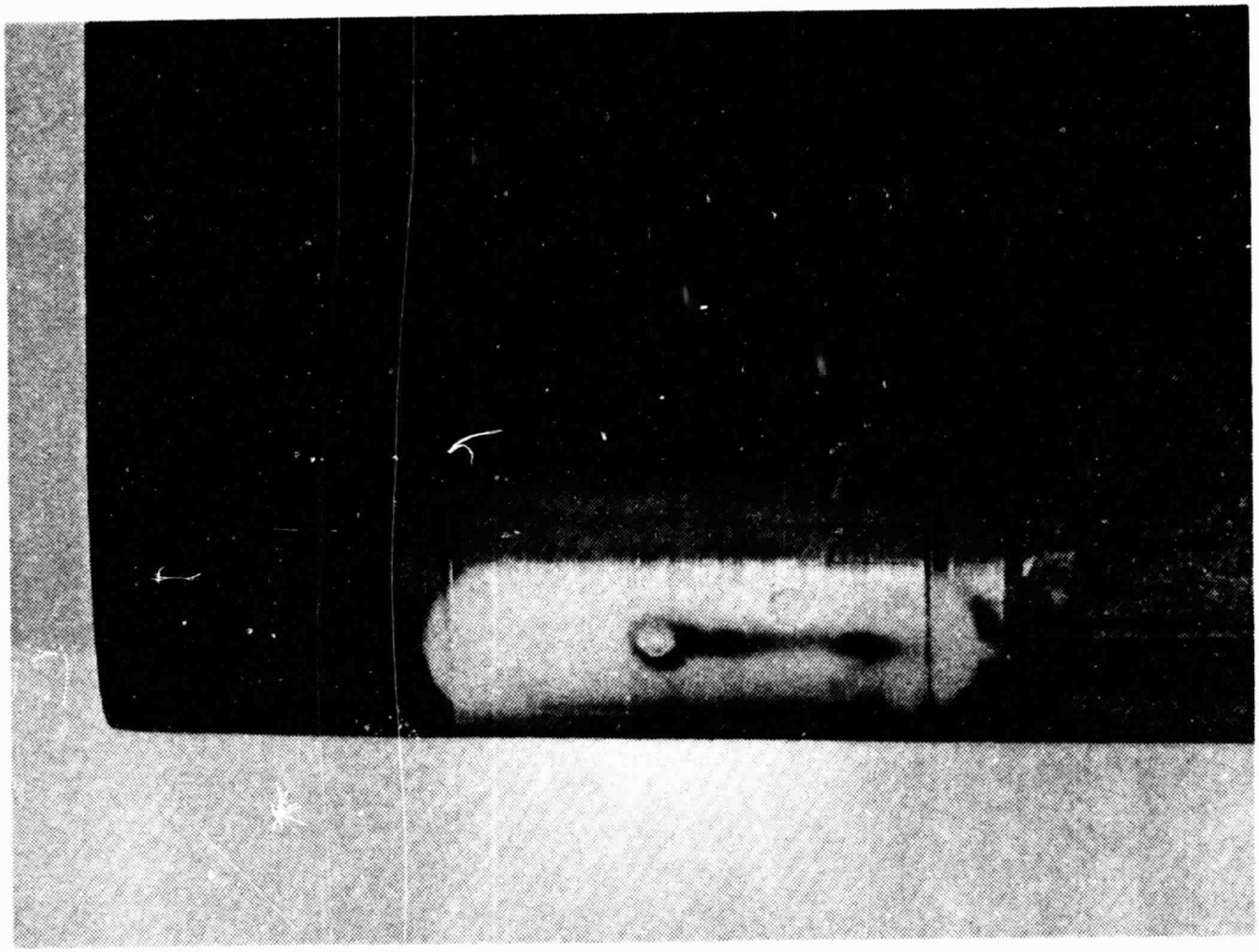

FIG. 6. CLOSEUP VIEW OF MINIATURE PRESSURE TRANSDUCER FLUSH MOUNTED NEAR THE LEADING EDGE OF ROTOR BLADE AT 90% RADIUS.

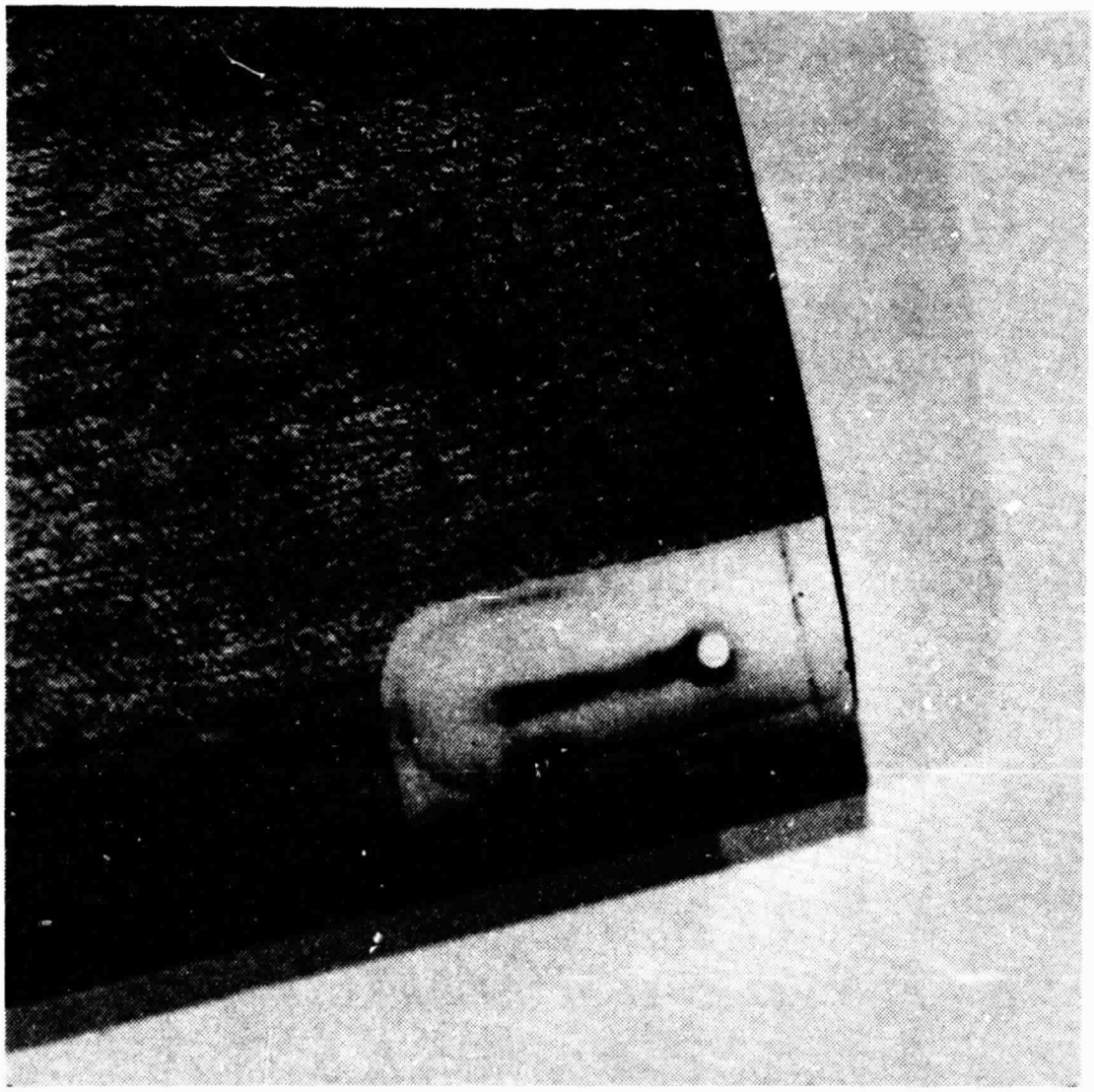

FIG. 7. CLOSEUP VIEW OF MINIATURE PRESSURE TRANSDUCER FLUSH MOUNTED NEAR THE LEADING EDGE OF ROTOR BLADE AT 97.5% RADIUS.

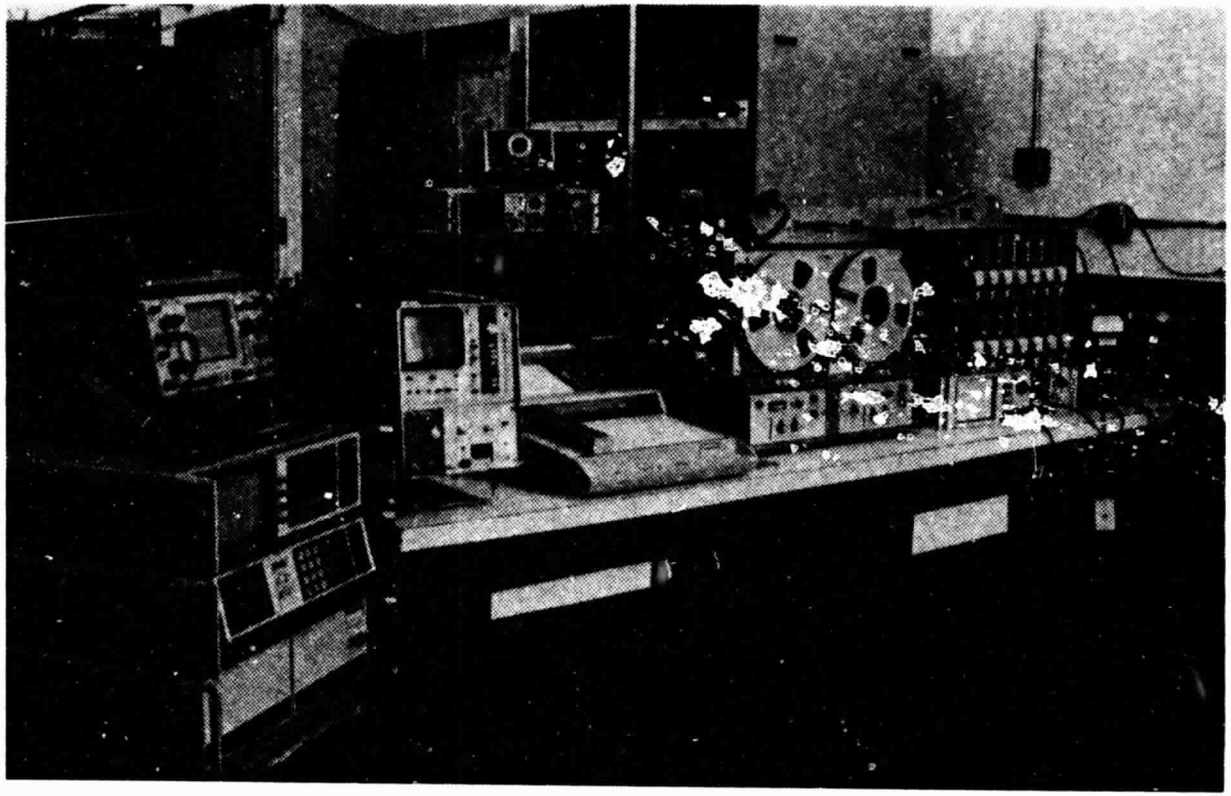

FIG. 8. ACOUSTIC WIND TUNNEL CONTROL ROOM WITH DATA ACQUISITION AND PROCESSING EQUIPMENT.

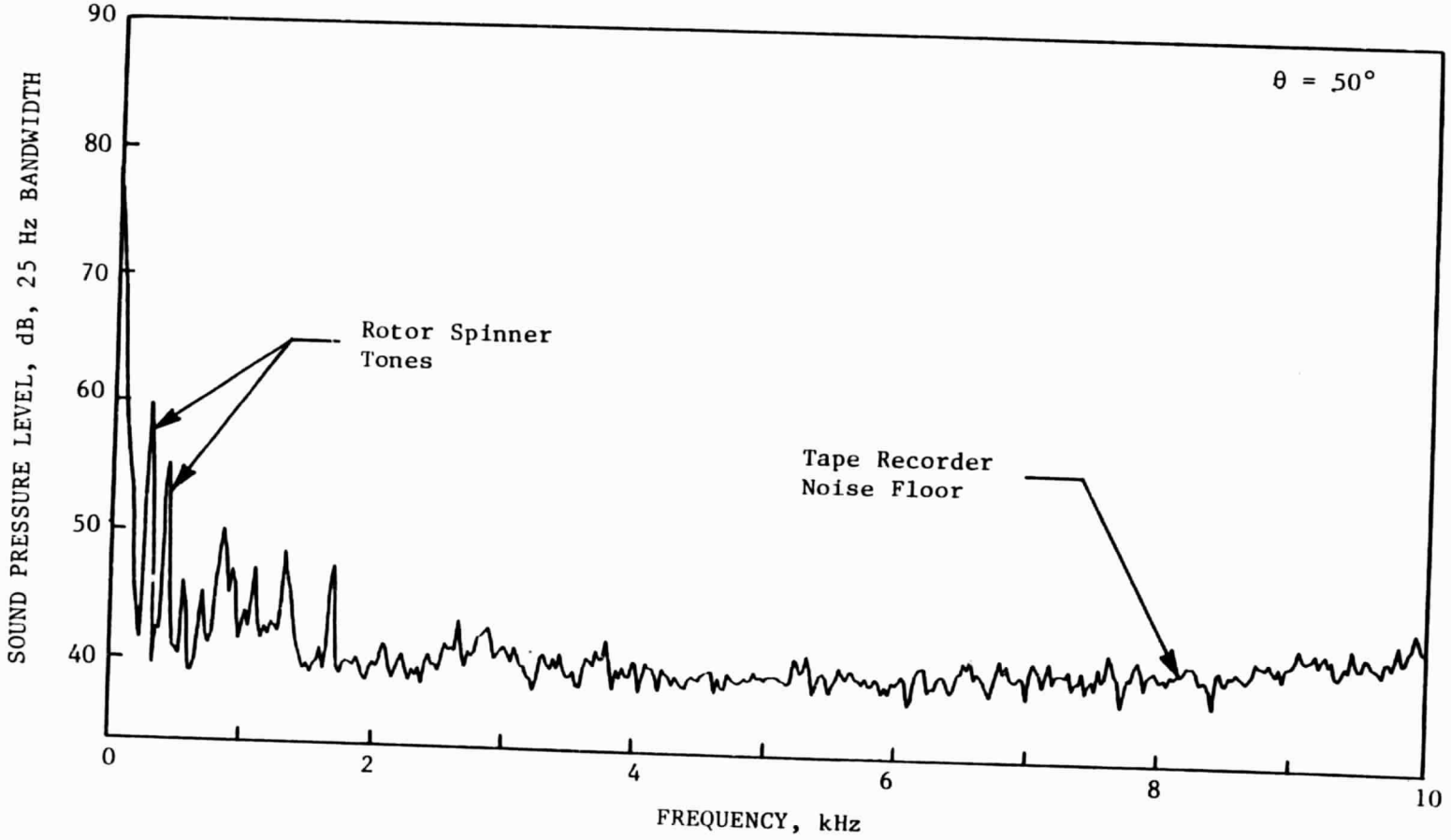

FIG. 9. SPECTRUM OF BACKGROUND NOISE WITH WIND TUNNEL AND SPINNER RIG OPERATING (ROTOR AND VORTEX GENERATOR REMOVED), CORRESPONDING TO TEST CONDITIONS 1 AND 4 (M_T = 0.55, U_∞ = 9.1 m/s).

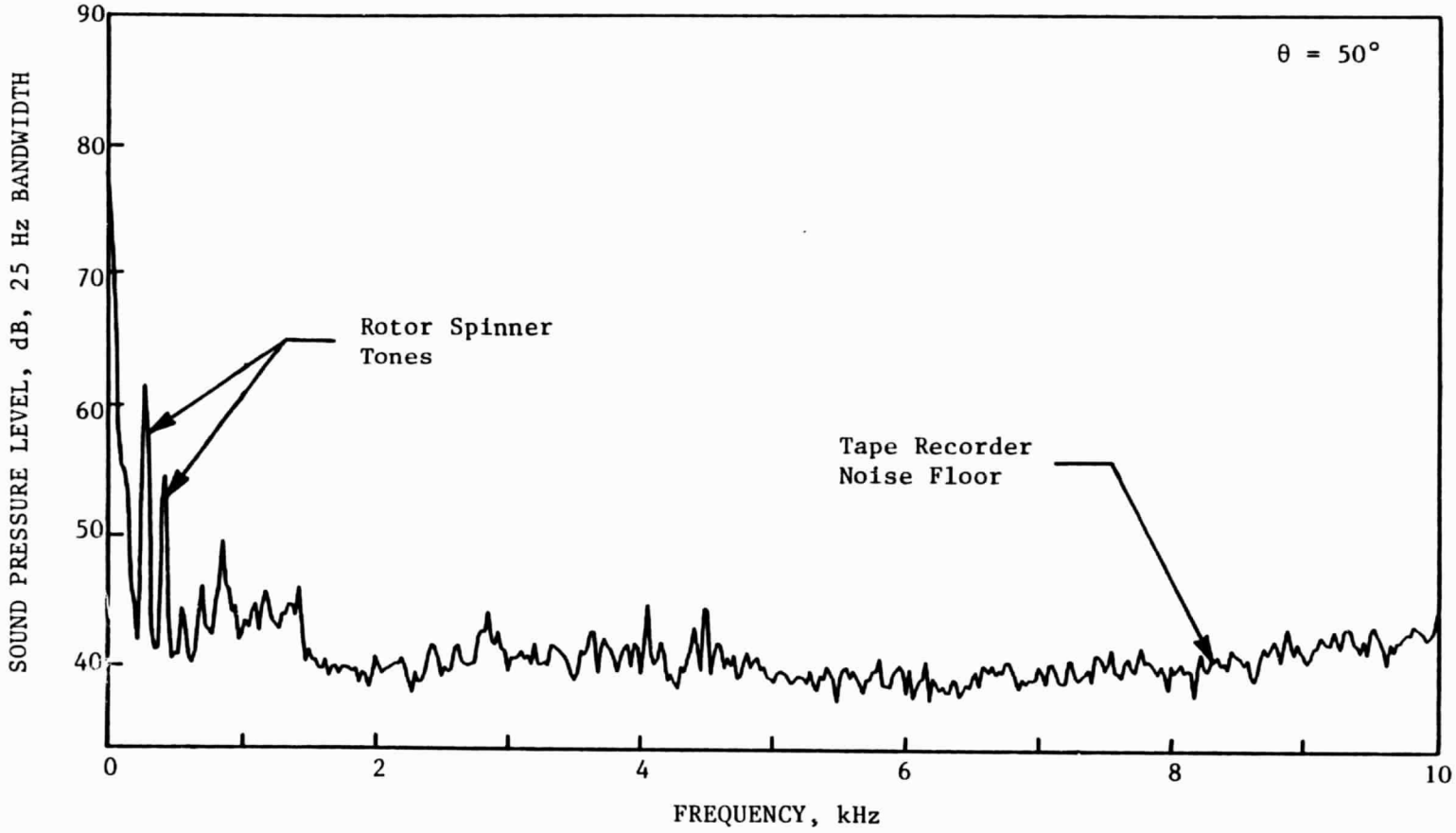

FIG. 10 . SPECTRUM OF BACKGROUND NOISE WITH WIND TUNNEL AND SPINNER RIG OPERATING (ROTOR AND VORTEX GENERATOR REMOVED), CORRESPONDING TO TEST CONDITIONS 2 AND 5 (M_T = 0.59, U_∞ = 8.2 m/s).

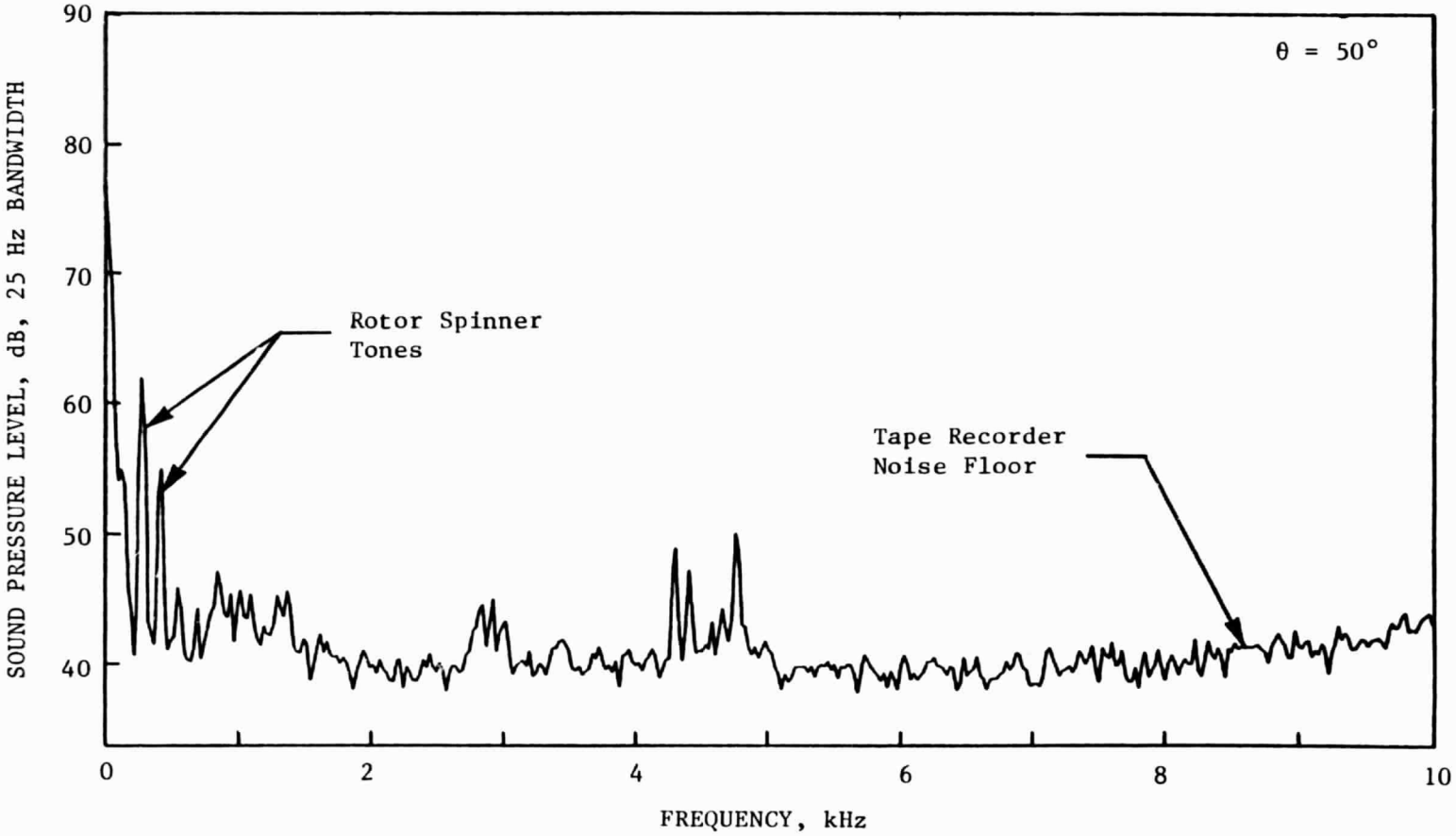

FIG. 11. SPECTRUM OF BACKGROUND NOISE WITH WIND TUNNEL AND SPINNER RIG OPERATING (ROTOR AND VORTEX GENERATOR REMOVED), CORRESPONDING TO TEST CONDITIONS 3 AND 6 (M_T = 0.63, U_∞ = 7.3 m/s).

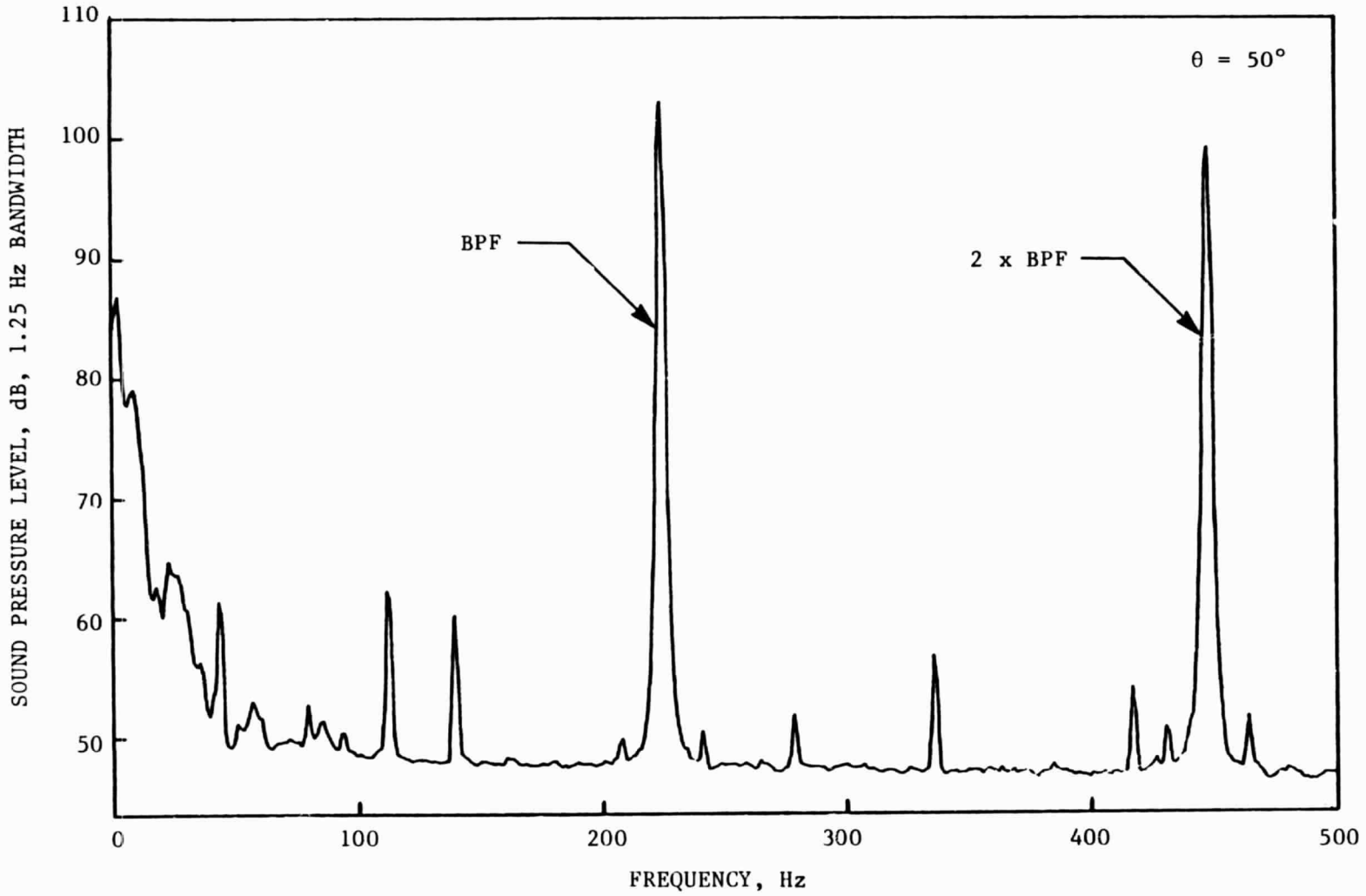

FIG. 12. LONG-TIME-AVERAGE (3 min 25 sec) ROTOR ACOUSTIC SPECTRUM DEMONSTRATING STEADINESS OF SHAFT ROTATION RATE, TEST CONDITION 3 (r_I/R = 0.90, M_T = 0.63, U_∞ = 7.3 m/s).

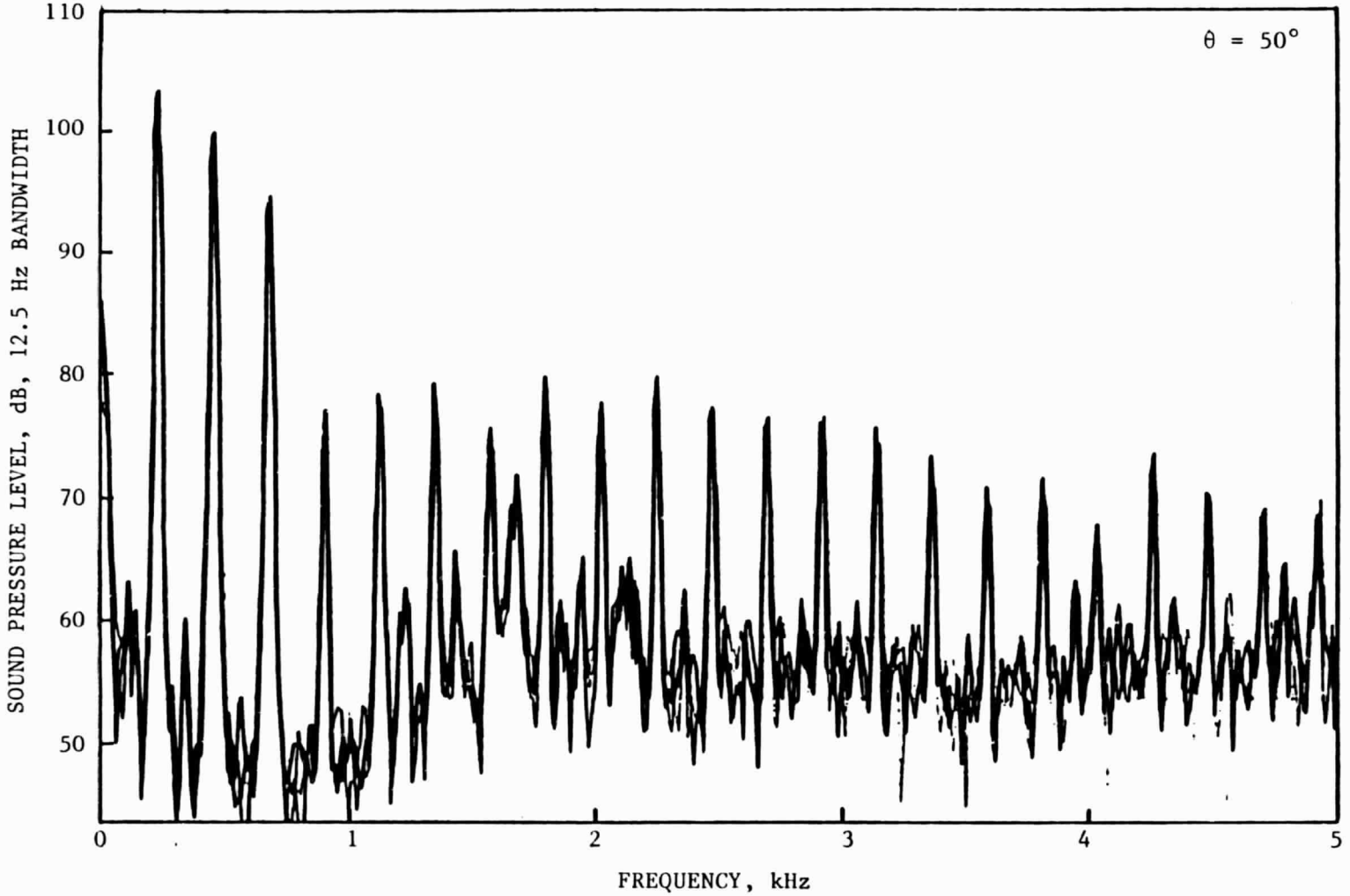

FIG. 13. SUPERPOSITION OF THREE SHORT-TIME-AVERAGE (0.32 Sec) ROTOR ACOUSTIC SPECTRA FROM THE BEGINNING, MIDDLE AND END OF THE RECORD FOR TEST CONDITION 3 (r_T/R = 0.90, M_T = 0.63, U_∞ = 7.3 m/s) DEMONSTRATING OVERALL STEADINESS OF THE EXPERIMENT.

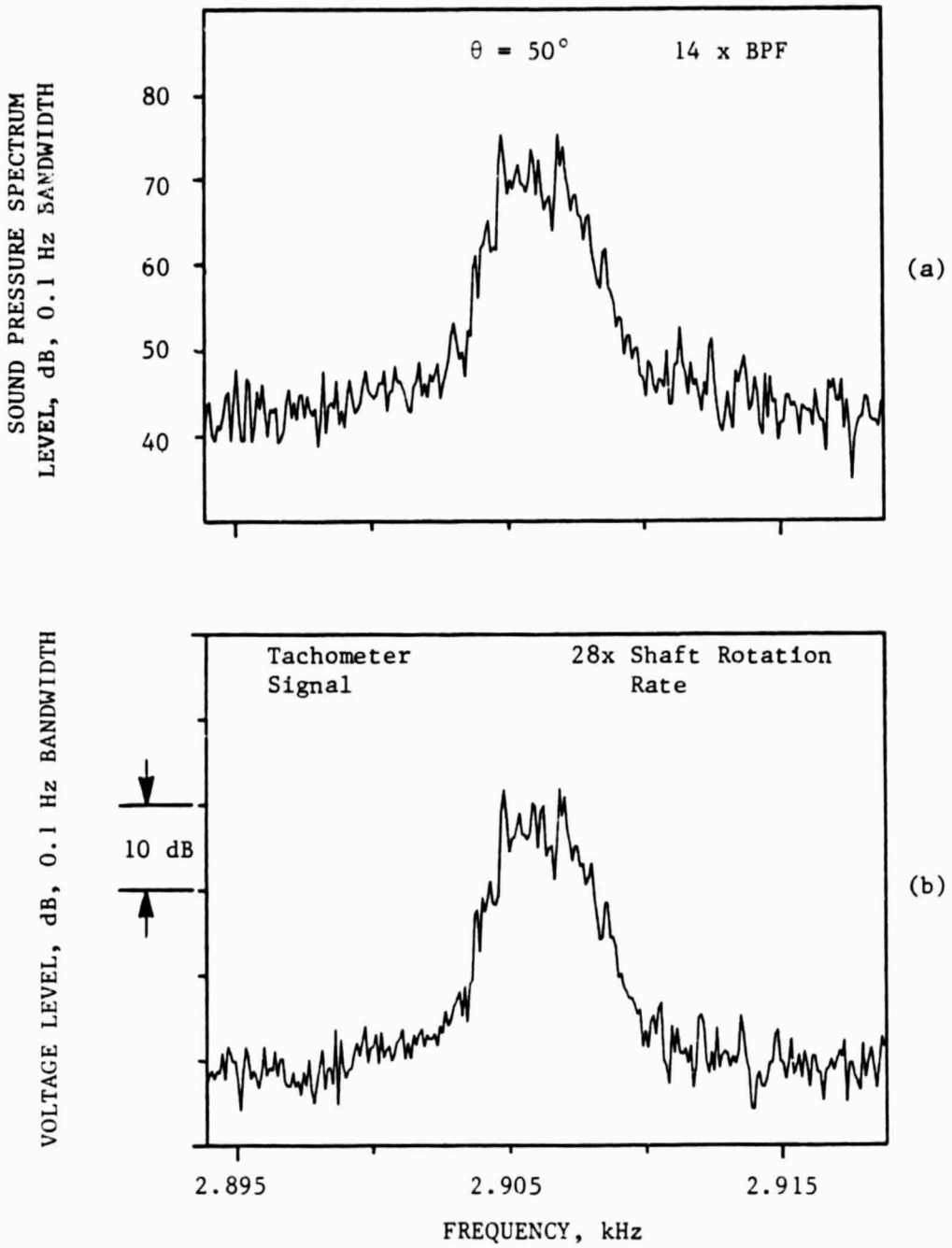

FIG. 14. HIGH RESOLUTION SPECTRA OF (a) NARROWBAND RANDOM TONES OF ROTOR NOISE AND (b) ROTOR TACHOMETER SIGNAL, TEST CONDITION 3 (r_I/R = 0.90, M_T = 0.63, U_∞ = 7.3 m/s).

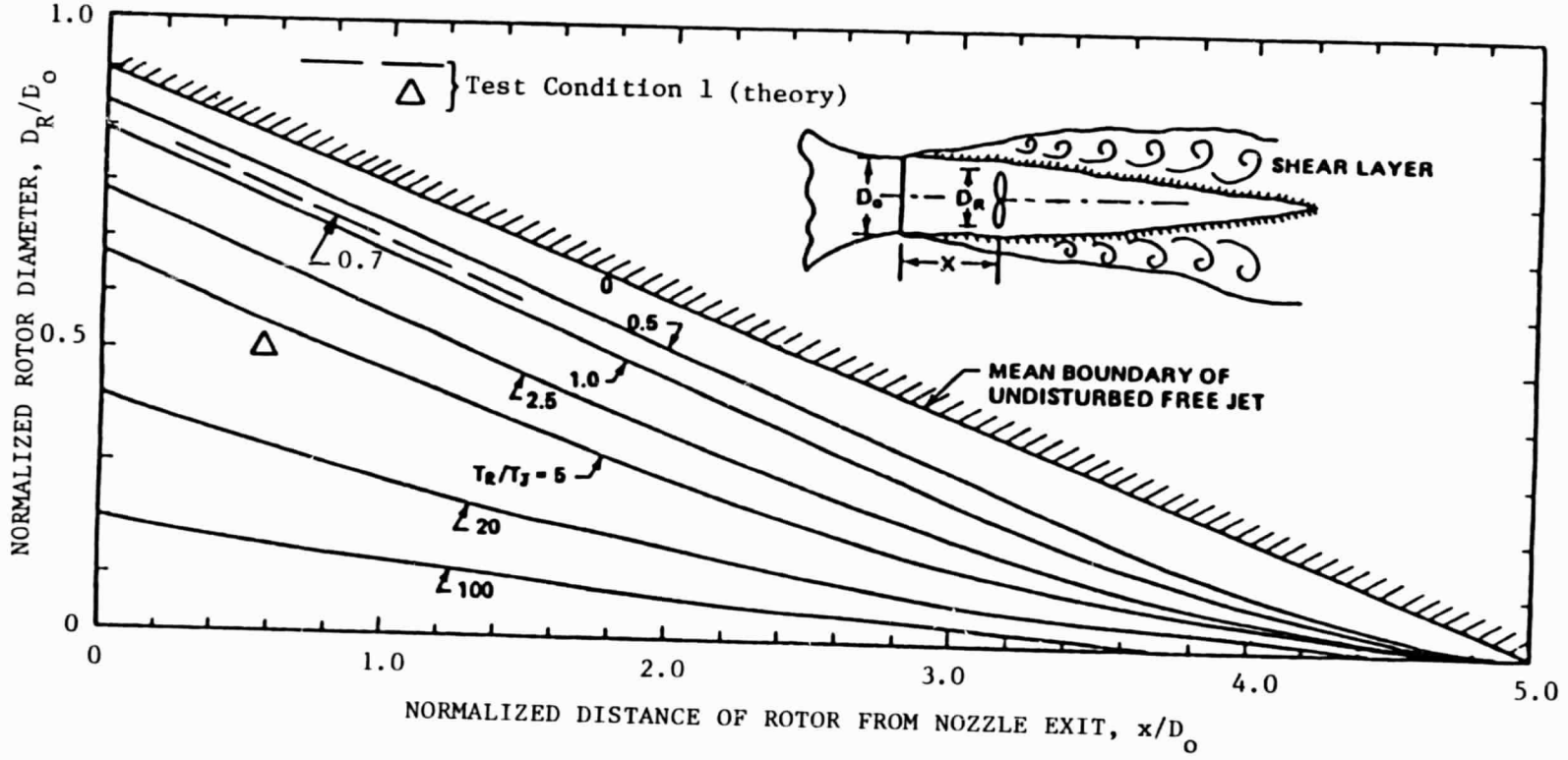

FIG. 15. THEORETICAL SHEAR LAYER INJESTION BOUNDARIES FOR A ROTOR IN A FREE JET.

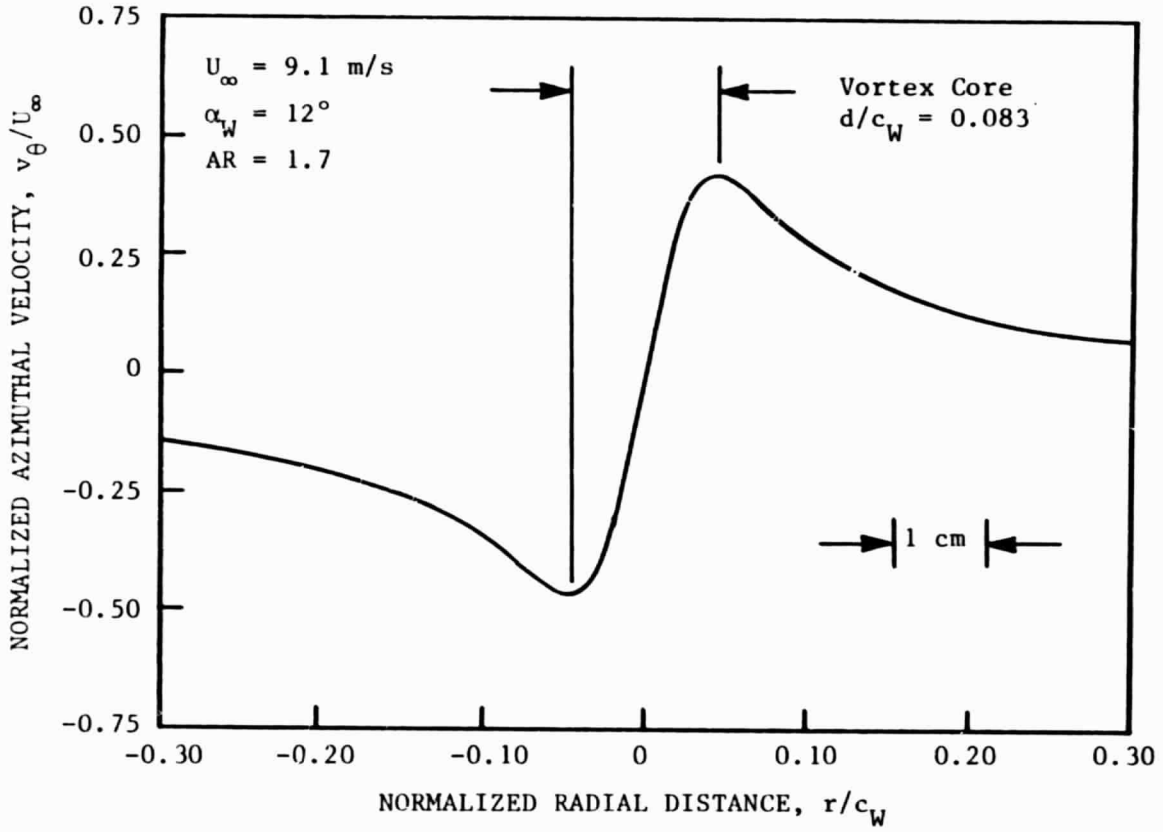

FIG. 16. RADIAL DISTRIBUTION OF VORTEX AZIMUTHAL VELOCITY THREE CHORD LENGTHS DOWNSTREAM OF VORTEX GENERATOR TRAILING EDGE.

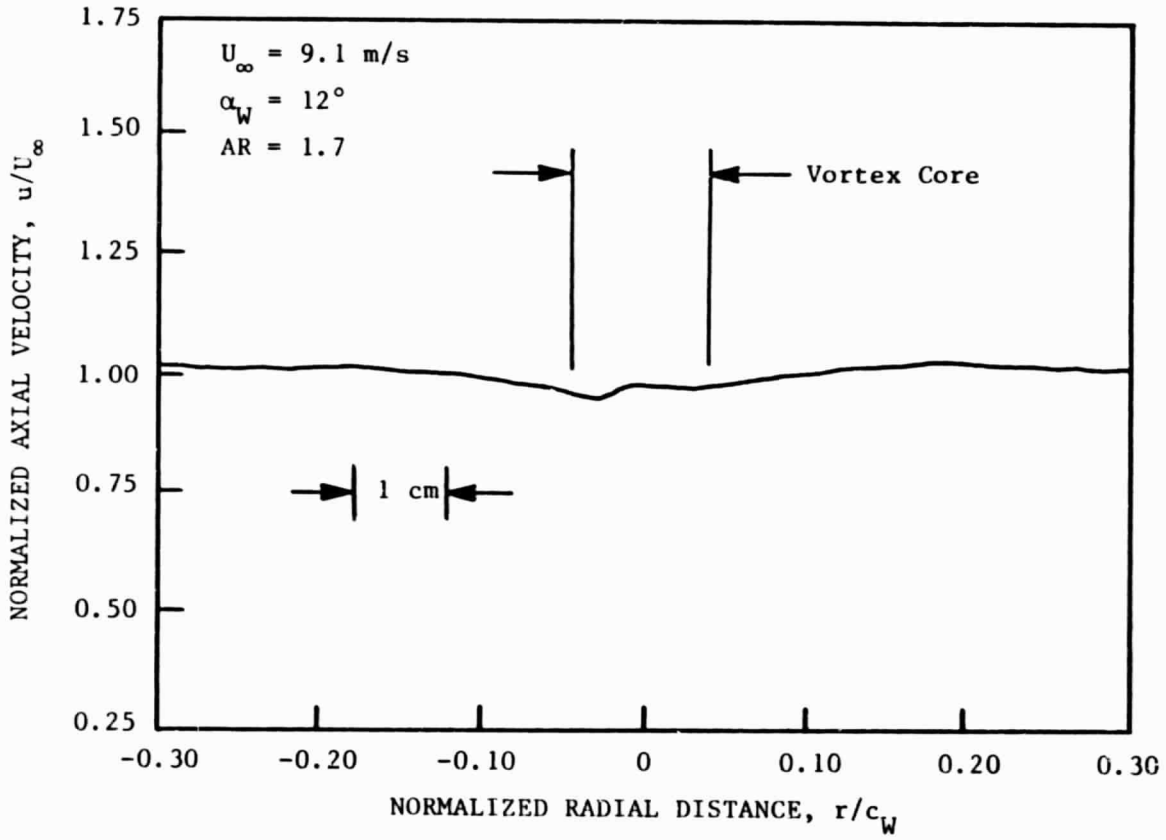

FIG. 17. RADIAL DISTRIBUTION OF AXIAL VELOCITY THROUGH THE VORTEX CENTER THREE CHORD LENGTHS DOWNSTREAM OF VORTEX GENERATOR TRAILING EDGE.

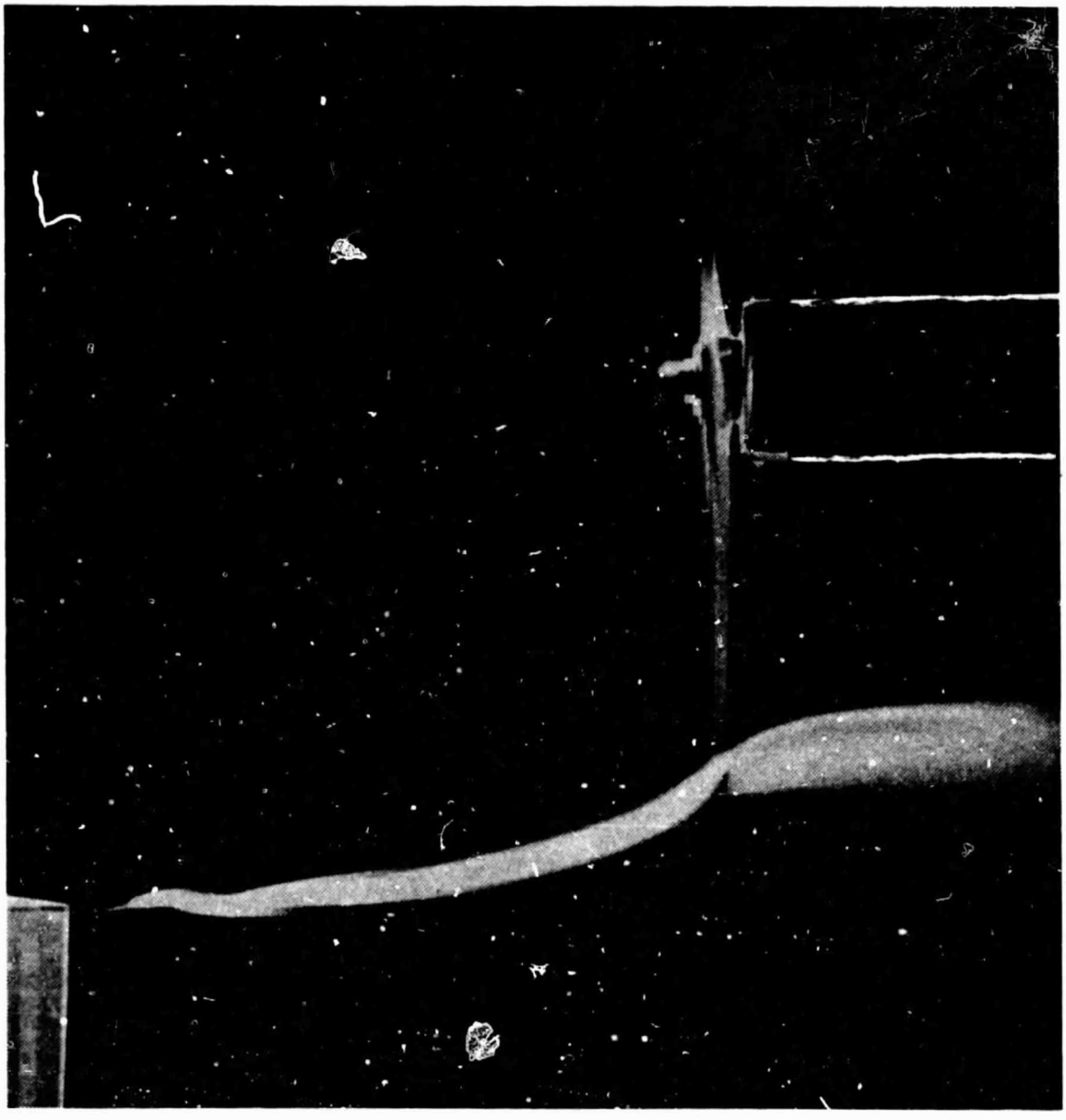

FIG. 18. FLOW VISUALIZATION OF BLADE-VORTEX INTERACTION IN SIDE VIEW, TEST CONDITION 3 (r_i/R = 0.90, M_T = 0.63, U_∞ = 7.3 m/s).

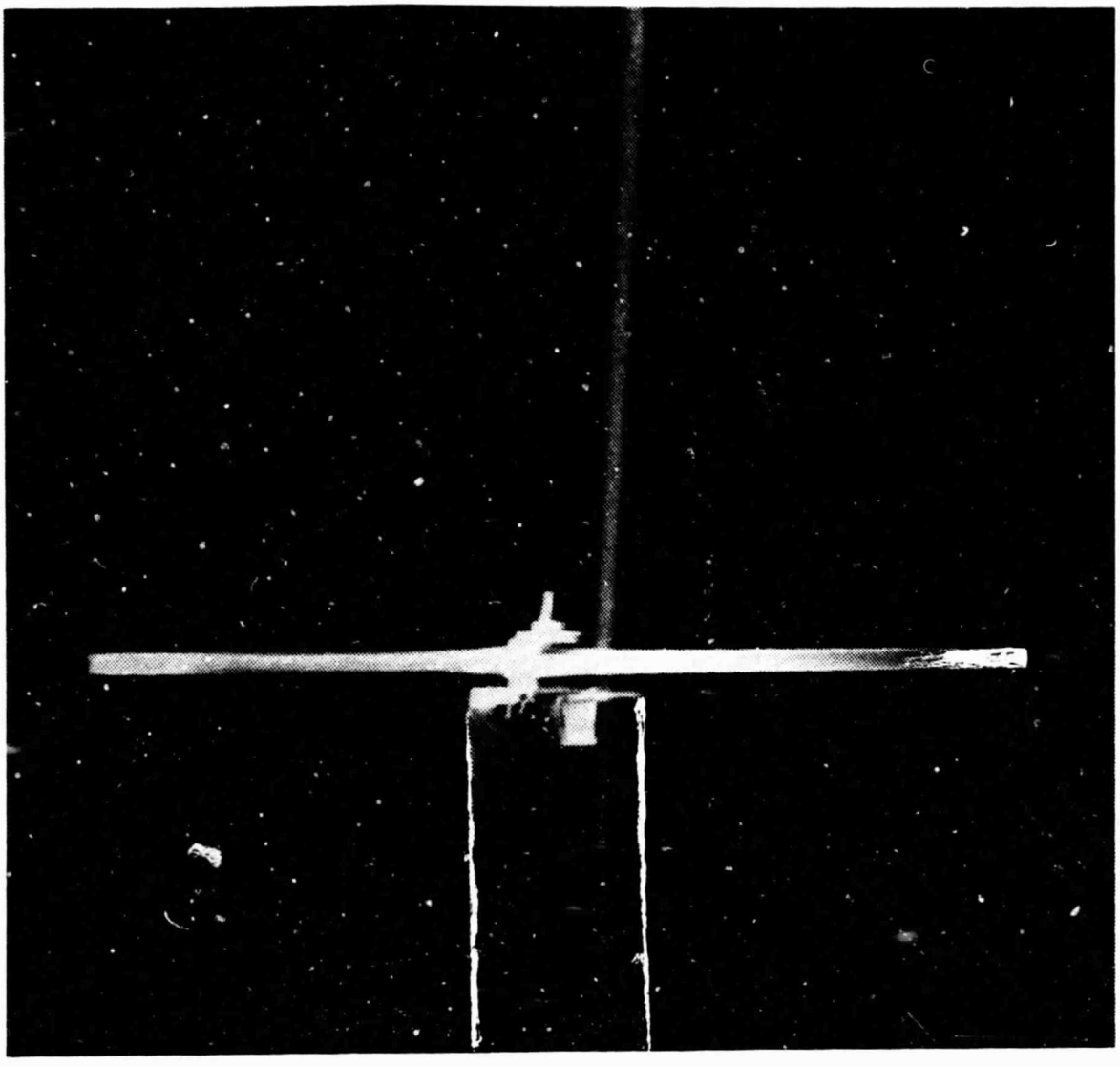

FIG. 19. FLOW VISUALIZATION OF BLADE-VORTEX INTERACTION IN BOTTOM VIEW, TEST CONDITION 1 (r_I/R = 0.90, M_T = 0.55, U_∞ = 9.1 m/s).

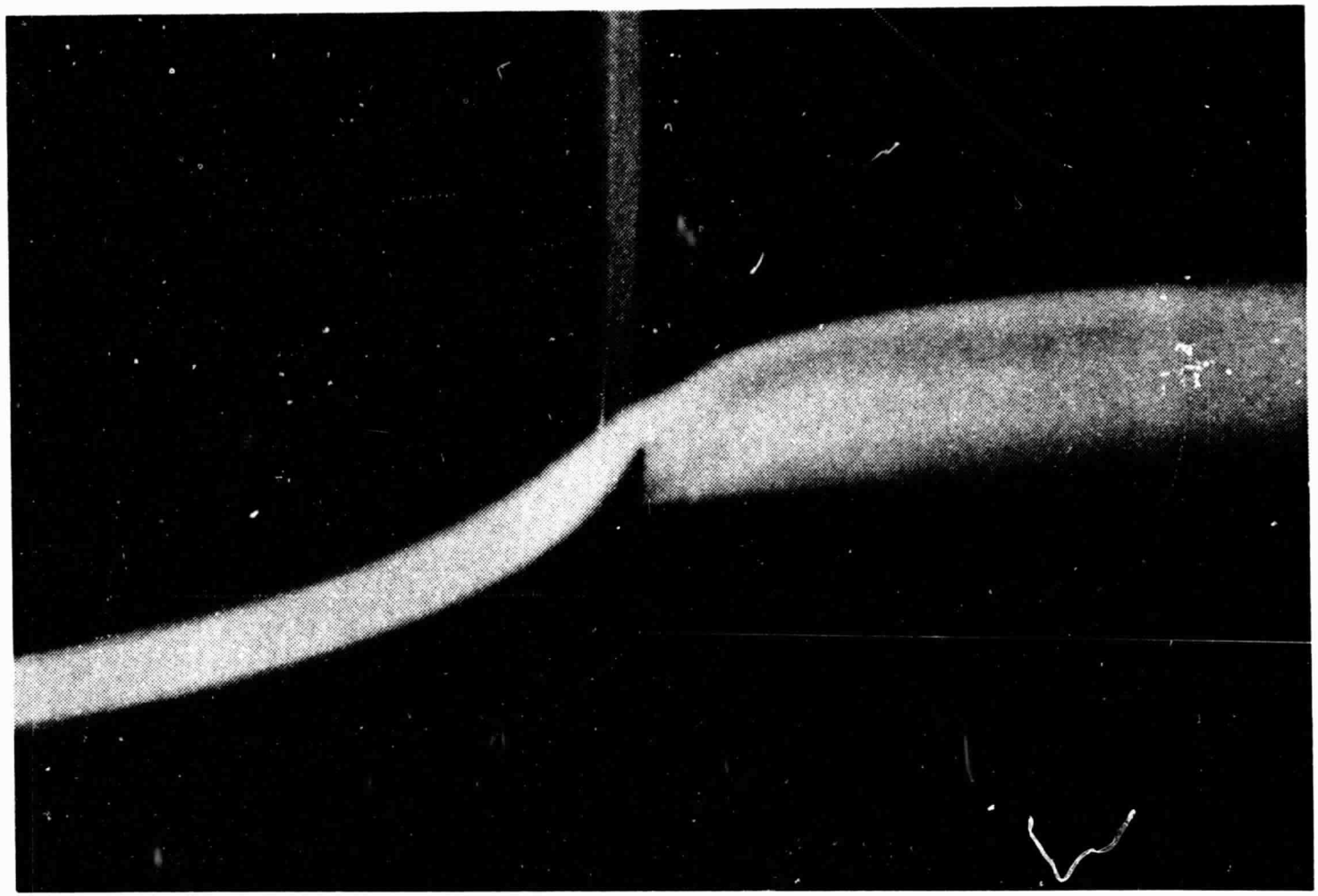

FIG. 20. CLOSEUP VIEW OF FLOW VISUALIZATION OF BLADE-VORTEX INTERACTION IN SIDE VIEW, TEST CONDITION 3 ($r_I/R = 0.90$, $M_T = 0.63$, $U_\infty = 7.3$ m/s).

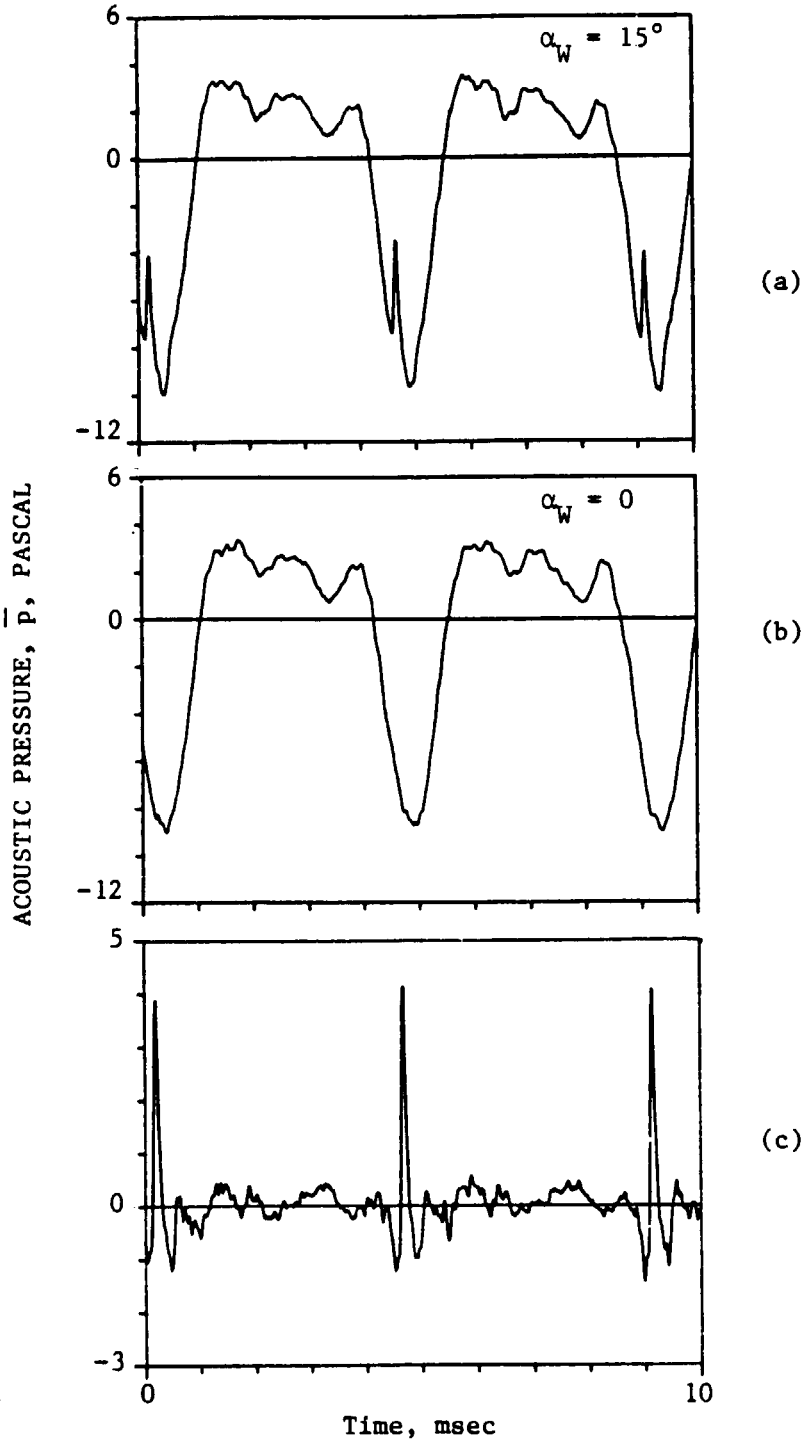

FIG. 21. ACOUSTIC WAVEFORMS (a,b) AND BVI SIGNATURE (c) FOR TEST CONDITION 3 (r_I/R = 0.90, M_T = 0.63, U_∞ = 7.3 m/s), θ = 50°.

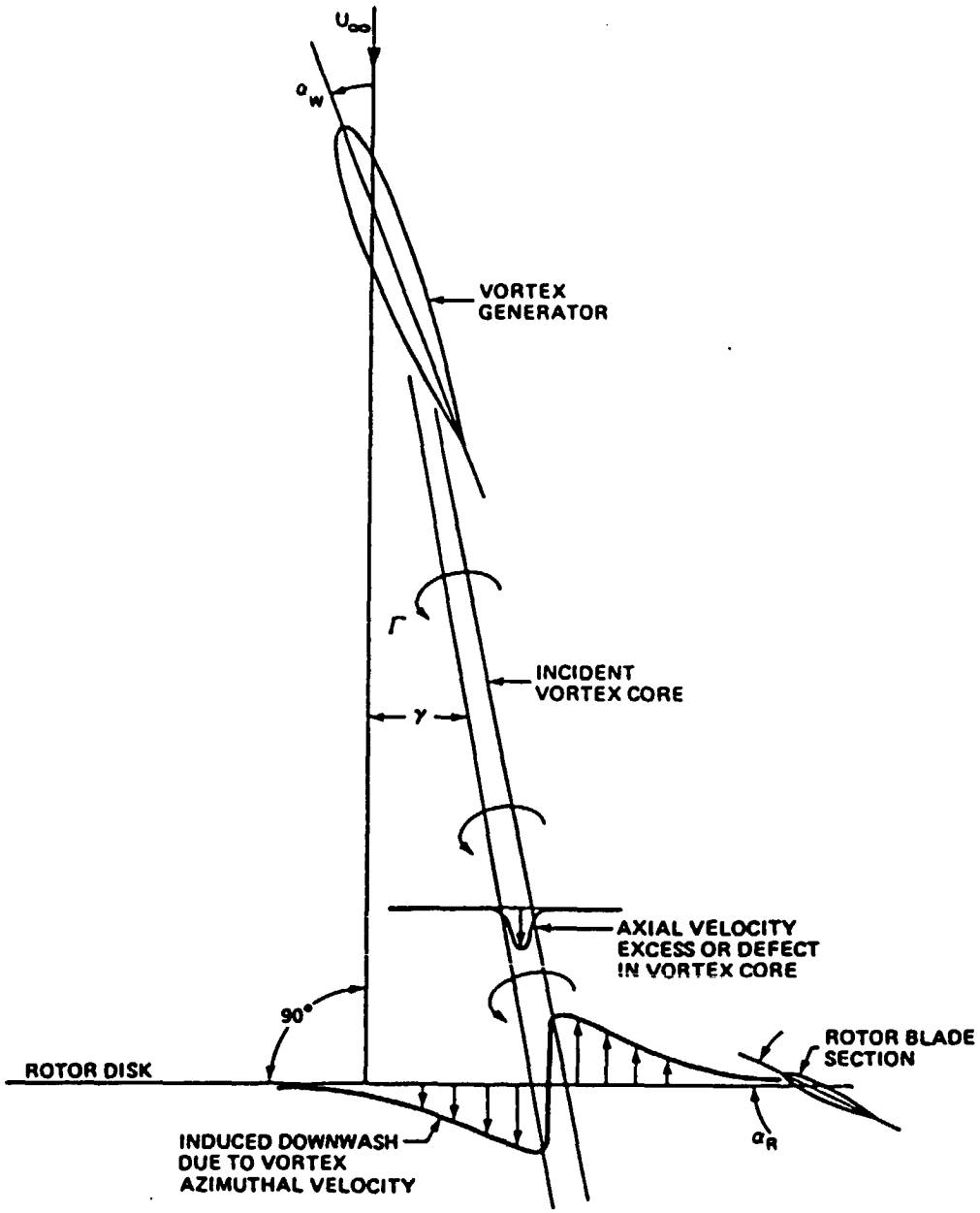

FIG. 22. SCHEMATIC OF BLADE-VORTEX INTERACTION AT NORMAL INCIDENCE.

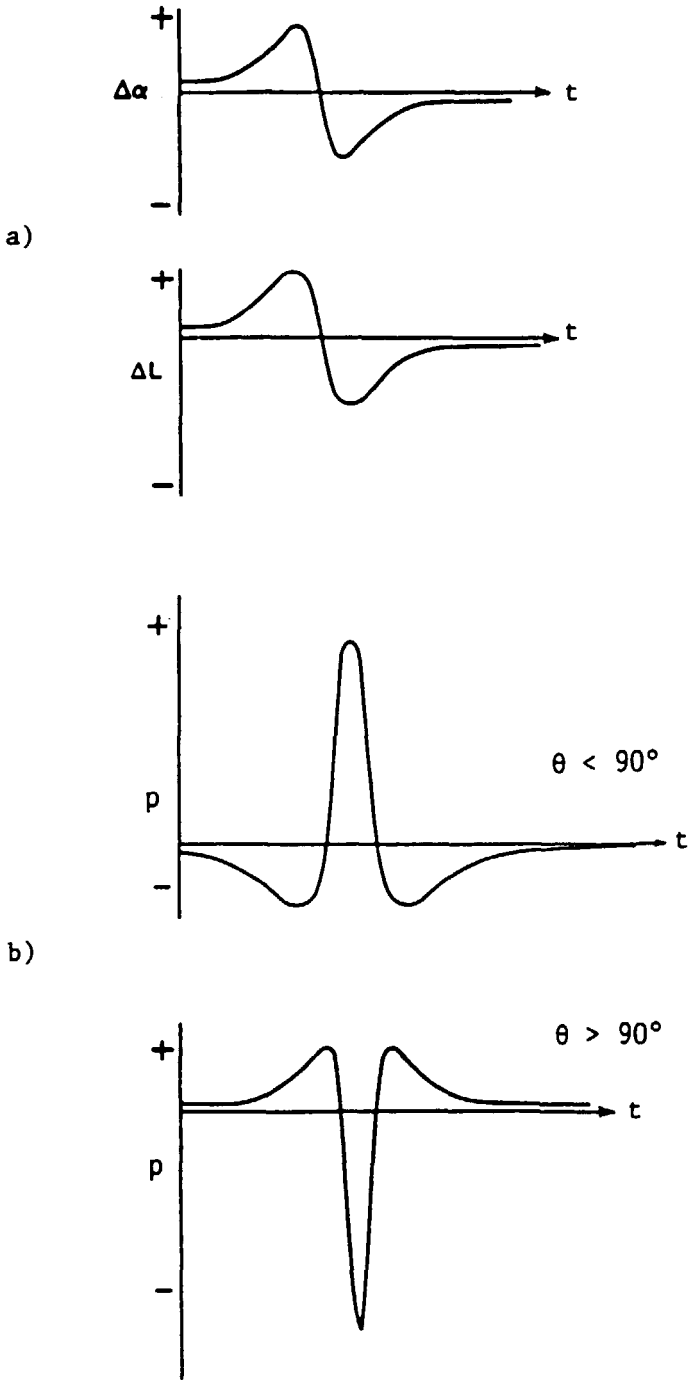

FIG. 23. ANGLE OF ATTACK AND LIFT FLUCTUATIONS (a), AND FARFIELD ACOUSTIC PRESSURE (b) DUE TO BLADE-VORTEX INTERACTION (after Ref. 1).

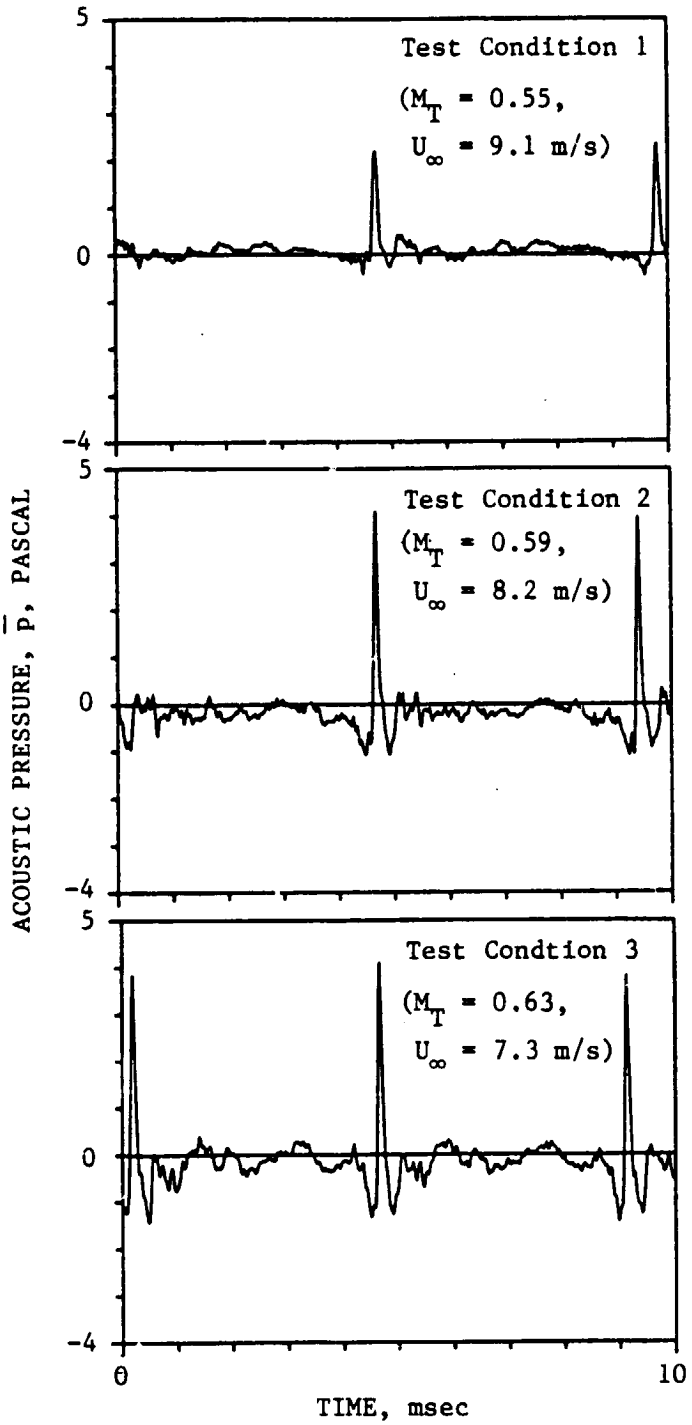

FIG. 24. BVI SIGNATURE AT θ = 50° FOR THREE DIFFERENT TEST CONDITIONS, r_I/R = 0.90.

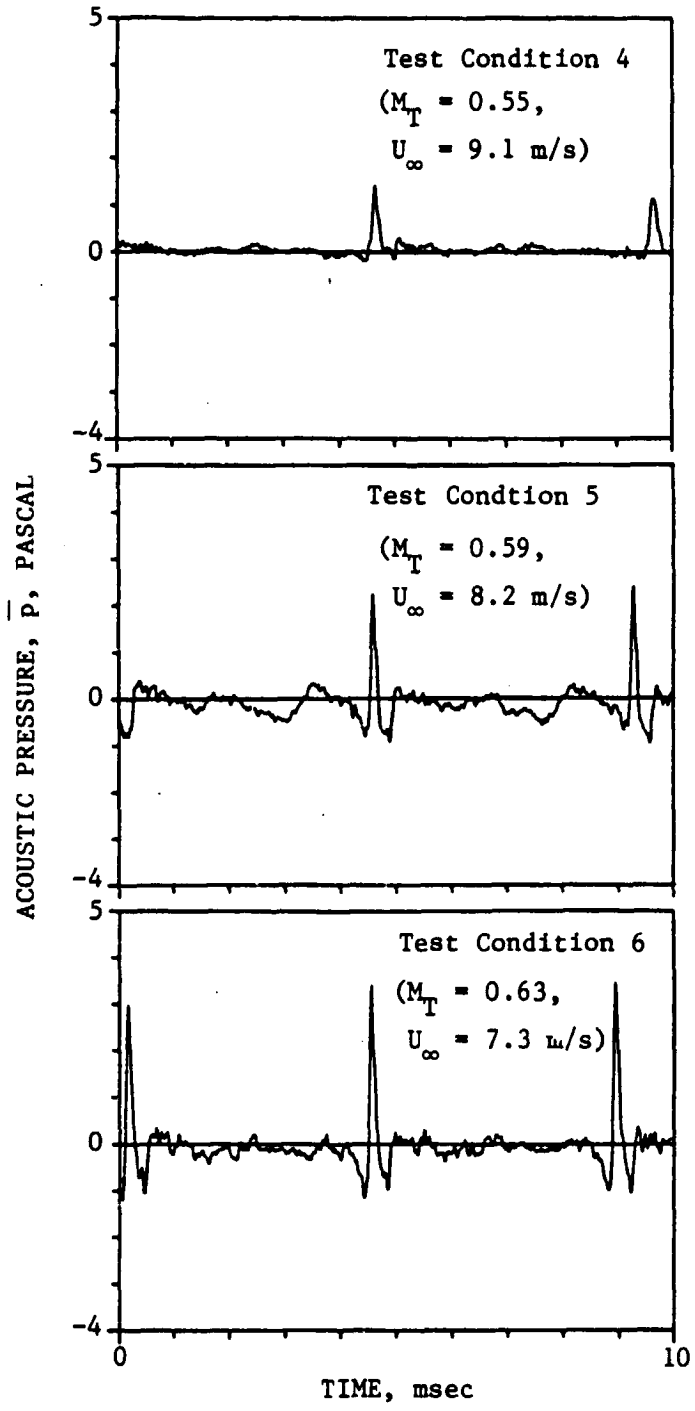

FIG. 25. BVI SIGNATURE AT θ = 50° FOR THREE DIFFERENT TEST CONDITIONS, r_I/R = 0.975.

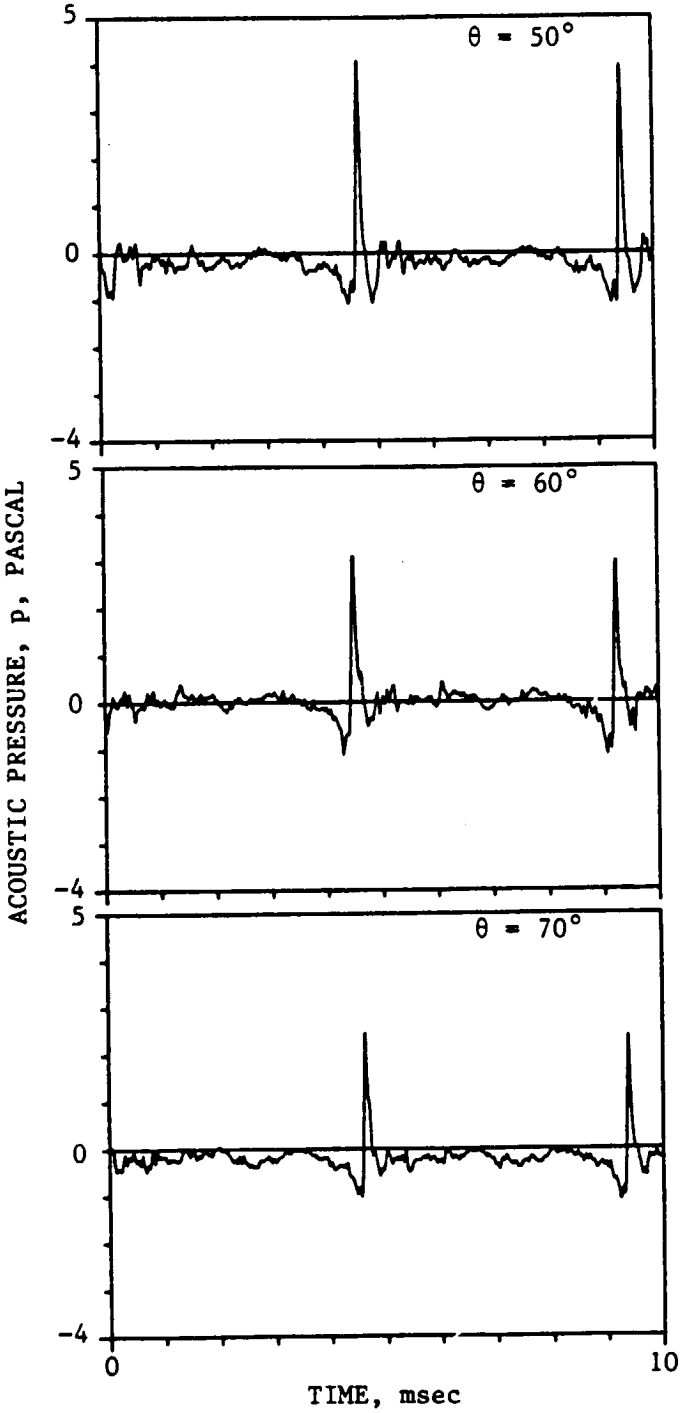

FIG. 26. BVI SIGNATURE AT DIFFERENT AZIMUTHAL POSITIONS FOR TEST CONDITION 2 (r_I/R = 0.90, M_T = 0.59, U_∞ = 8.2 m/s), θ = 50° - 130°.

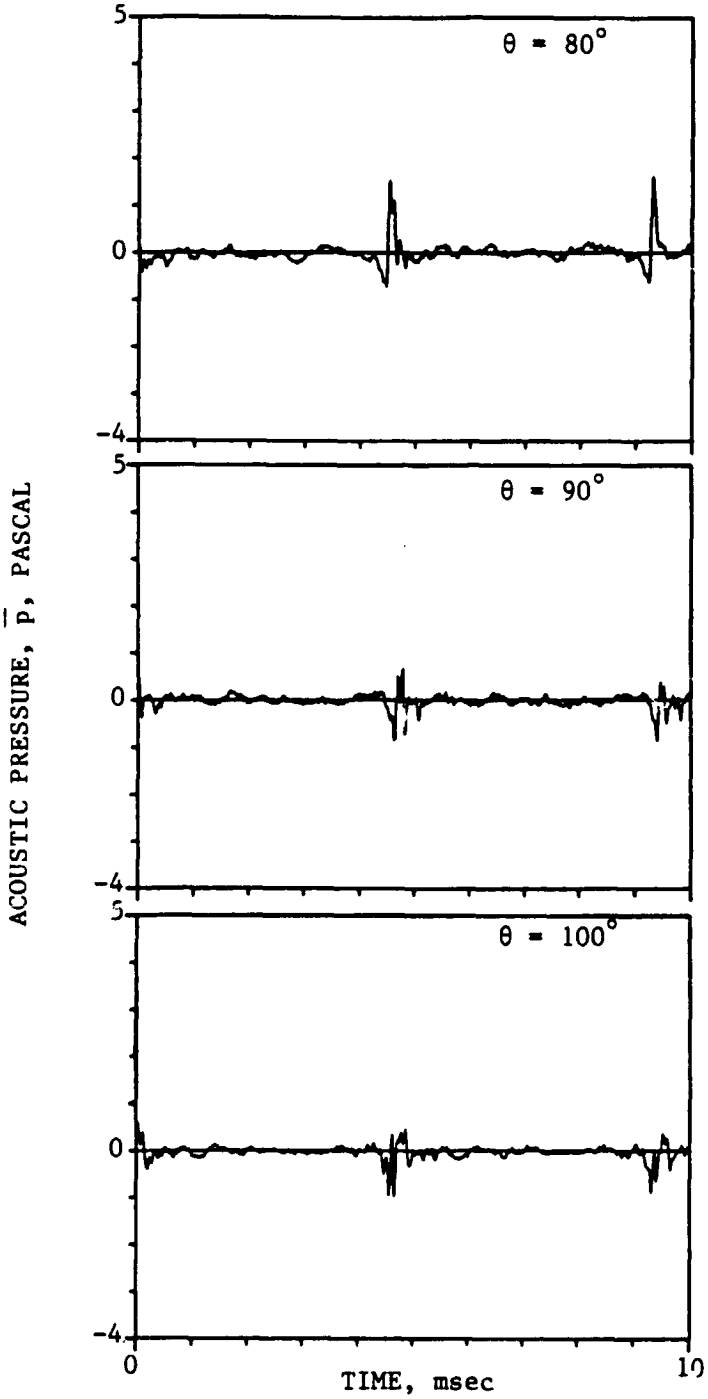
θ = 80°
θ = 90°
θ = 100°
5
0
-4
ACOUSTIC PRESSURE, $\bar{p}$, PASCAL
0
10
TIME, msec

FIG. 26. (CONT'D.).

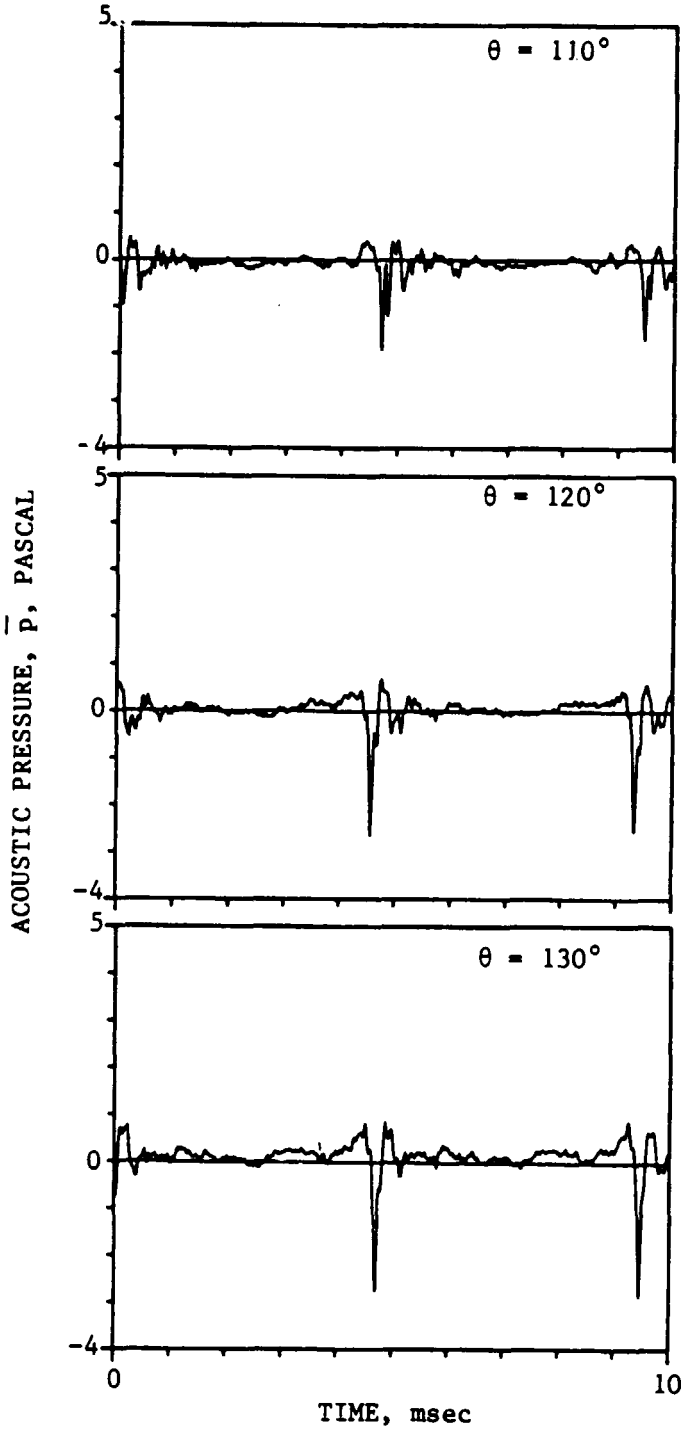
θ = 110°
θ = 120°
θ = 130°
5
0
-4
ACOUSTIC PRESSURE, $\bar{p}$, PASCAL
0
10
TIME, msec

FIG. 26. (CONT'D.).

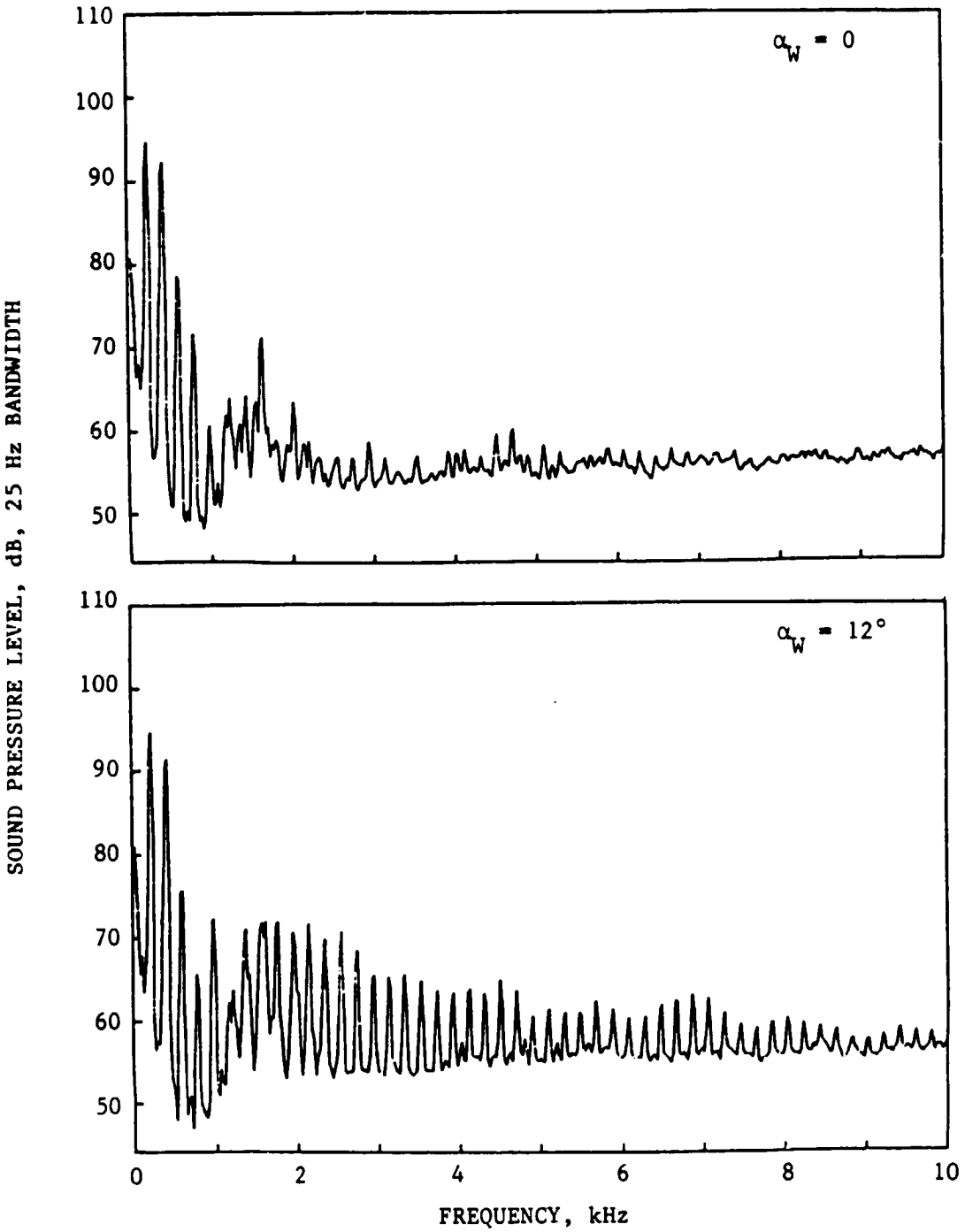

FIG. 27. EFFECT OF BLADE-VORTEX INTERACTION ON ROTOR ACOUSTIC SPECTRA FOR TEST CONDITION 1, (r_I/R = 0.90, M_T = 0.55, U_∞ = 9.1 m/s), θ = 50°.

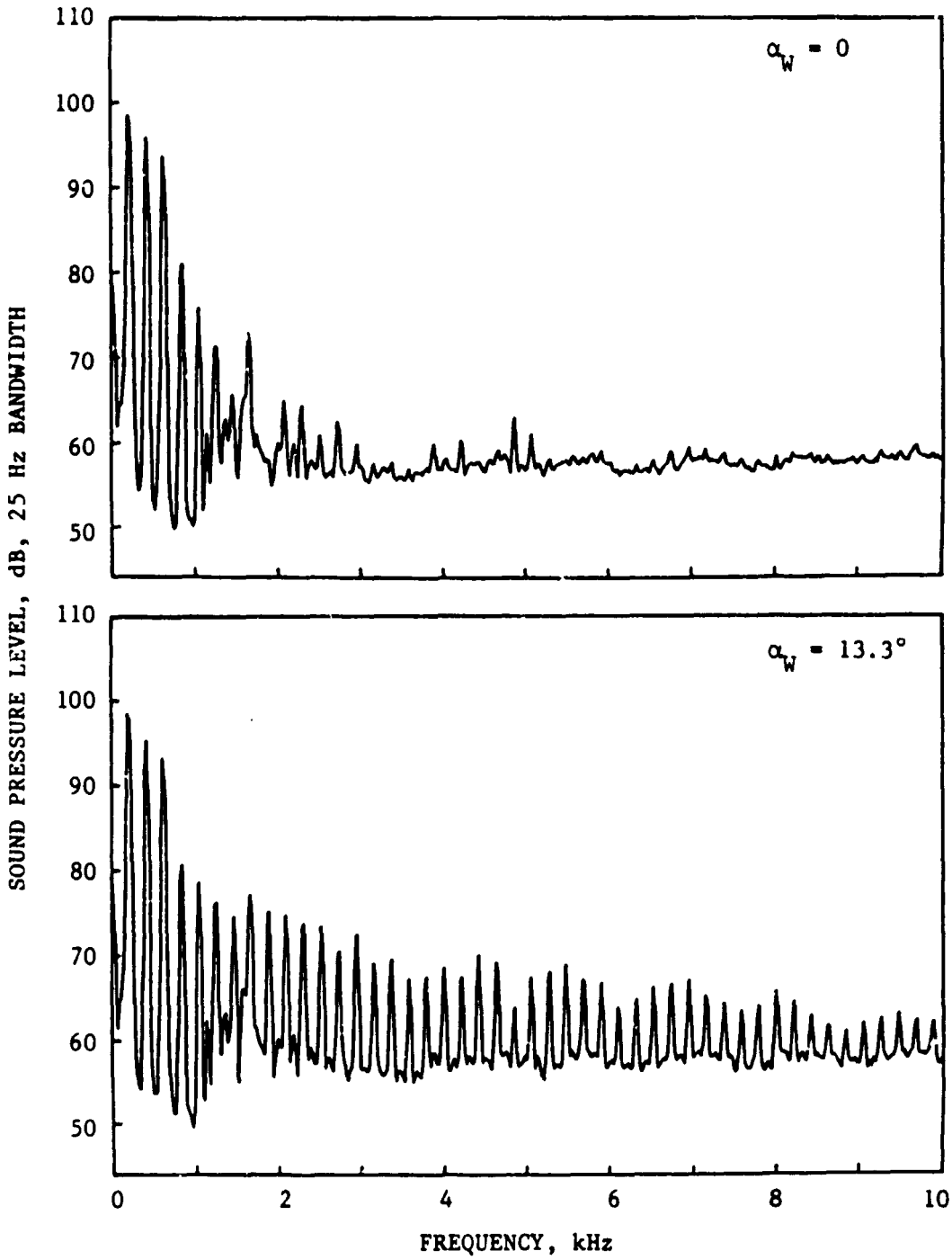

FIG. 28. EFFECT OF BLADE-VORTEX INTERACTION ON ROTOR ACOUSTIC SPECTRA FOR TEST CONDITION 2 (r_I/R = 0.90, M_T = 0.59, U_∞ = 8.2 m/s), θ = 50°.

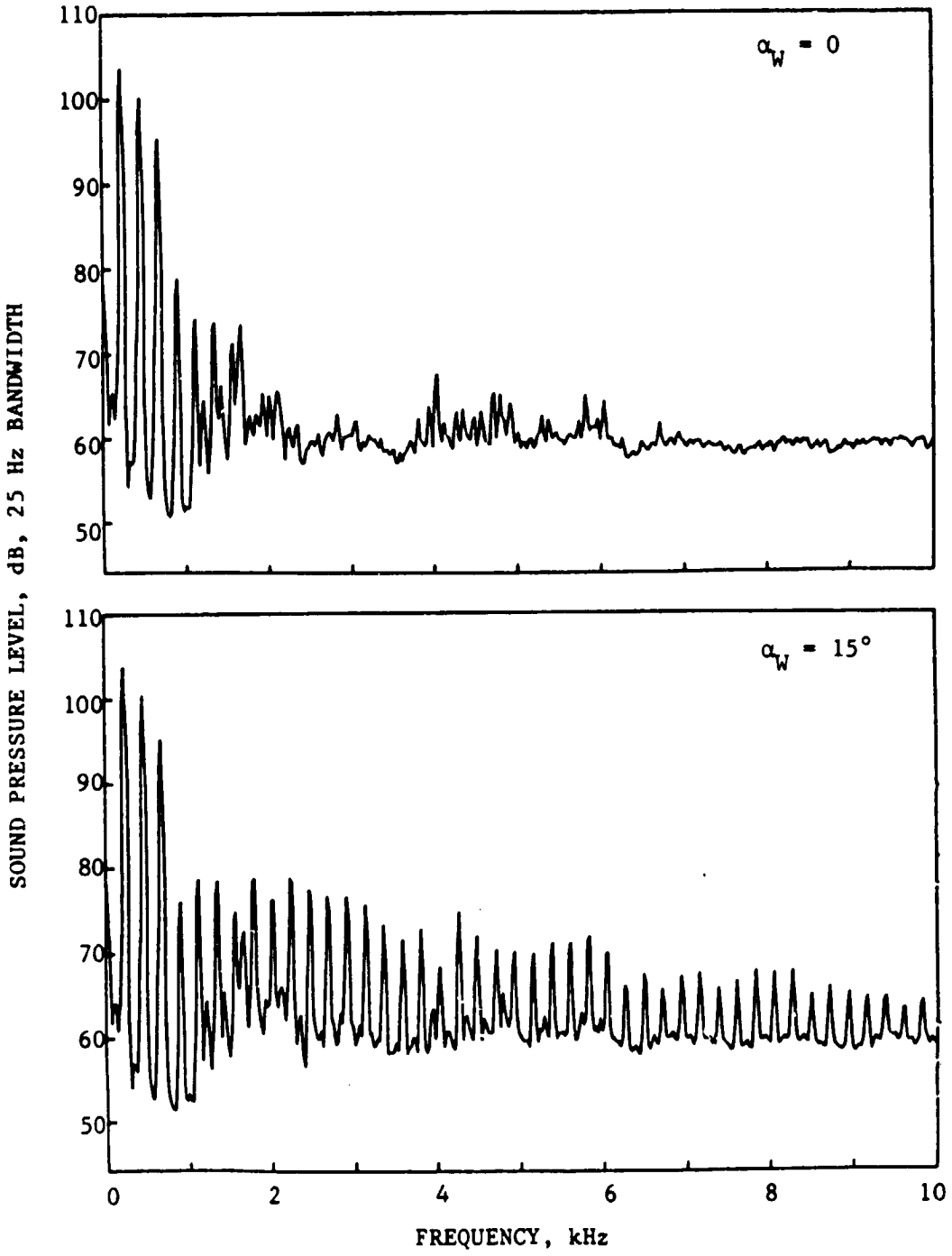

FIG. 29. EFFECT OF BLADE-VORTEX INTERACTION ON ROTOR ACOUSTIC SPECTRA FOR TEST CONDITION 3 (r_I/R = 0.90, M_T = 0.63, U_∞ = 7.3 m/s), θ = 50°.

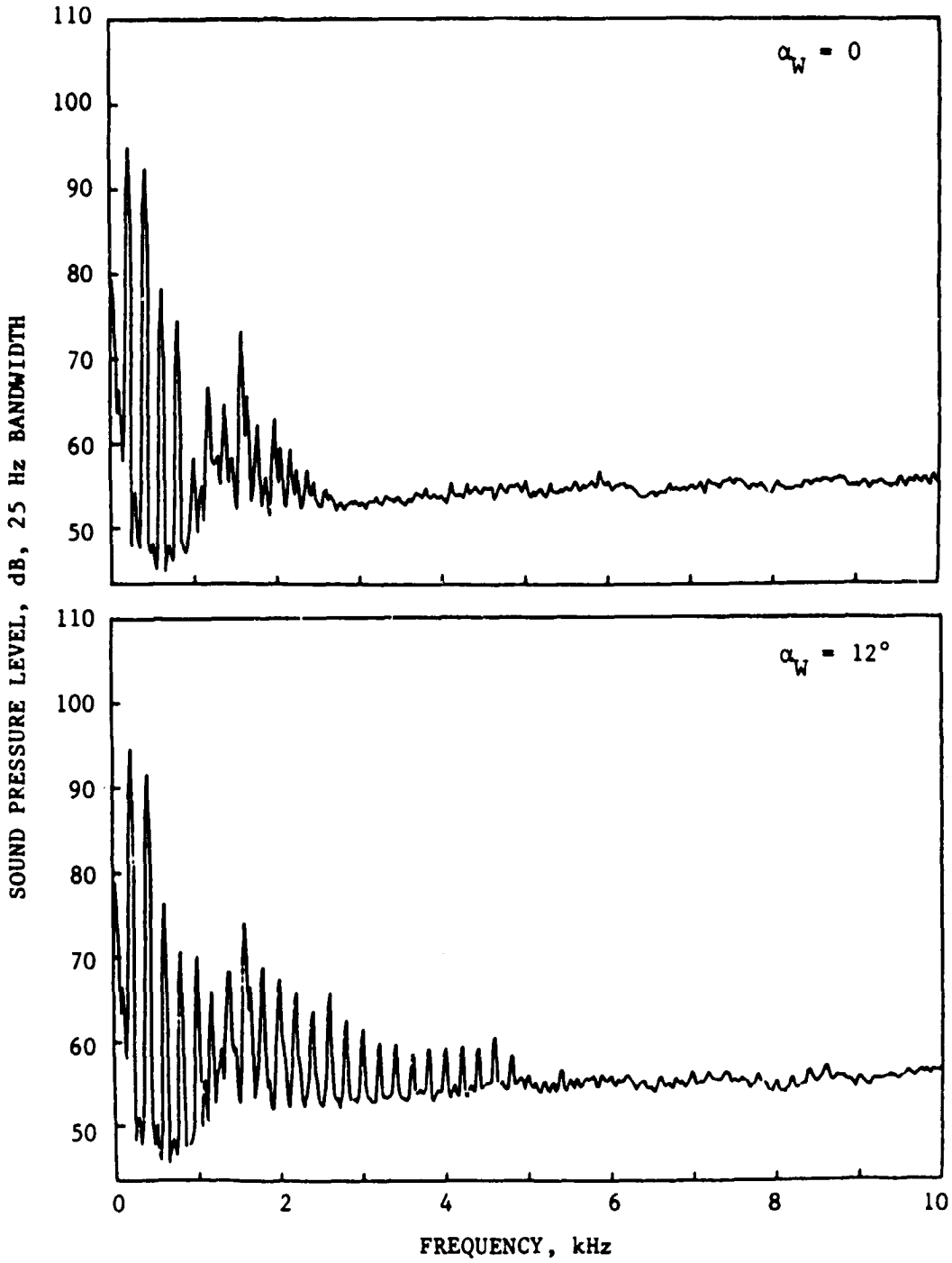

FIG. 30. EFFECT OF BLADE-VORTEX INTERACTION ON ROTOR ACOUSTIC SPECTRA FOR TEST CONDITION 4 (r_I/R = 0.975, M_T = 0.55, U_∞ = 9.1 m/s), θ = 50°.

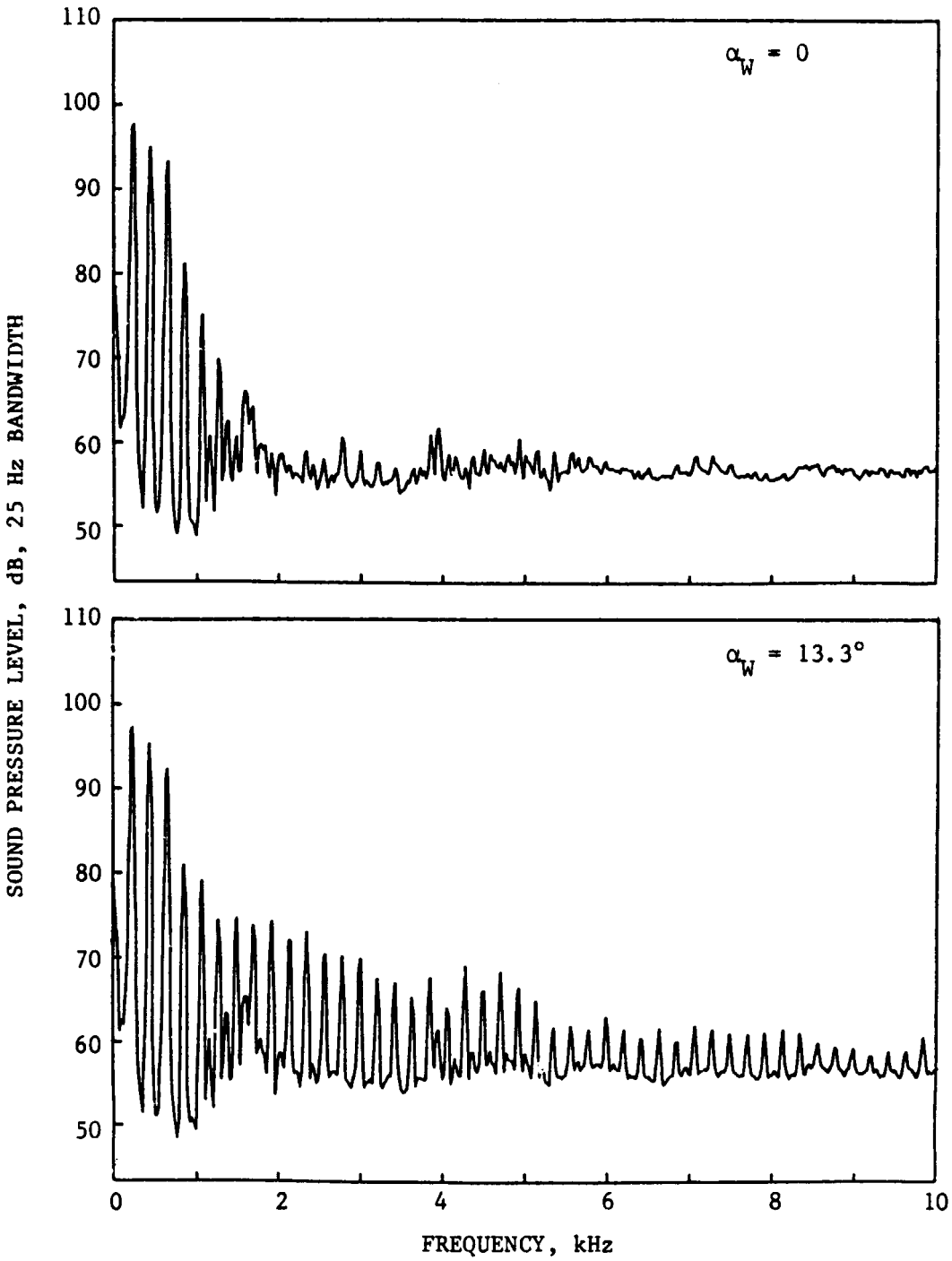

FIG. 31. EFFECT OF BLADE-VORTEX INTERACTION ON ROTOR ACOUSTIC SPECTRA FOR TEST CONDITION 5 (r_I/R = 0.975, M_T = 0.59, U_∞ = 8.2 m/s), θ = 50°.

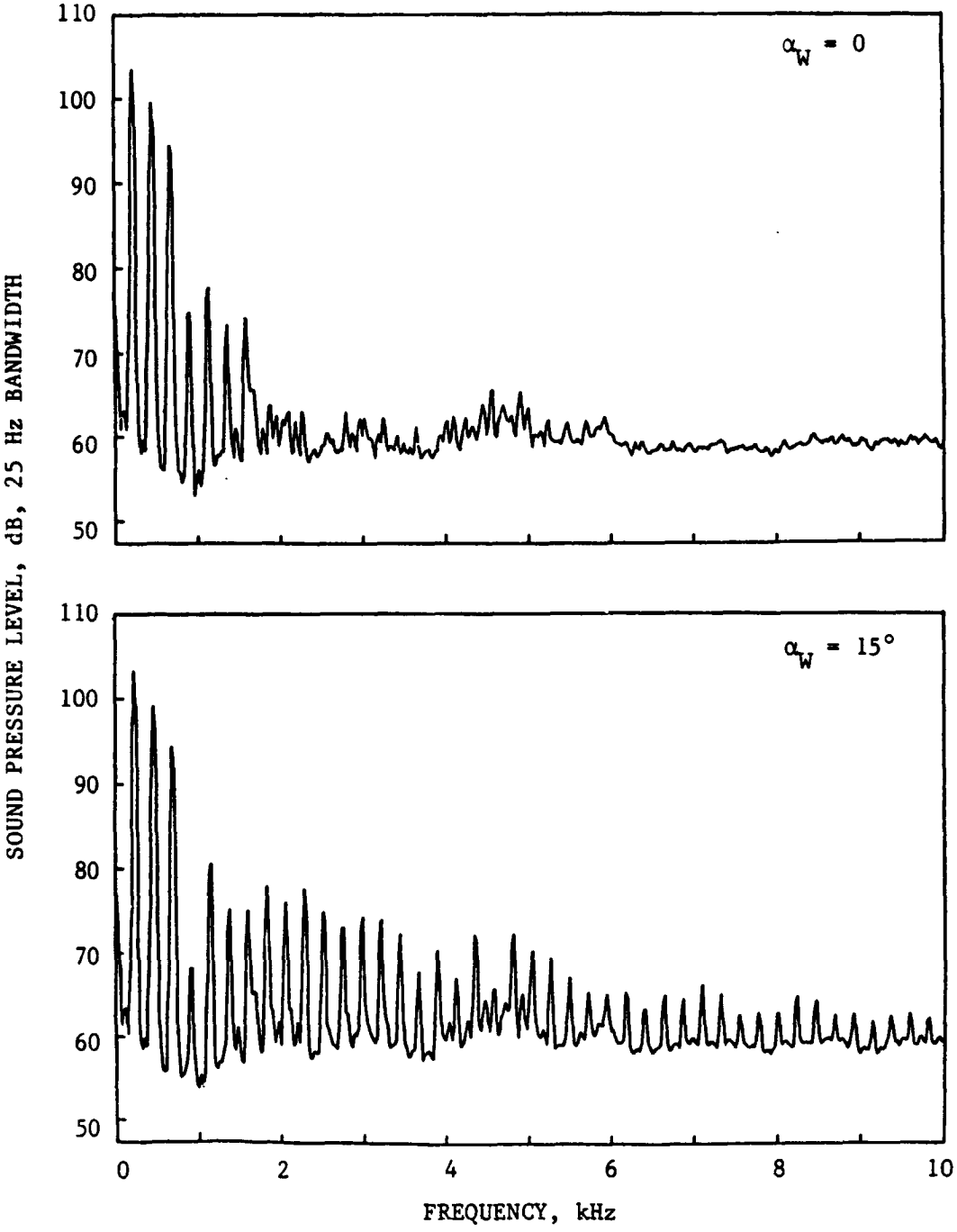

FIG. 32. EFFECT OF BLADE-VORTEX INTERACTION ON ROTOR ACOUSTIC SPECTRA FOR TEST CONDITION 6 (r_I/R = 0.975, M_T = 0.63, U_∞ = 7.3 m/s), θ = 50°.

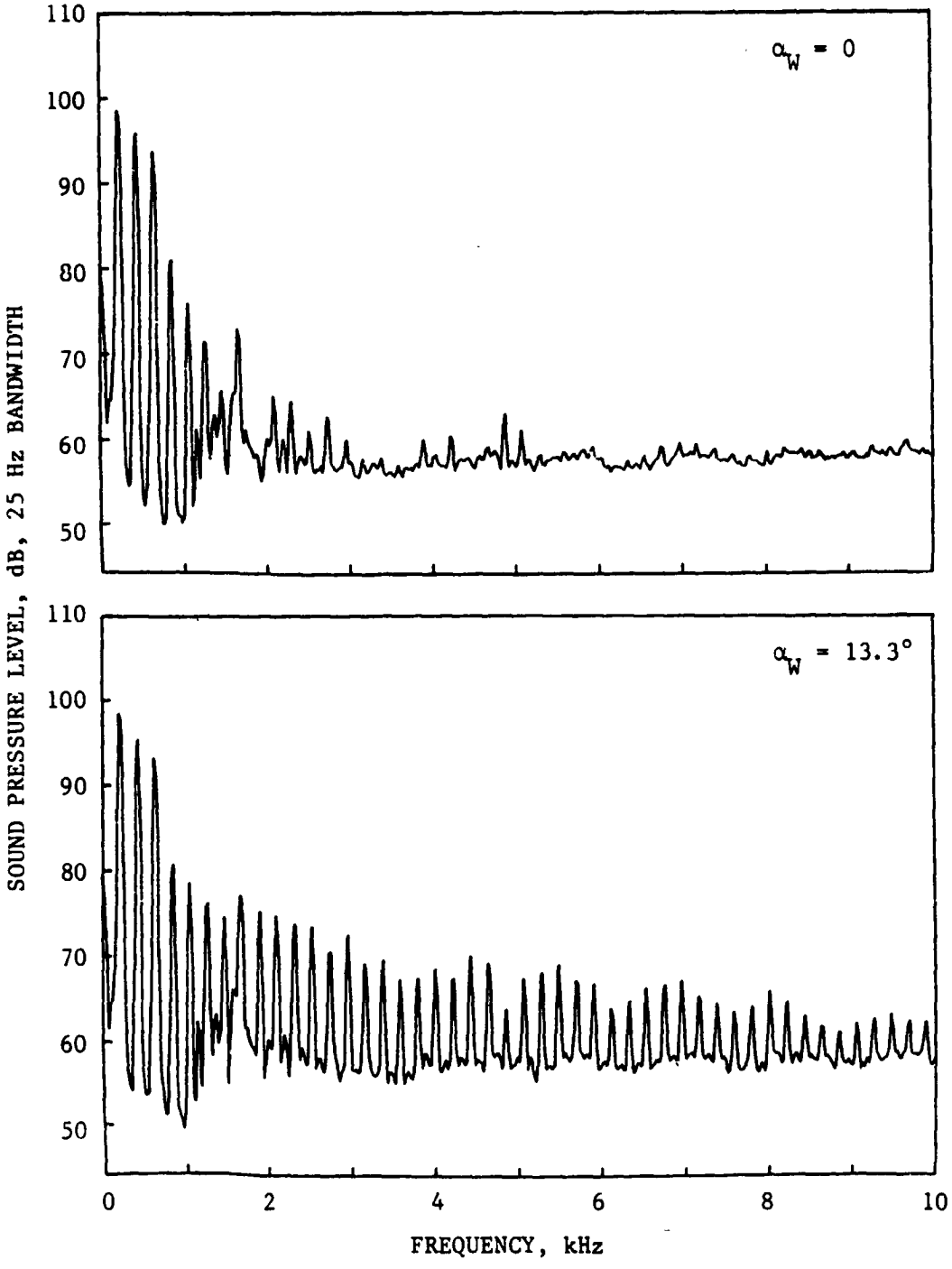

FIG. 33. EFFECT OF BLADE-VORTEX INTERACTION ON ROTOR ACOUSTIC SPECTRA FOR TEST CONDITION 2 (r_I/R = 0.90, M_T = 0.59, U_∞ = 8.2 m/s), θ = 50°.

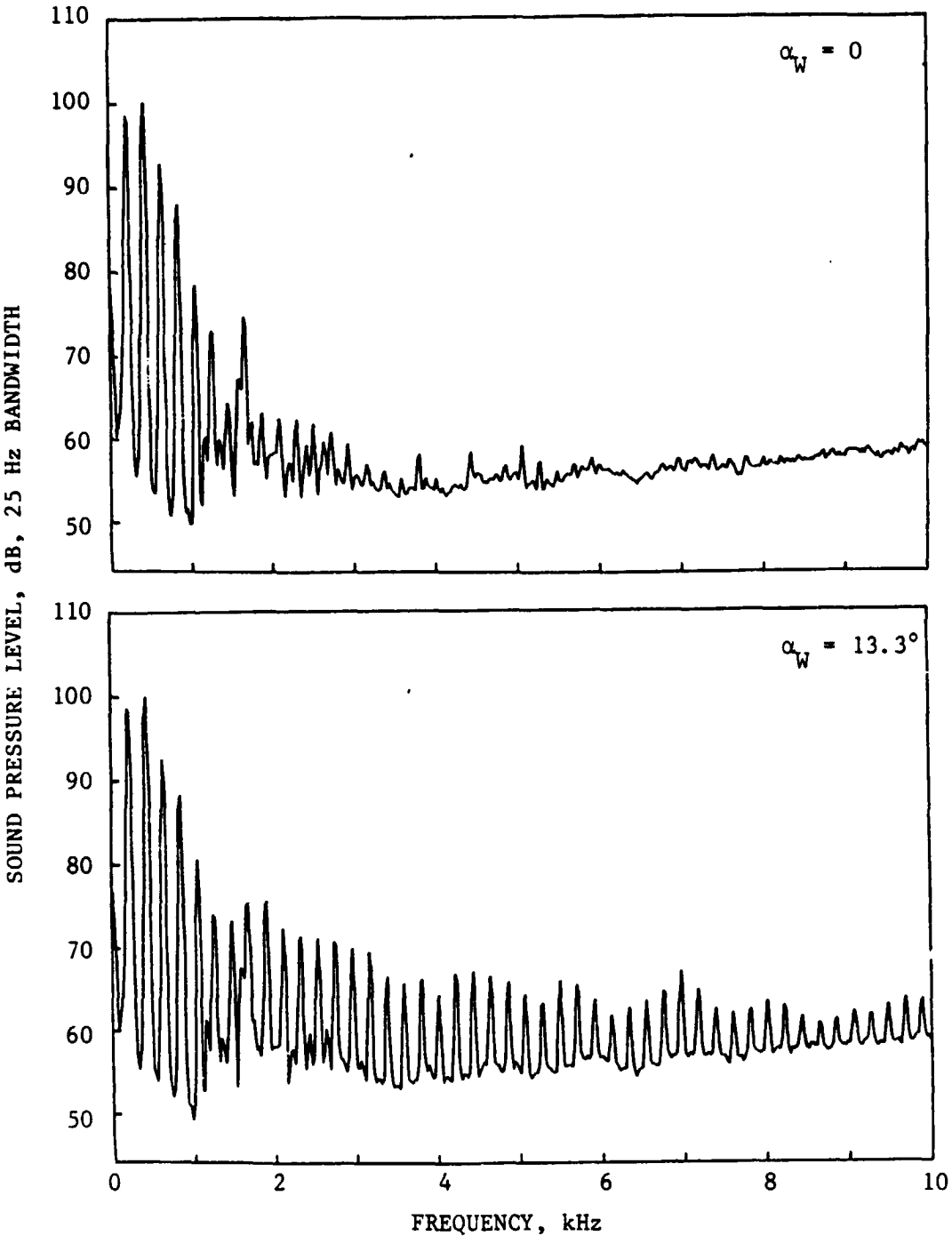

FIG. 34. EFFECT OF BLADE-VORTEX INTERACTION ON ROTOR ACOUSTIC SPECTRA FOR TEST CONDITION 2 (r_I/R = 0.90, M_T = 0.59, U_∞ = 8.2 m/s), θ = 60°.

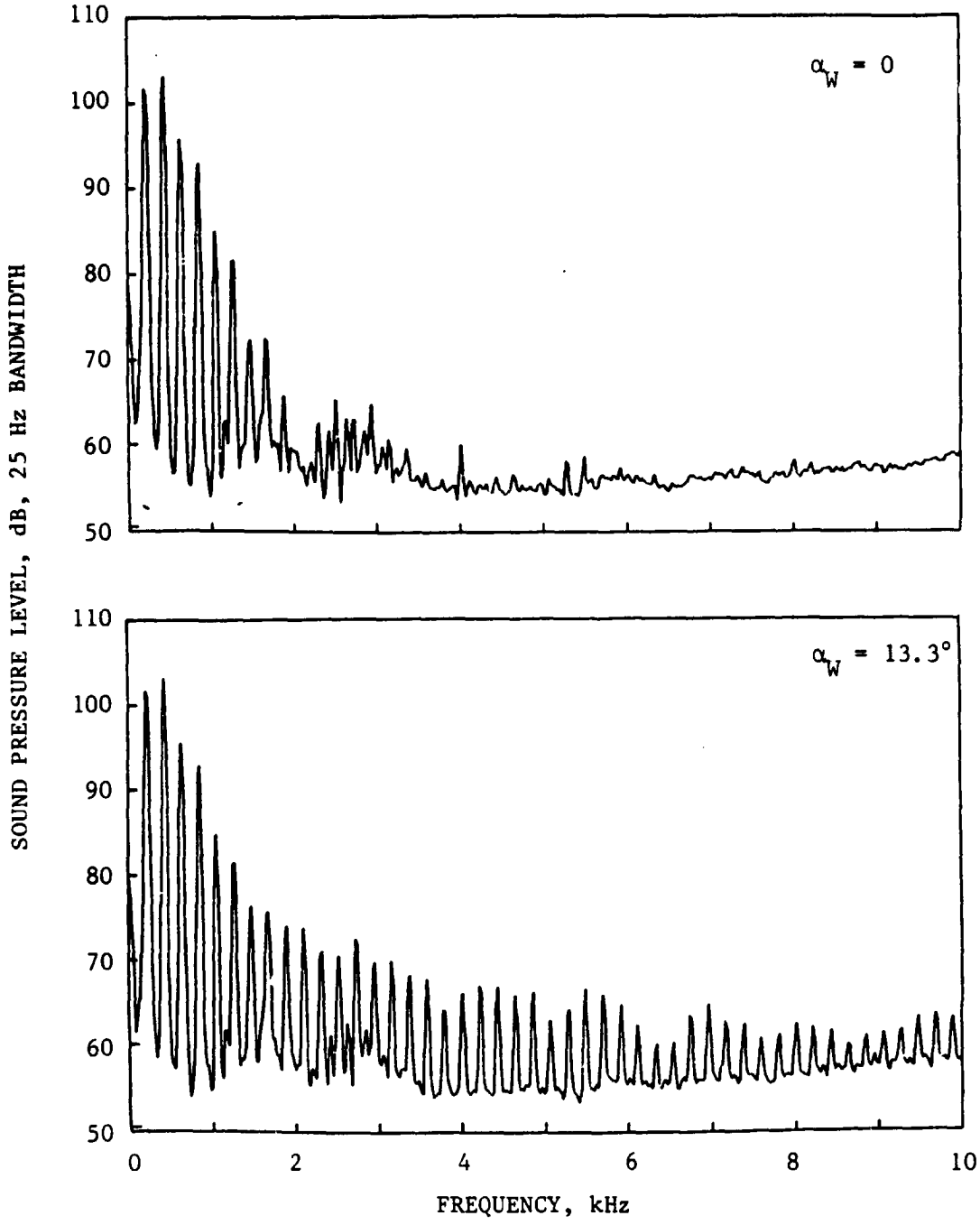

FIG. 35. EFFECT OF BLADE-VORTEX INTERACTION ON ROTOR ACOUSTIC SPECTRA FOR TEST CONDITION 2 (r_I/R = 0.90, M_T = 0.59, U_∞ = 8.2 m/s), θ = 70°.

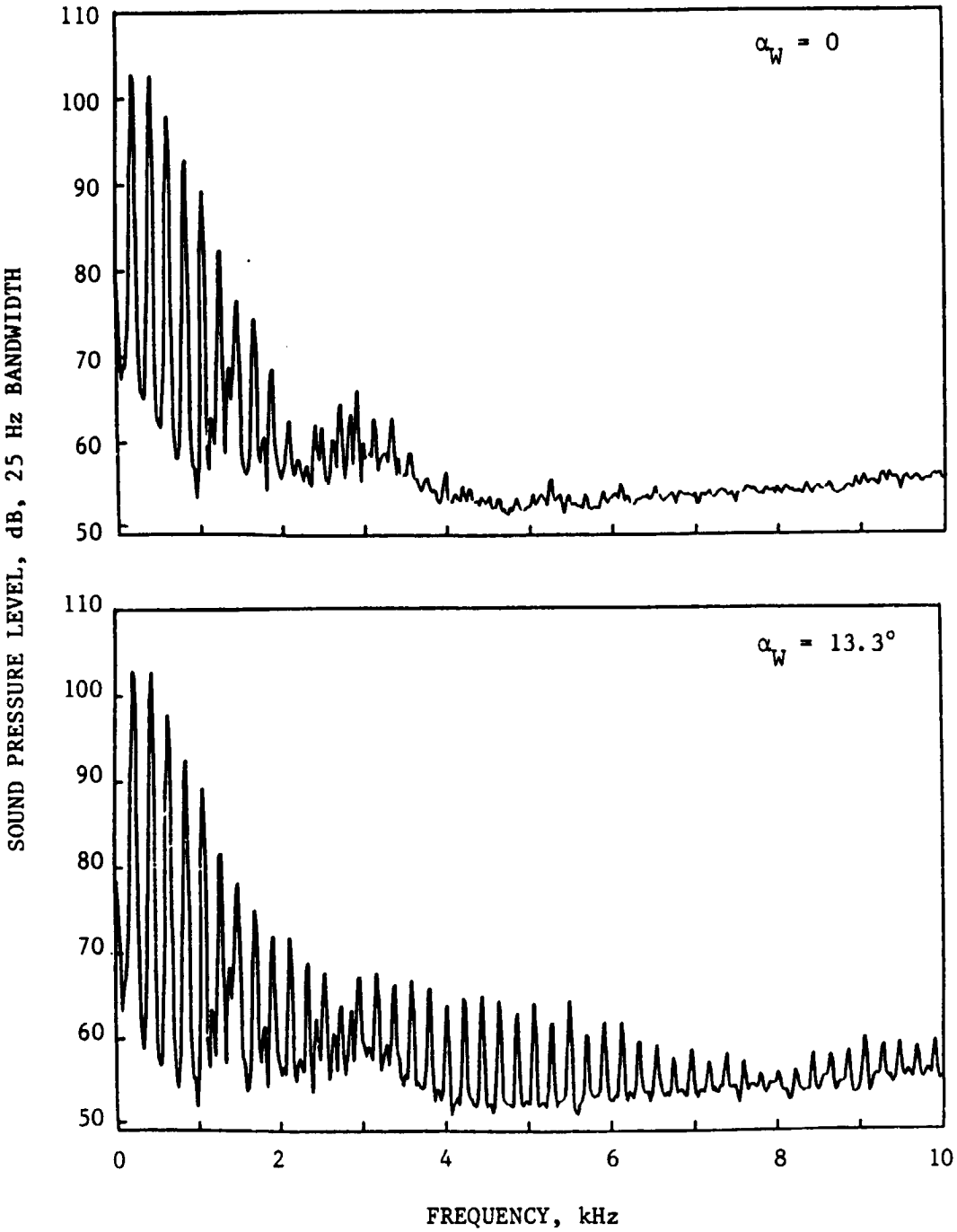

FIG. 36. EFFECT OF BLADE-VORTEX INTERACTION ON ROTOR ACOUSTIC SPECTRA FOR TEST CONDITION 2 (r_I/R = 0.90, M_T = 0.59, U_∞ = 8.2 m/s), θ = 80°.

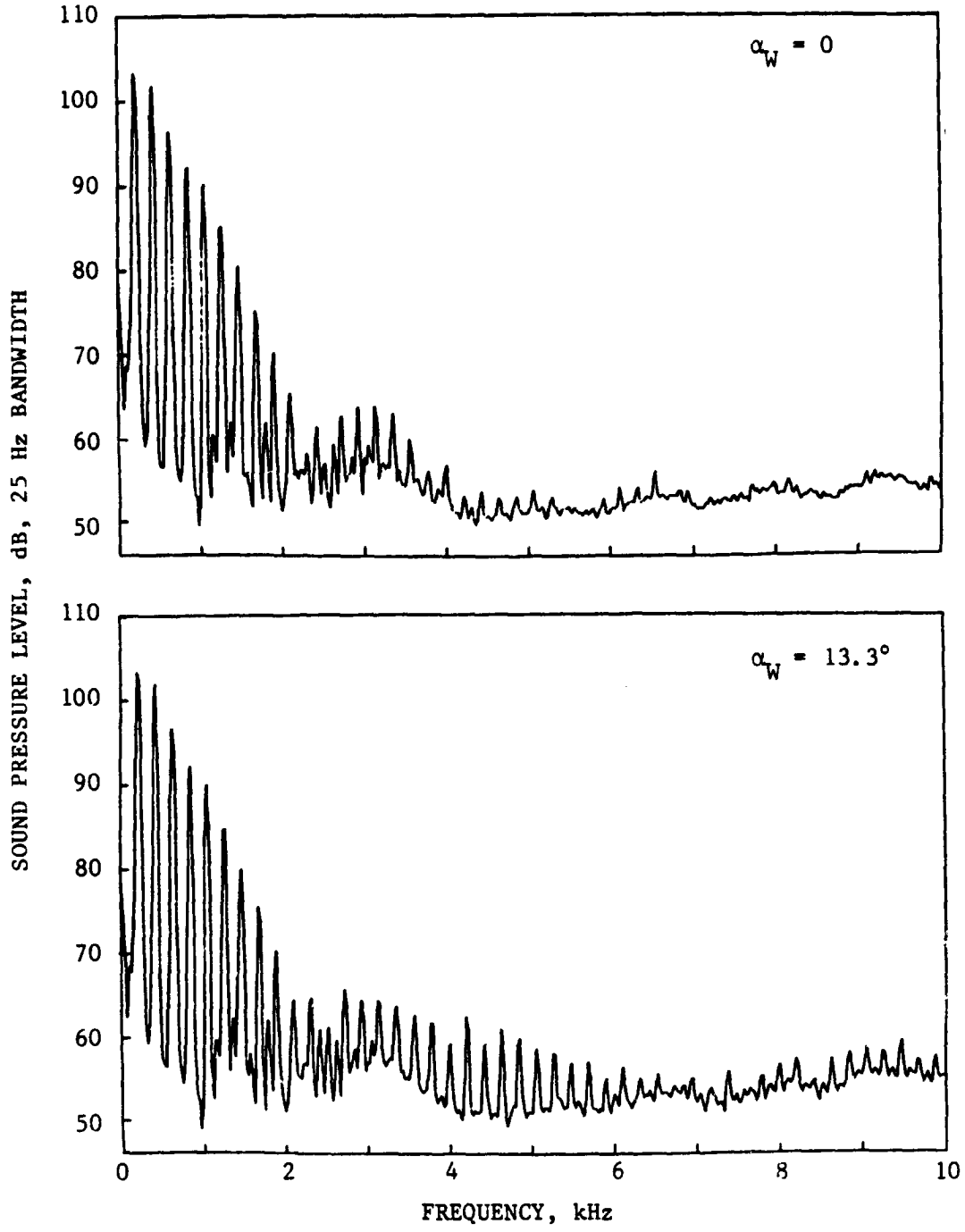

FIG. 37. EFFECT OF BLADE-VORTEX INTERACTION ON ROTOR ACOUSTIC SPECTRA FOR TEST CONDITION 2 (r_I/R = 0.90, M_T = 0.59, U_∞ = 8.2 m/s), θ = 90°.

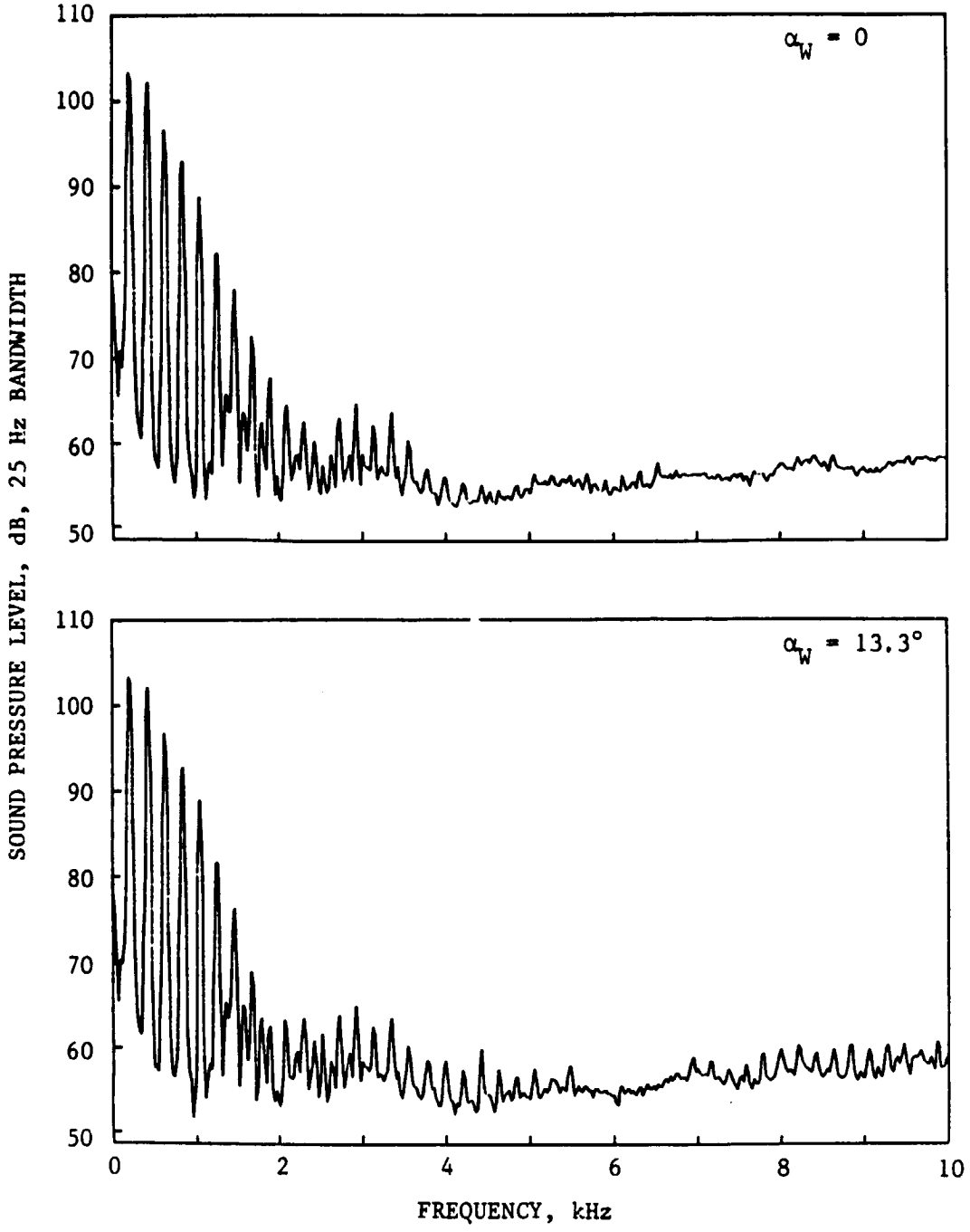

FIG. 38. EFFECT OF BLADE-VORTEX INTERACTION ON ROTOR ACOUSTIC SPECTRA FOR TEST CONDITION 2 (r_I/R = 0.90, M_T = 0.59, U_∞ = 8.2 m/s), θ = 100°.

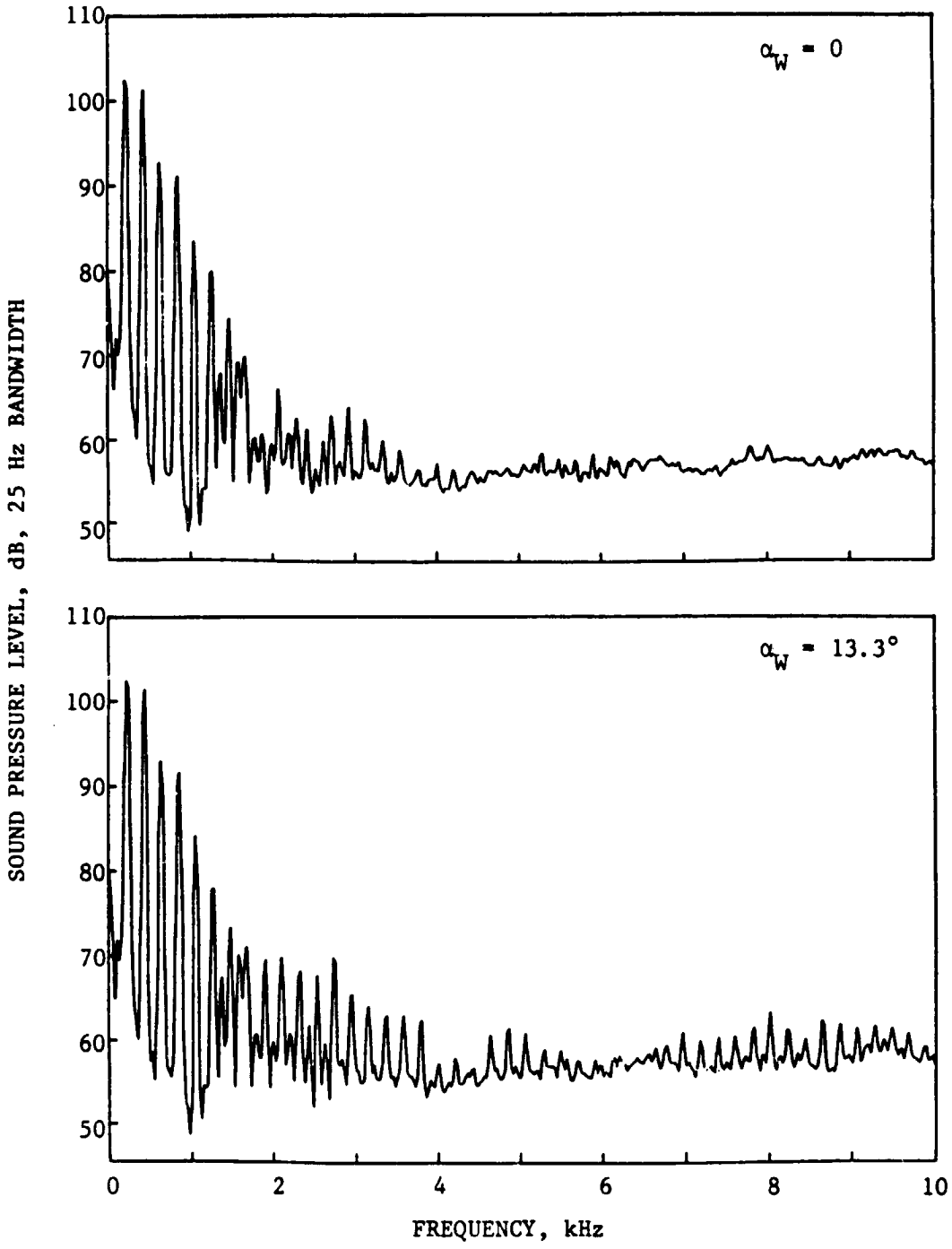

FIG. 39. EFFECT OF BLADE-VORTEX INTERACTION ON ROTOR ACOUSTIC SPECTRA FOR TEST CONDITION 2 (r_I/R = 0.90, M_T = 0.59, U_∞ = 8.2 m/s), θ = 110°.

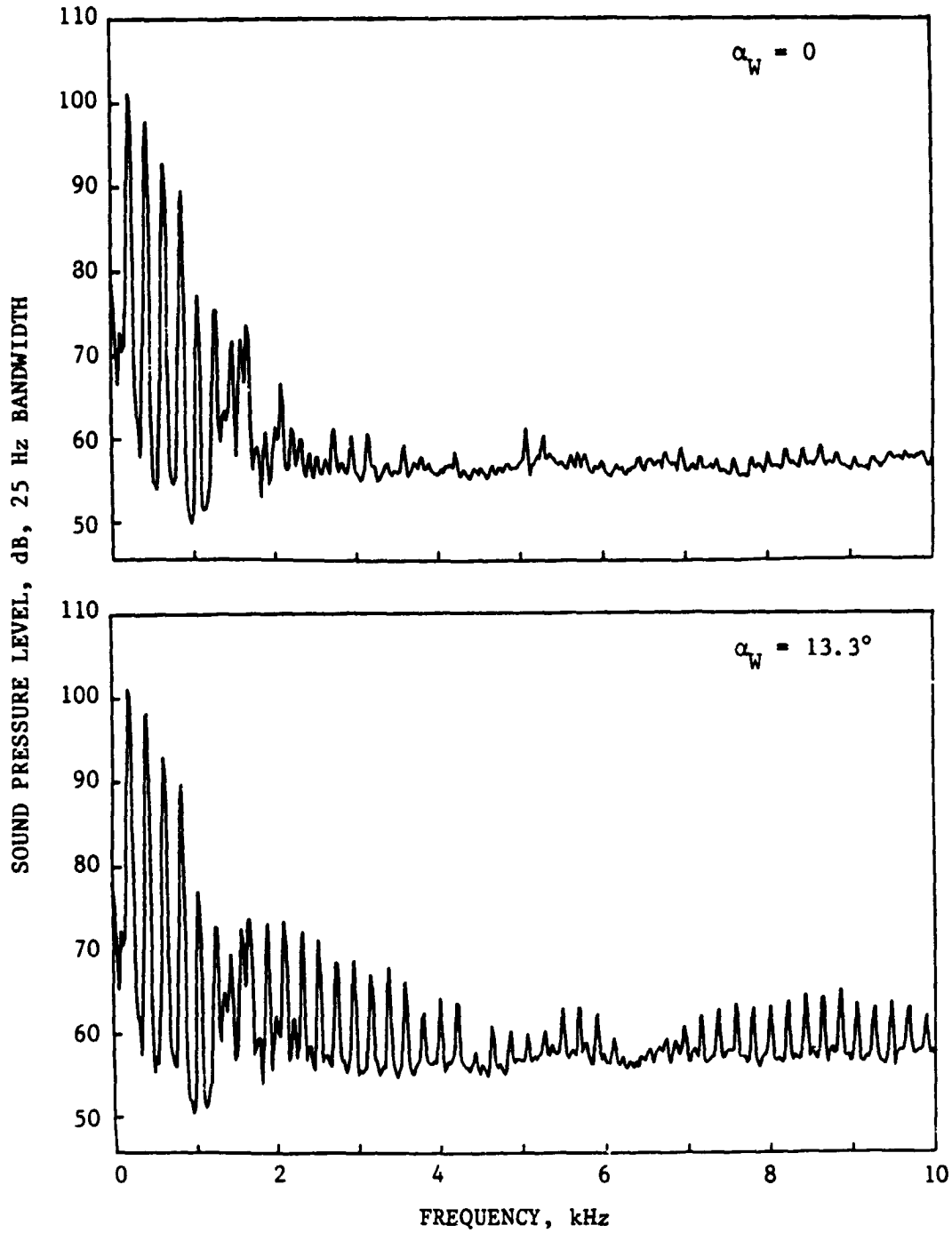

FIG. 40. EFFECT OF BLADE-VORTEX INTERACTION ON ROTOR ACOUSTIC SPECTRA FOR TEST CONDITION 2 (r_I/R = 0.90, M_T = 0.59, U_∞ = 8.2 m/s), θ = 120°.

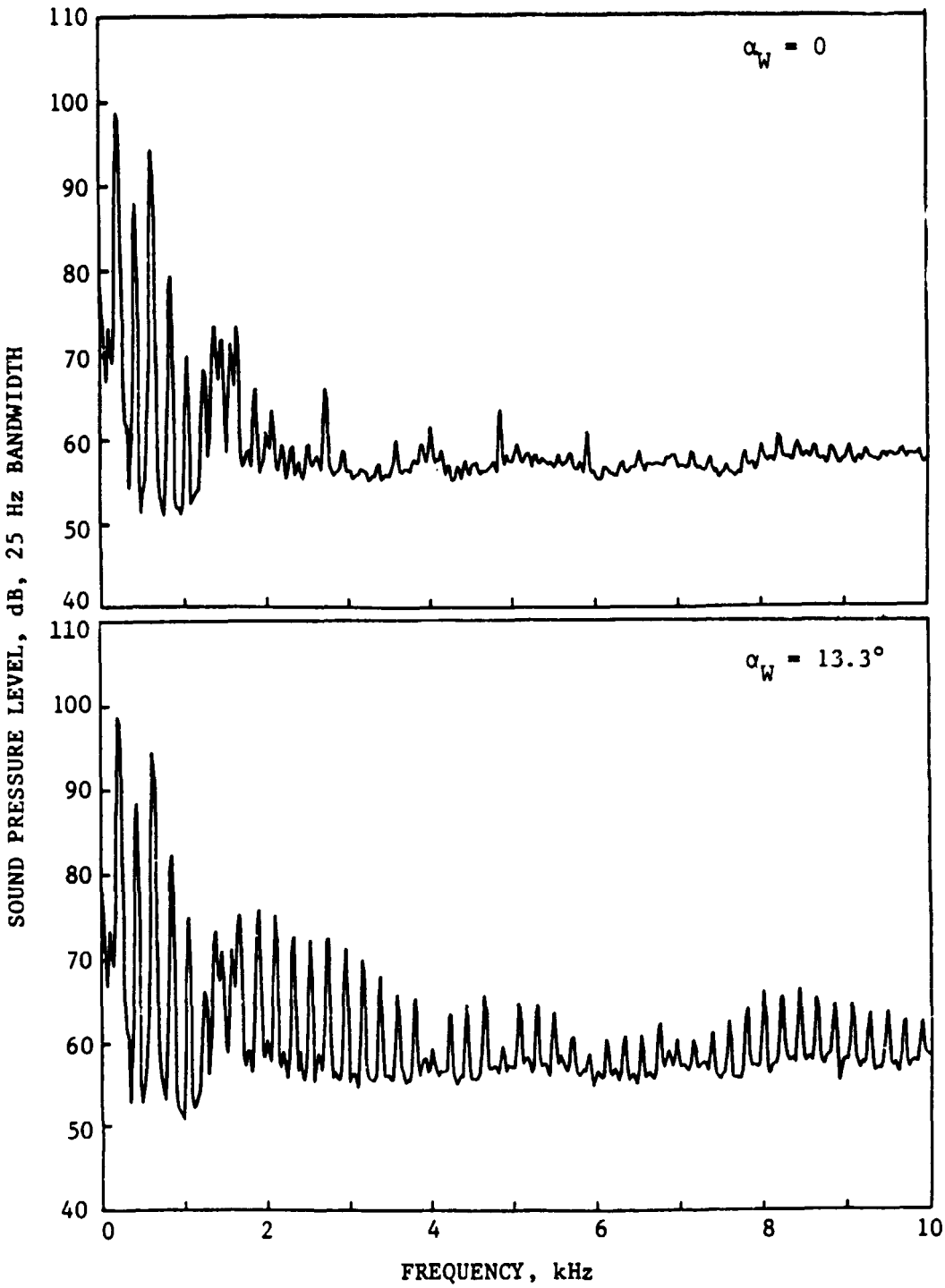

FIG. 41. EFFECT OF BLADE-VORTEX INTERACTION ON ROTOR ACOUSTIC SPECTRA FOR TEST CONDITION 2 (r_I/R = 0.90, M_T = 0.59, U_∞ = 8.2 m/s), θ = 130°.

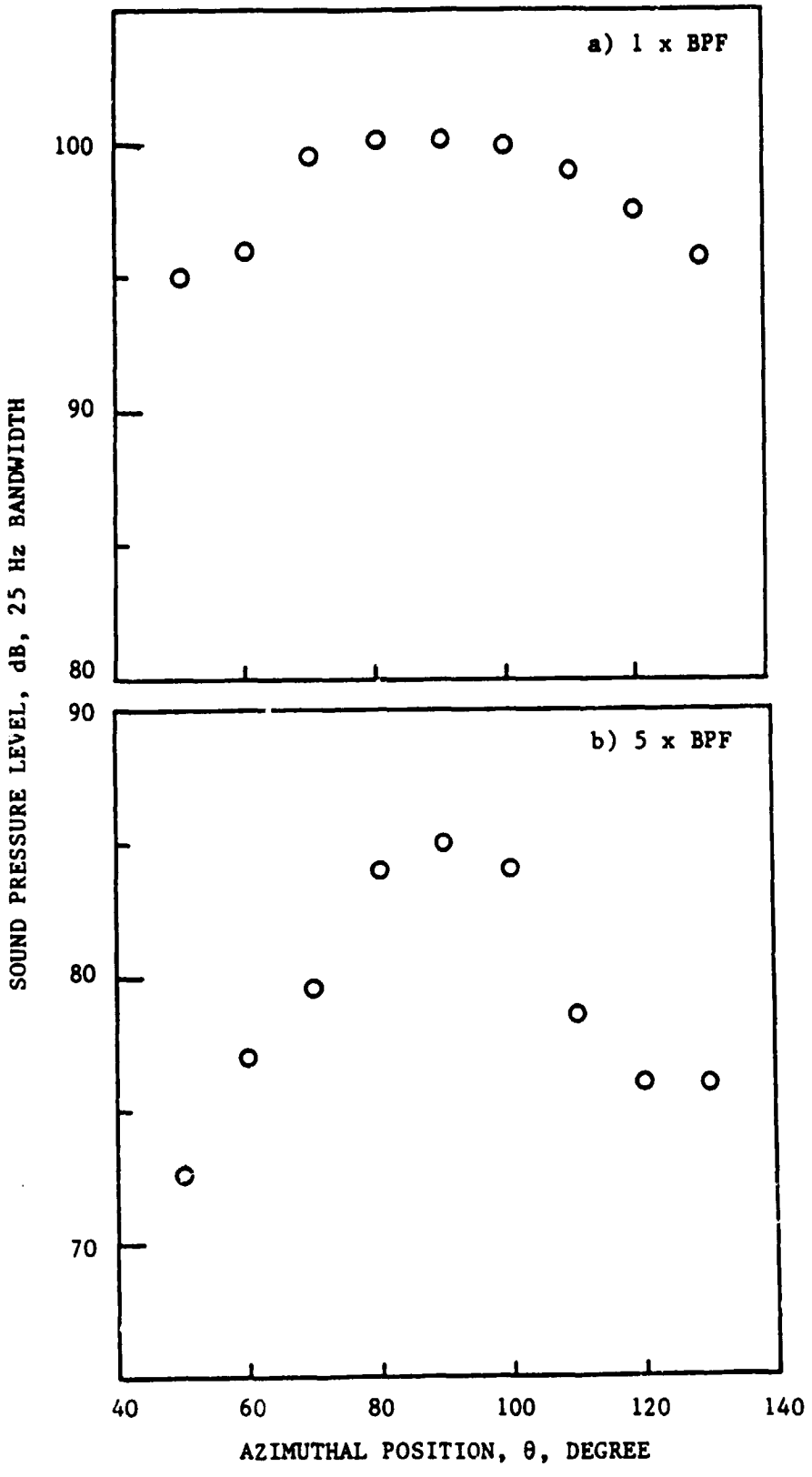

FIG. 42. DIRECTIVITY PATTERN OF BLADE-VORTEX INTERACTION HARMONIC NOISE FOR TEST CONDITION 1 (r_I/R = 0.90, M_T = 0.55, U_∞ = 9.1 m/s). ⚲ DENOTES THAT ACTUAL LEVEL IS SOMEWHAT LOWER THAN INDICATED LEVEL.

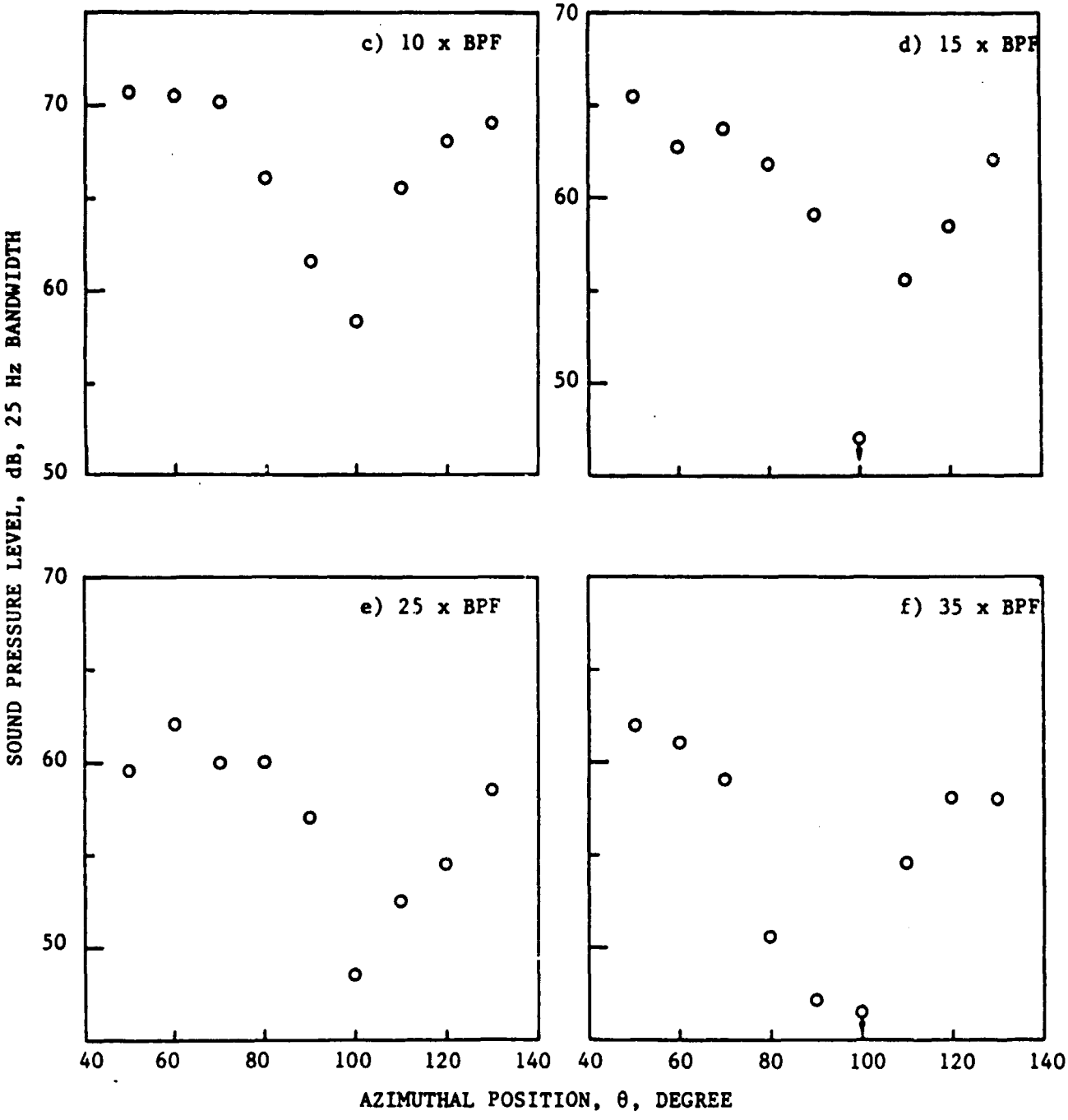
c) 10 x BPF
d) 15 x BPF
e) 25 x BPF
f) 35 x BPF
SOUND PRESSURE LEVEL, dB, 25 Hz BANDWIDTH
AZIMUTHAL POSITION, θ, DEGREE
70
60
50
40
60
80
100
120
140

FIG. 42. (CONT'D.).

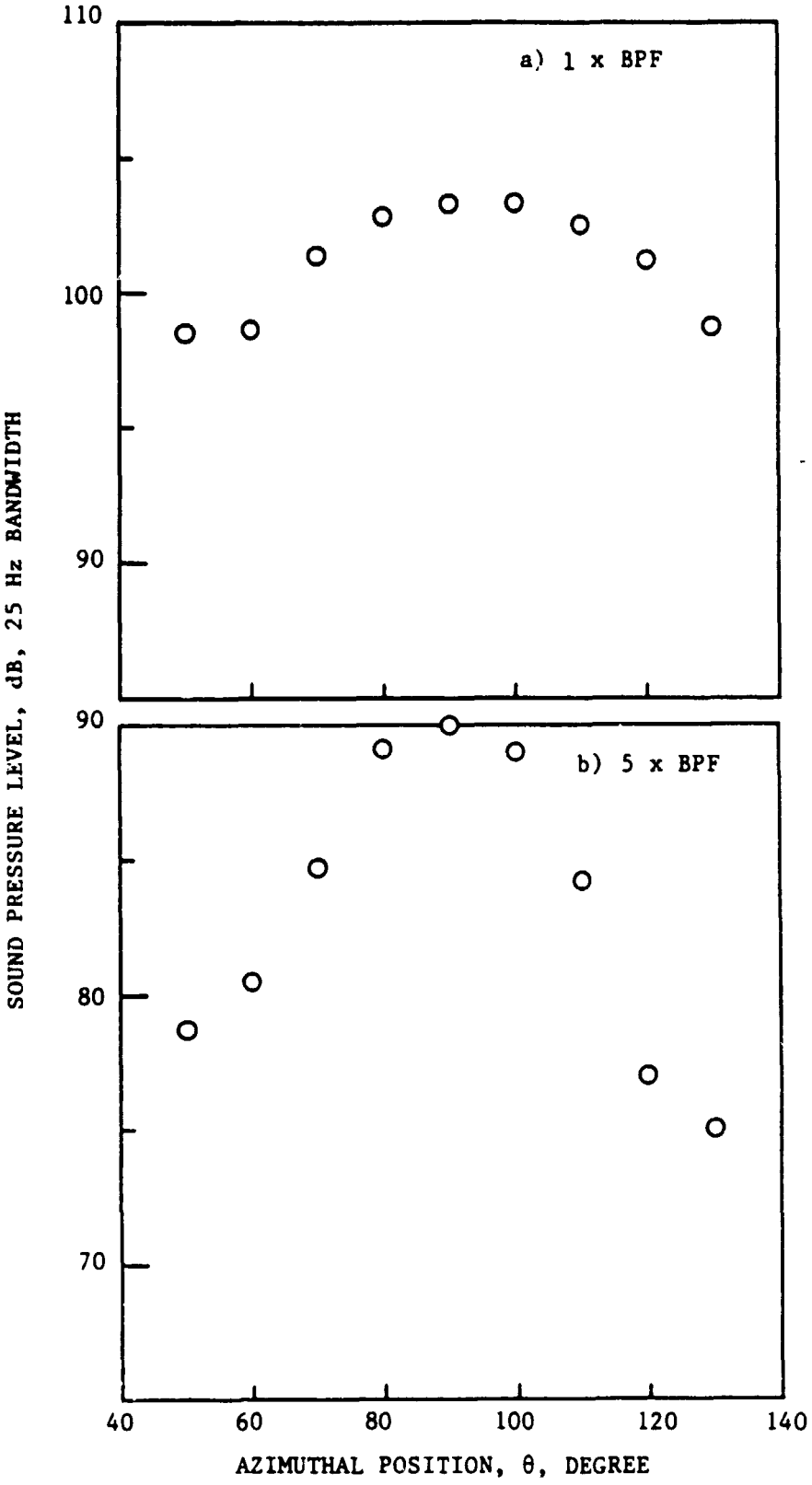

FIG. 43. DIRECTIVITY PATTERN OF BLADE-VORTEX INTERACTION HARMONIC NOISE FOR TEST CONDITION 2 (r_I/R = 0.90, M_T = 0.59, U_∞ = 8.2 m/s). ♀ DENOTES THAT ACTUAL LEVEL IS SOMEWHAT LOWER THAN INDICATED LEVEL.

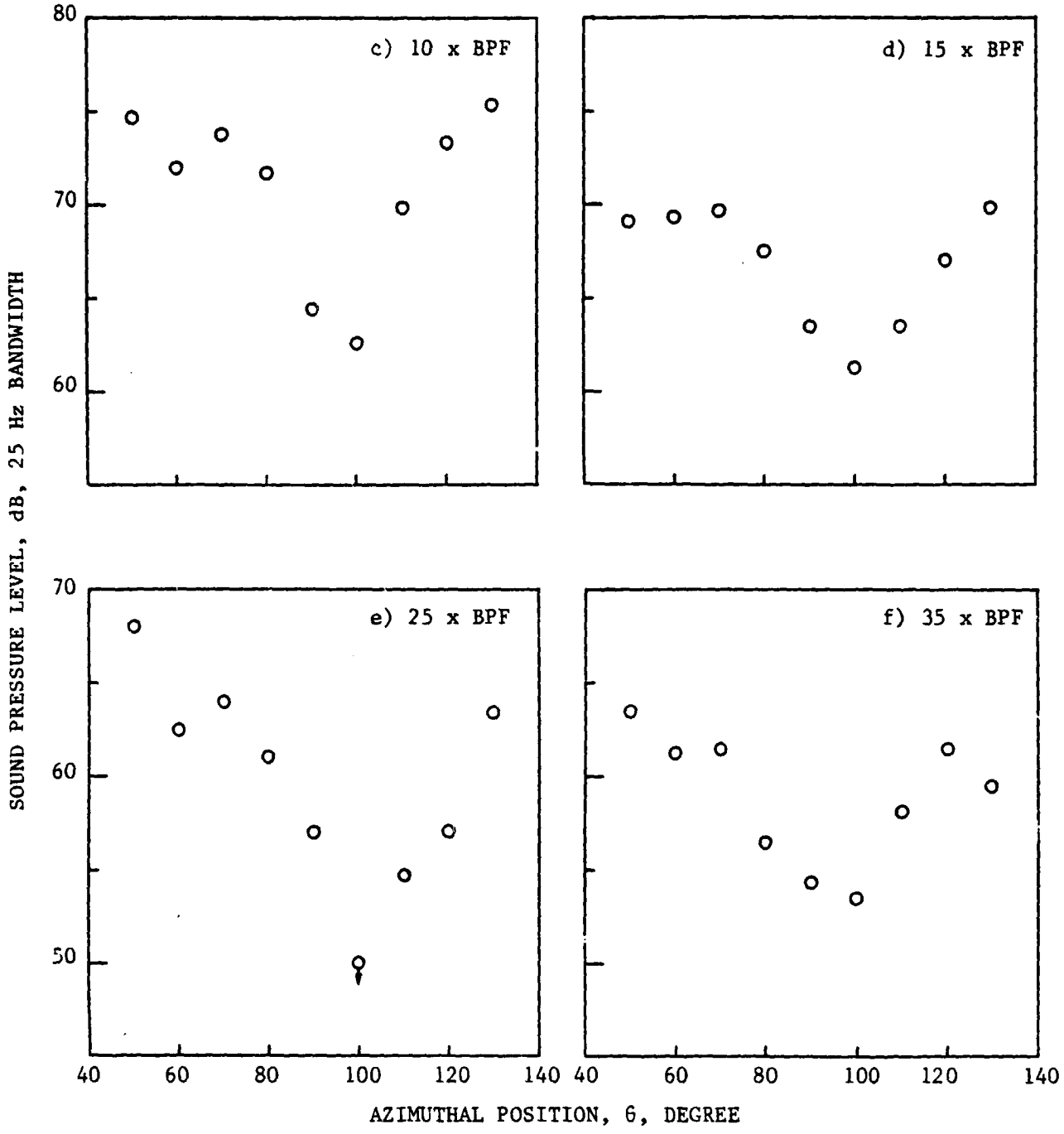
c) 10 x BPF
d) 15 x BPF
e) 25 x BPF
f) 35 x BPF
SOUND PRESSURE LEVEL, dB, 25 Hz BANDWIDTH
AZIMUTHAL POSITION, θ, DEGREE
80
70
60
50
40
60
80
100
120
140

FIG. 43. (CONT'D.).

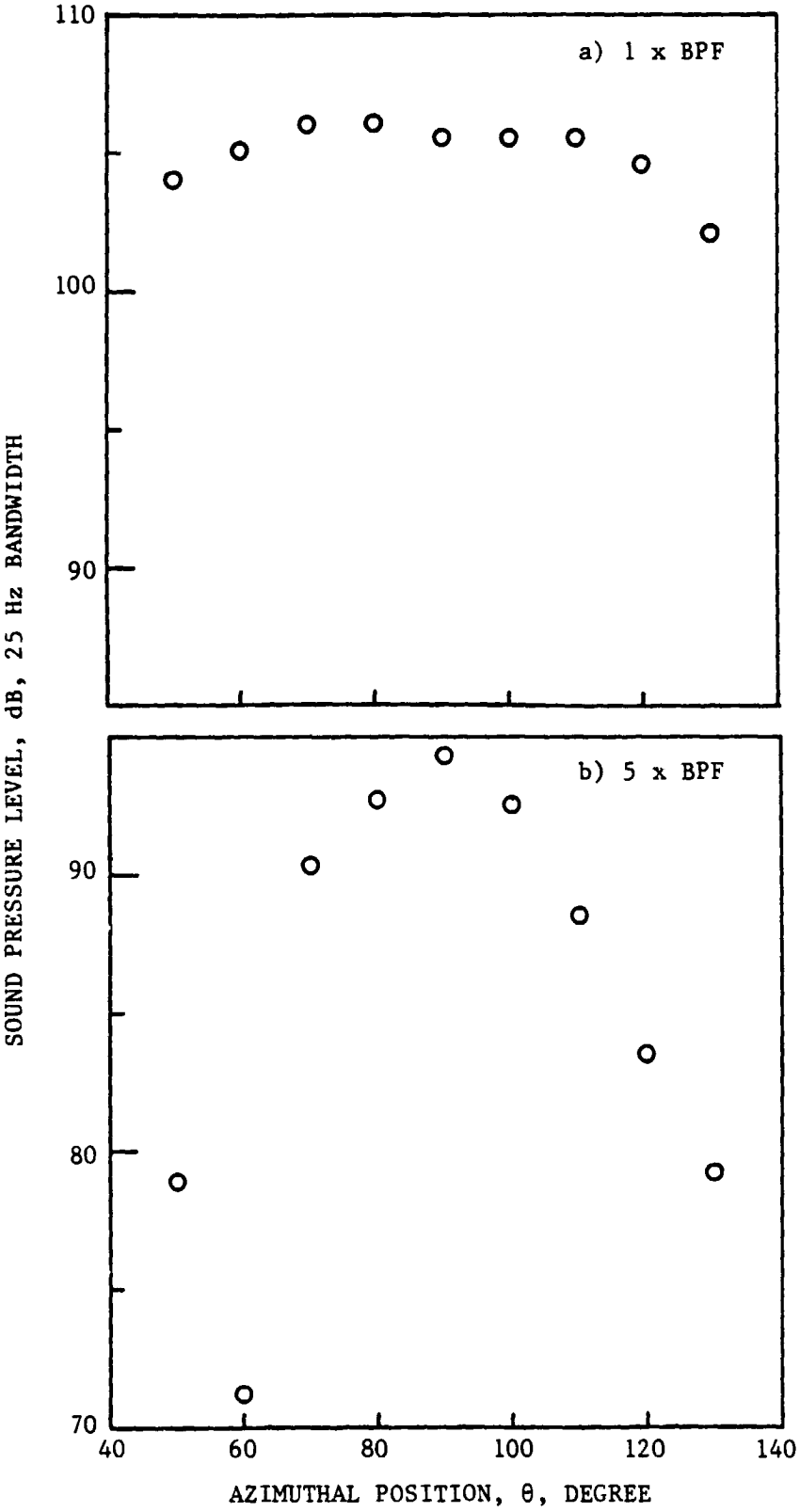

FIG. 44. DIRECTIVITY PATTERN OF BLADE-VORTEX INTERACTION HARMONIC NOISE FOR TEST CONDITION 3 (r_I/R = 0.90, M_T = 0.63, U_∞ = 7.3 m/s). ♀ DENOTES THAT ACTUAL LEVEL IS SOMEWHAT LOWER THAN INDICATED LEVEL.

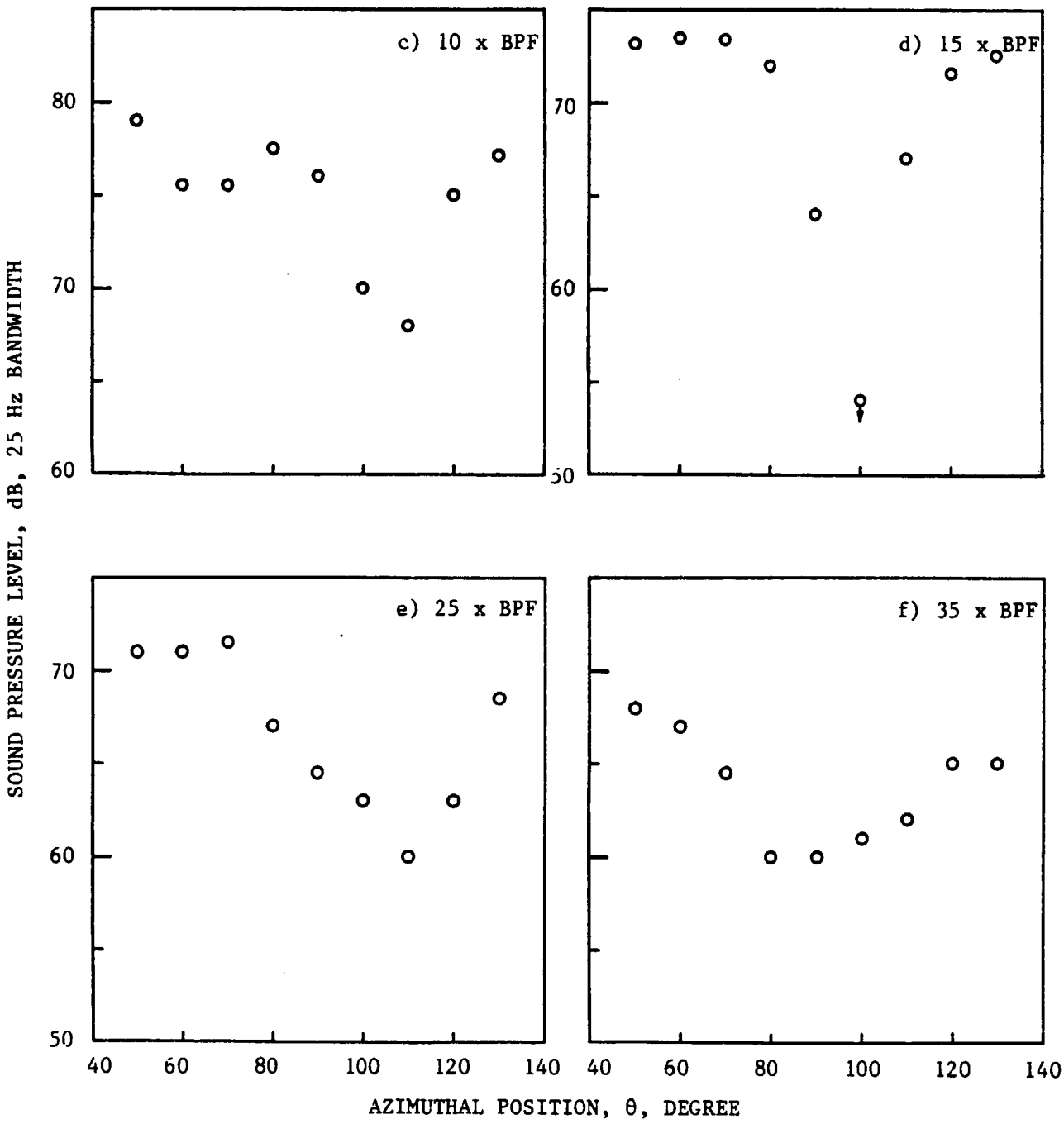
c) 10 x BPF
d) 15 x BPF
e) 25 x BPF
f) 35 x BPF
SOUND PRESSURE LEVEL, dB, 25 Hz BANDWIDTH
AZIMUTHAL POSITION, θ, DEGREE
80
70
60
50
40
60
80
100
120
140

FIG. 44. (CONT'D.).

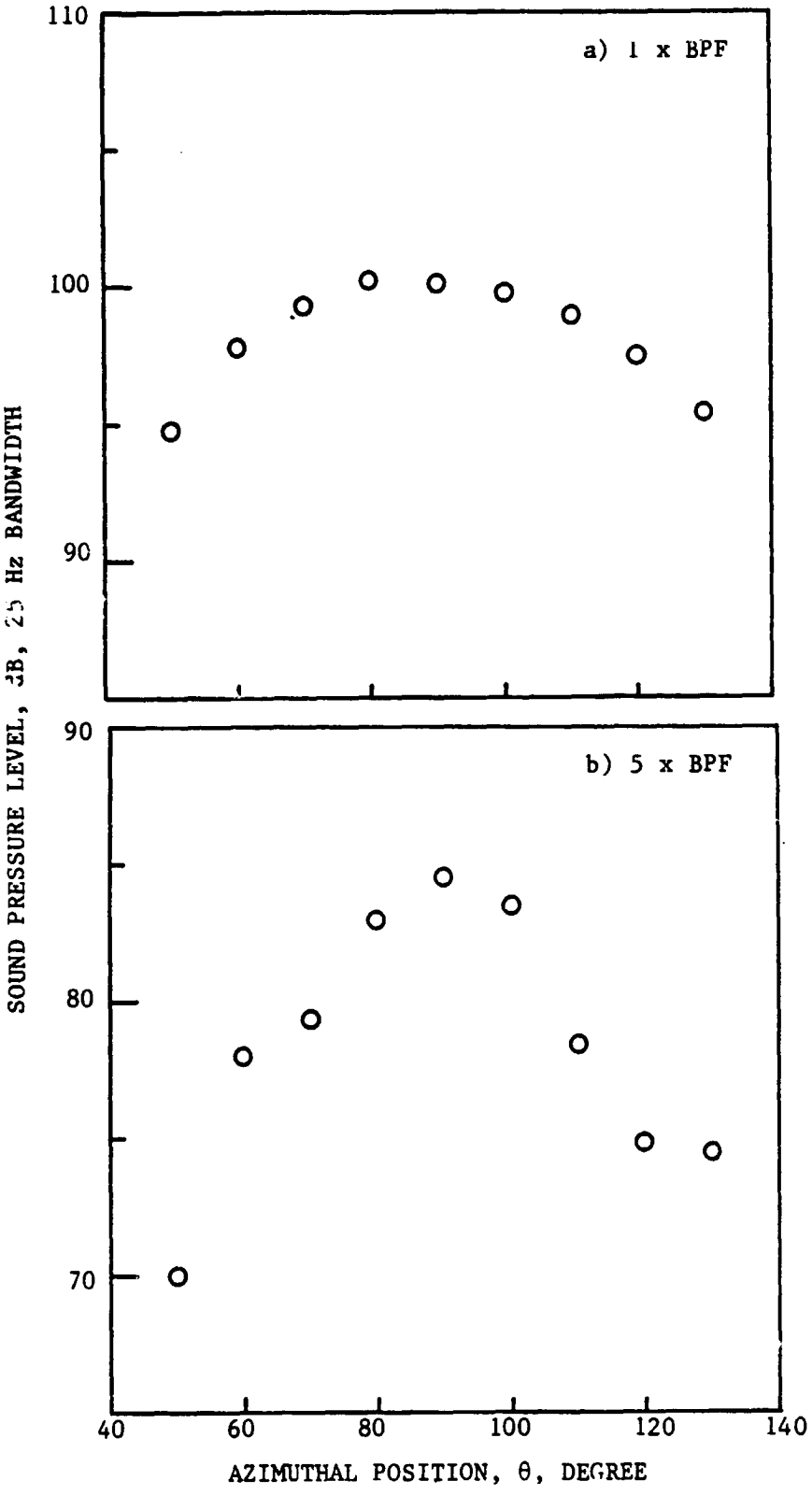

FIG. 45. DIRECTIVITY PATTERN OF BLADE-VORTEX INTERACTION HARMONIC NOISE FOR TESTS CONDITION 4 (r_I/R = 0.975, M_T = 0.55, U_∞ = 9.1 m/s). ⚲ DENOTES THAT ACTUAL LEVEL IS SOMEWHAT LOWER THAN INDICATED LEVEL.

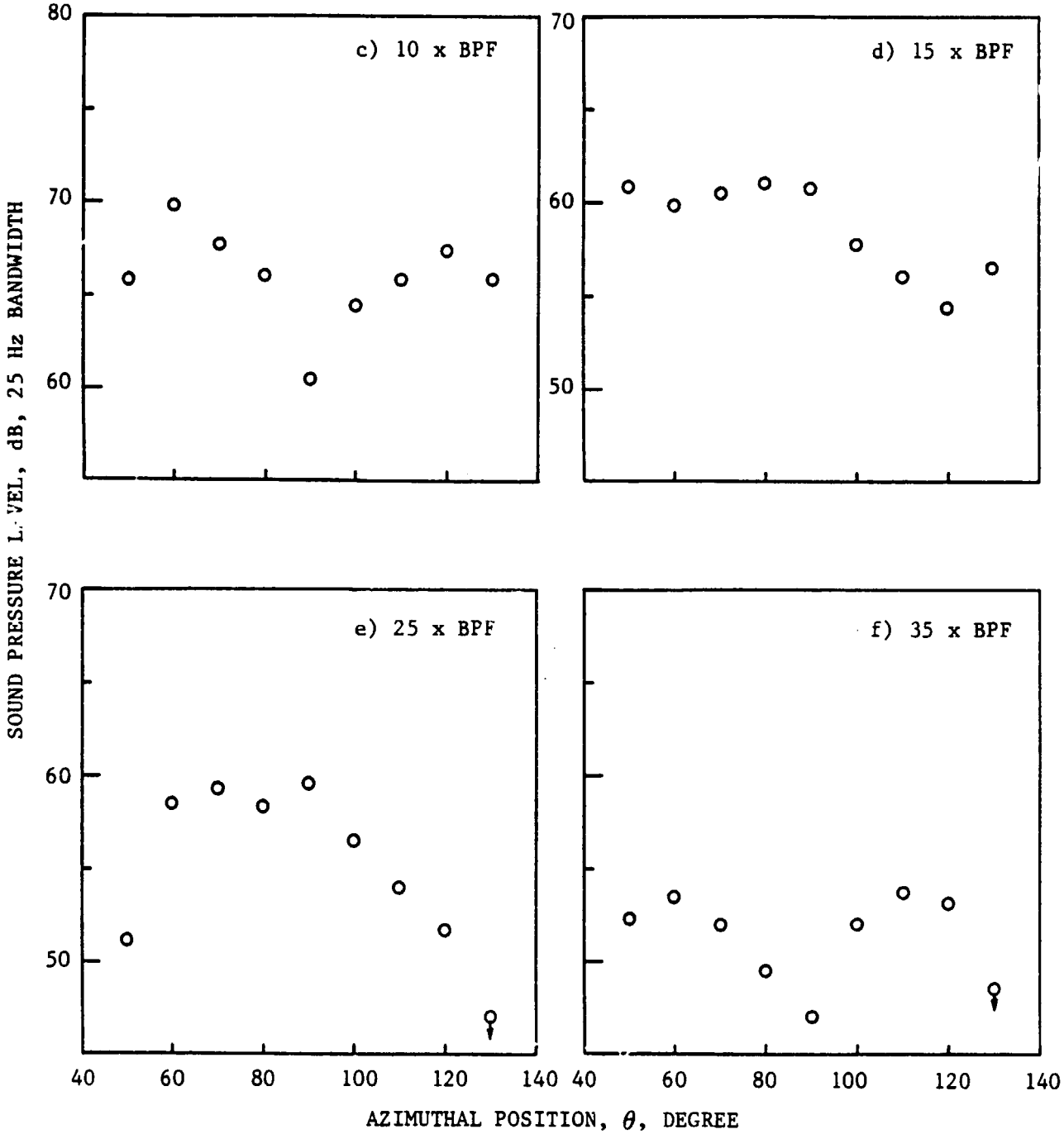
c) 10 x BPF
d) 15 x BPF
e) 25 x BPF
f) 35 x BPF
SOUND PRESSURE LEVEL, dB, 25 Hz BANDWIDTH
AZIMUTHAL POSITION, θ, DEGREE
80
70
60
50
40
60
80
100
120
140

FIG. 45. (CONT'D.).

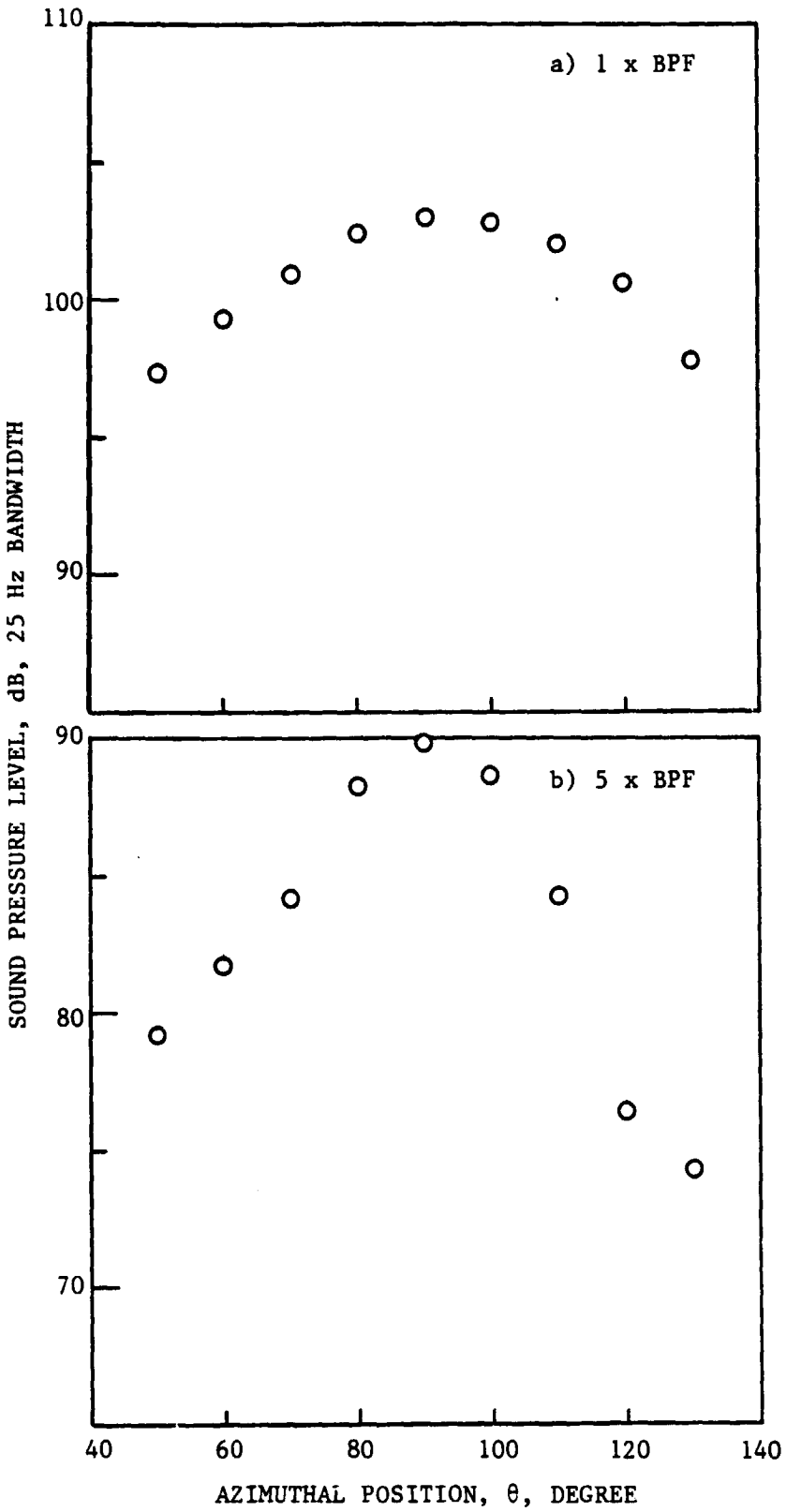

FIG. 46. DIRECTIVITY PATTERN OF BLADE-VORTEX INTERACTION HARMONIC NOISE FOR TEST CONDITION 5 (r_I/R = 0.975, M_T = 0.59, U_∞ = 8.2 m/s).

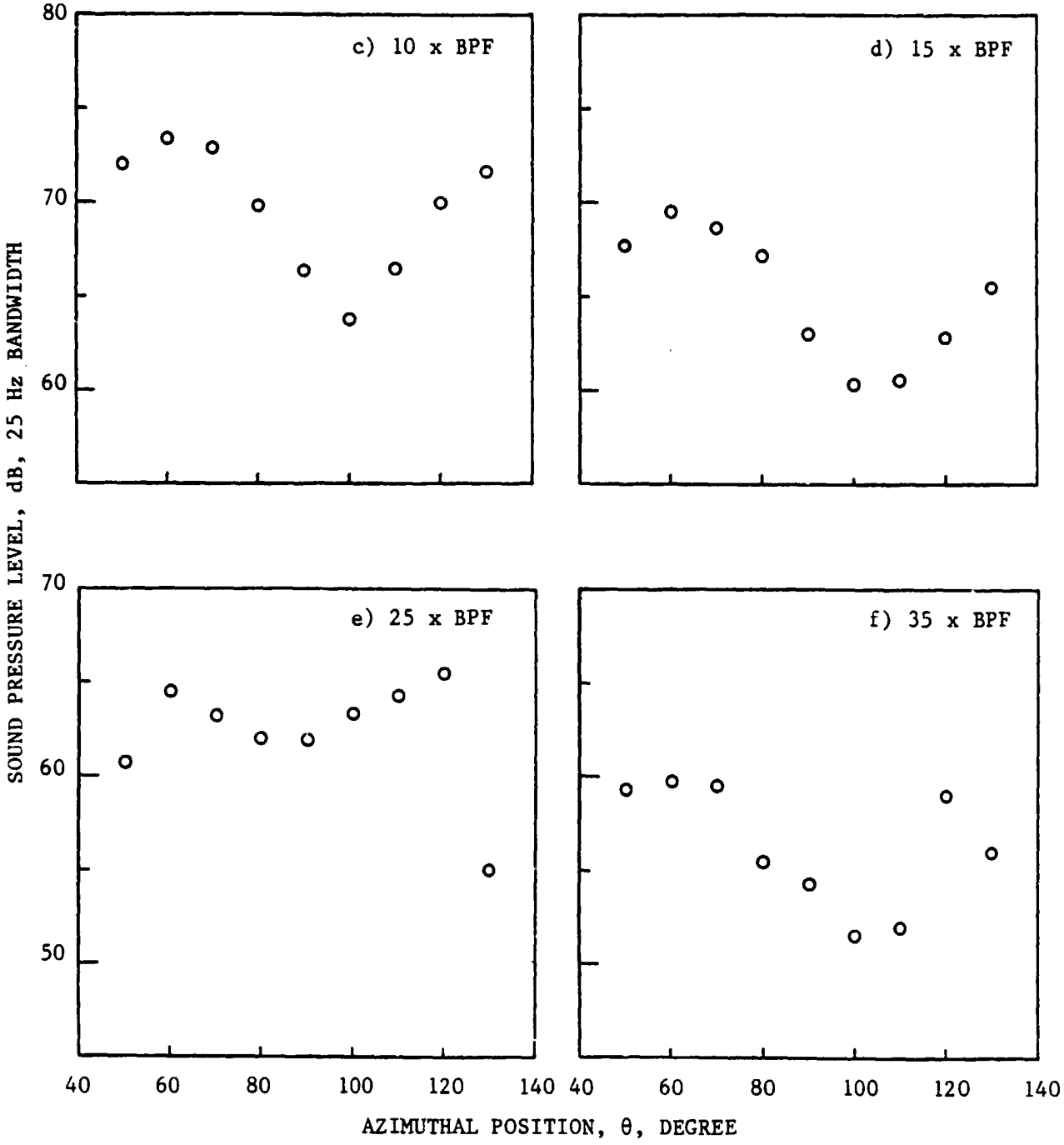
c) 10 x BPF
d) 15 x BPF
e) 25 x BPF
f) 35 x BPF
SOUND PRESSURE LEVEL, dB, 25 Hz BANDWIDTH
AZIMUTHAL POSITION, θ, DEGREE
80
70
60
50
40
60
80
100
120
140

FIG. 46. (CONT'D.).

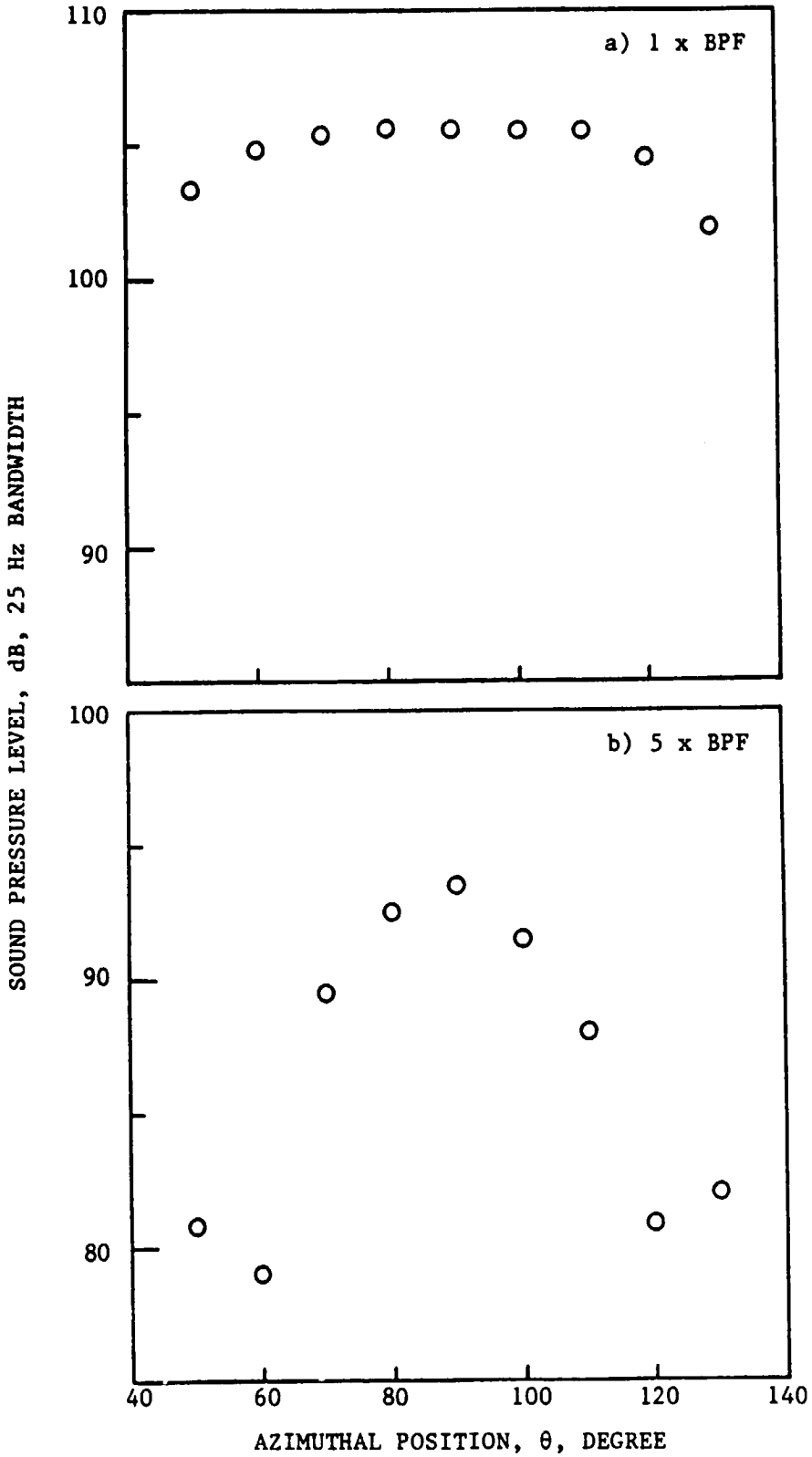

FIG. 47. DIRECTIVITY PATTERN OF BLADE-VORTEX INTERACTION HARMONIC NOISE FOR TEST CONDITION 6 (r_I/R = 0.975, M_T = 0.63, U_∞ = 7.3 m/s). ⚲ DENOTES THAT ACTUAL LEVEL IS SOMEWHAT LOWER THAN INDICATED LEVEL.

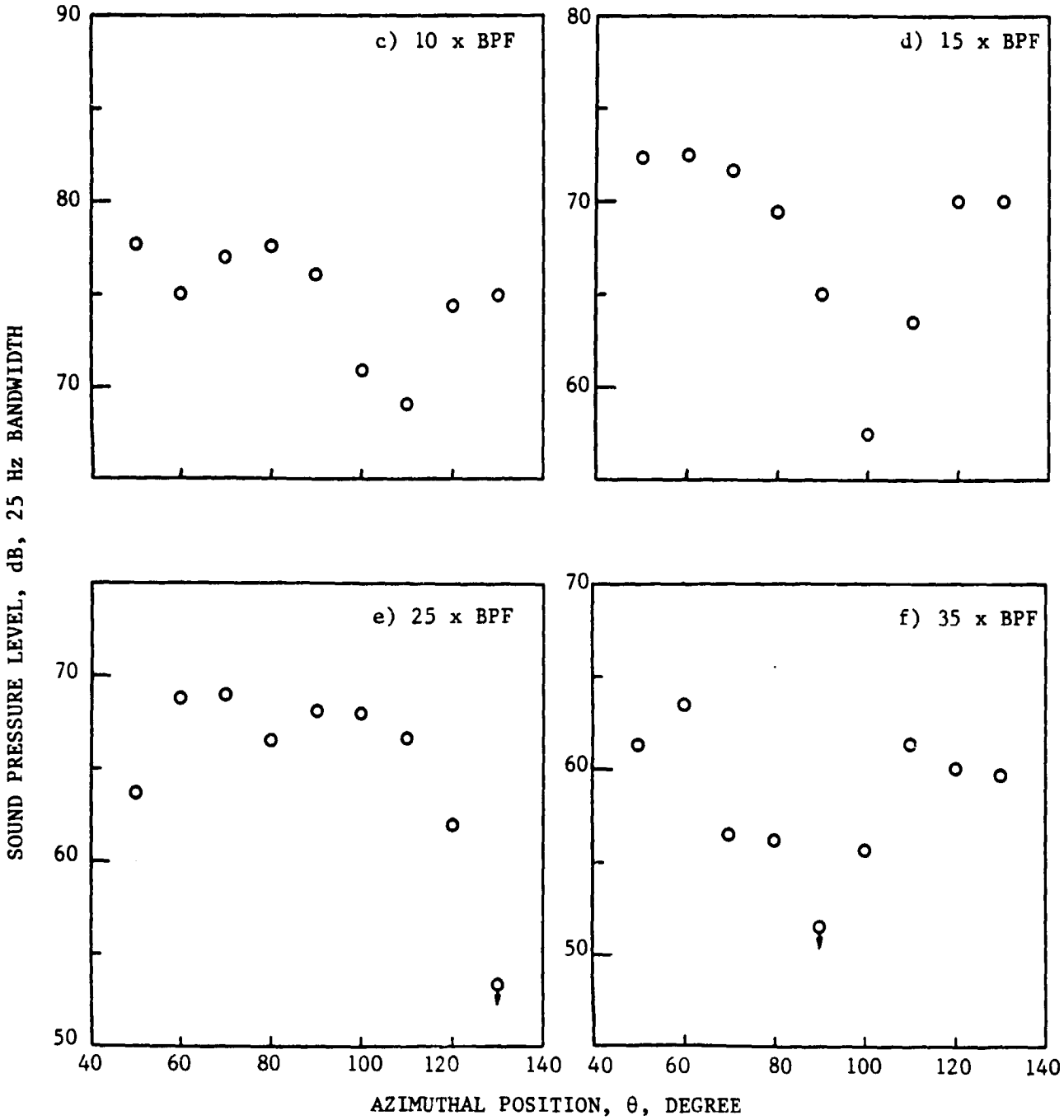
c) 10 x BPF
d) 15 x BPF
e) 25 x BPF
f) 35 x BPF
SOUND PRESSURE LEVEL, dB, 25 Hz BANDWIDTH
AZIMUTHAL POSITION, θ, DEGREE
90
80
70
60
50
40
60
80
100
120
140

FIG. 47. (CONT'D.).

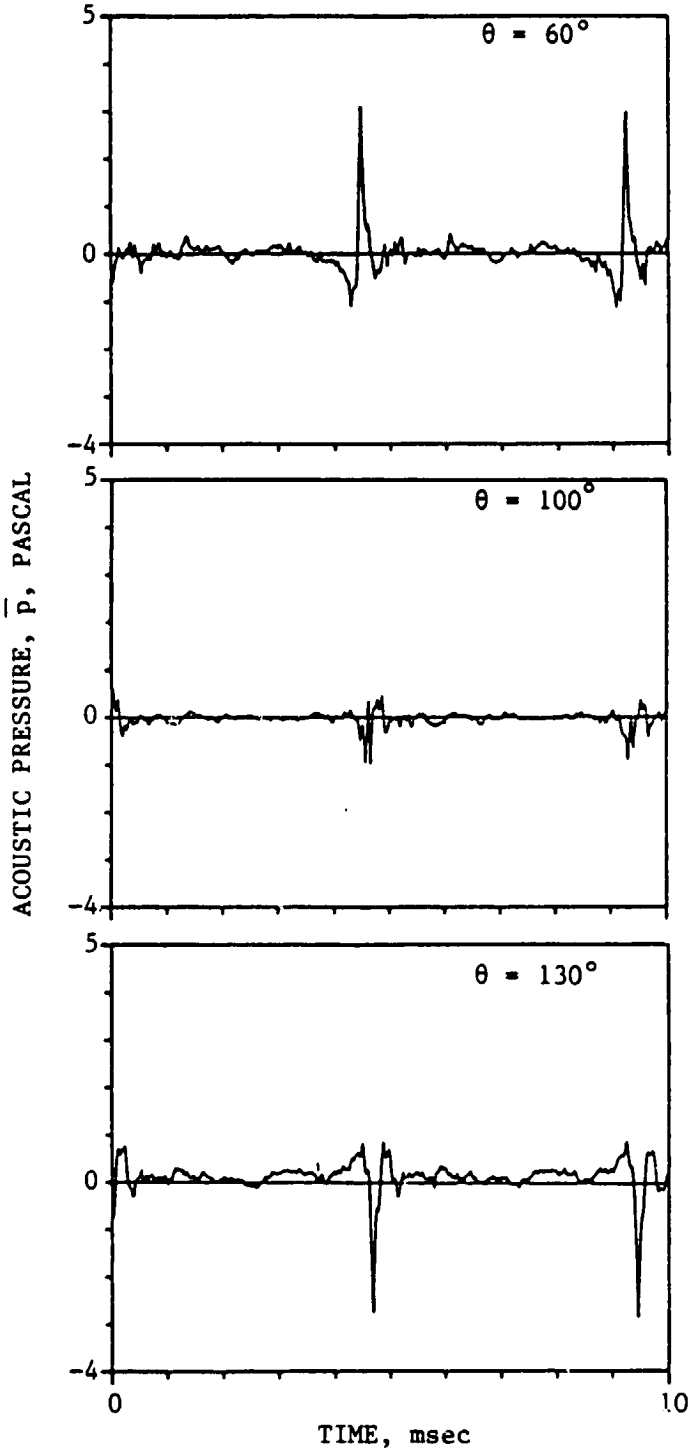

FIG. 48. BVI SIGNATURES FOR THREE DIFFERENT AZIMUTHAL LOCATIONS DISPLAYING THE DIPOLE CHARACTER OF BLADE-VORTEX INTERACTION RADIATION, TEST CONDITION 2 (r_I/R = 0.90, M_T = 0.59, U_∞ = 8.2 m/s).

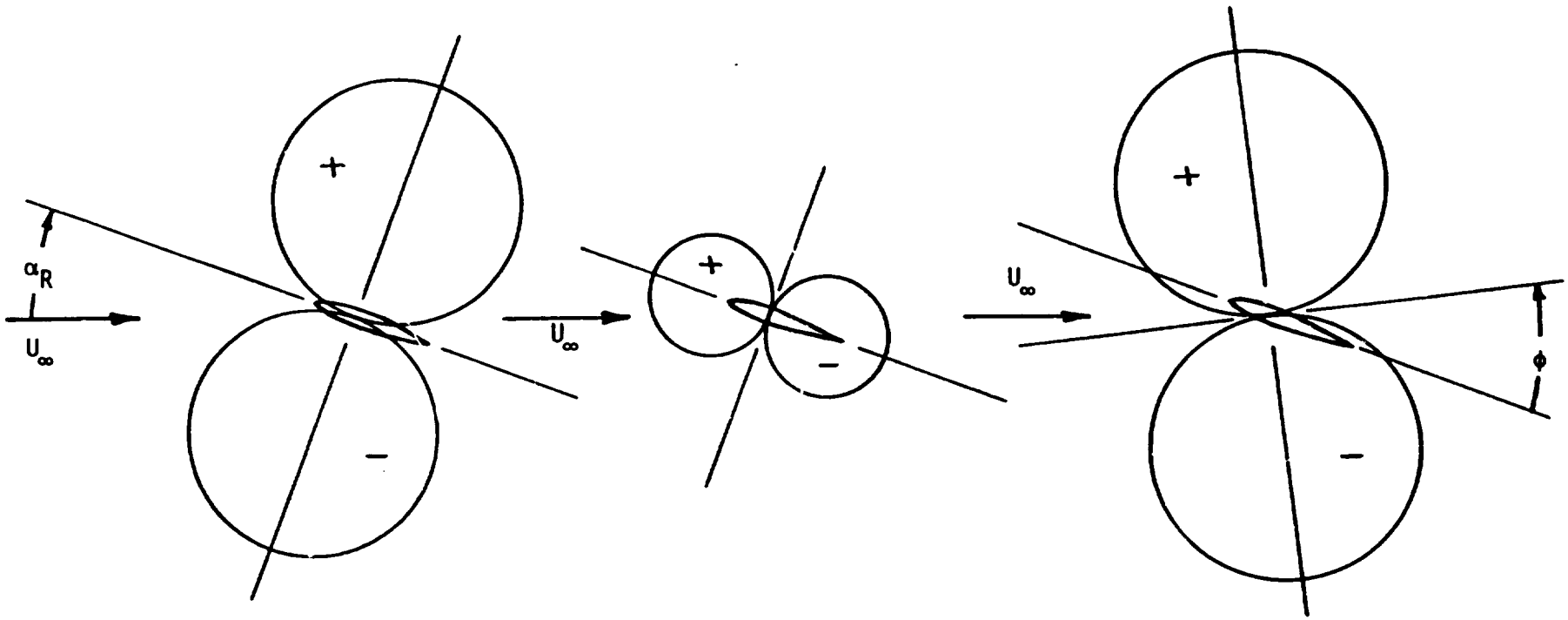

(Unsteady Lift Dipole Radiation) + (Unsteady Drag Dipole Radiation) = (Rotated Dipole Radiation)

FIG. 49. DIAGRAM EXPLAINING THE EFFECT OF UNSTEADY DRAG DIPOLE RADIATION IN SHIFTING THE BLADE-VORTEX INTERACTION DIRECTIVITY PATTERN.

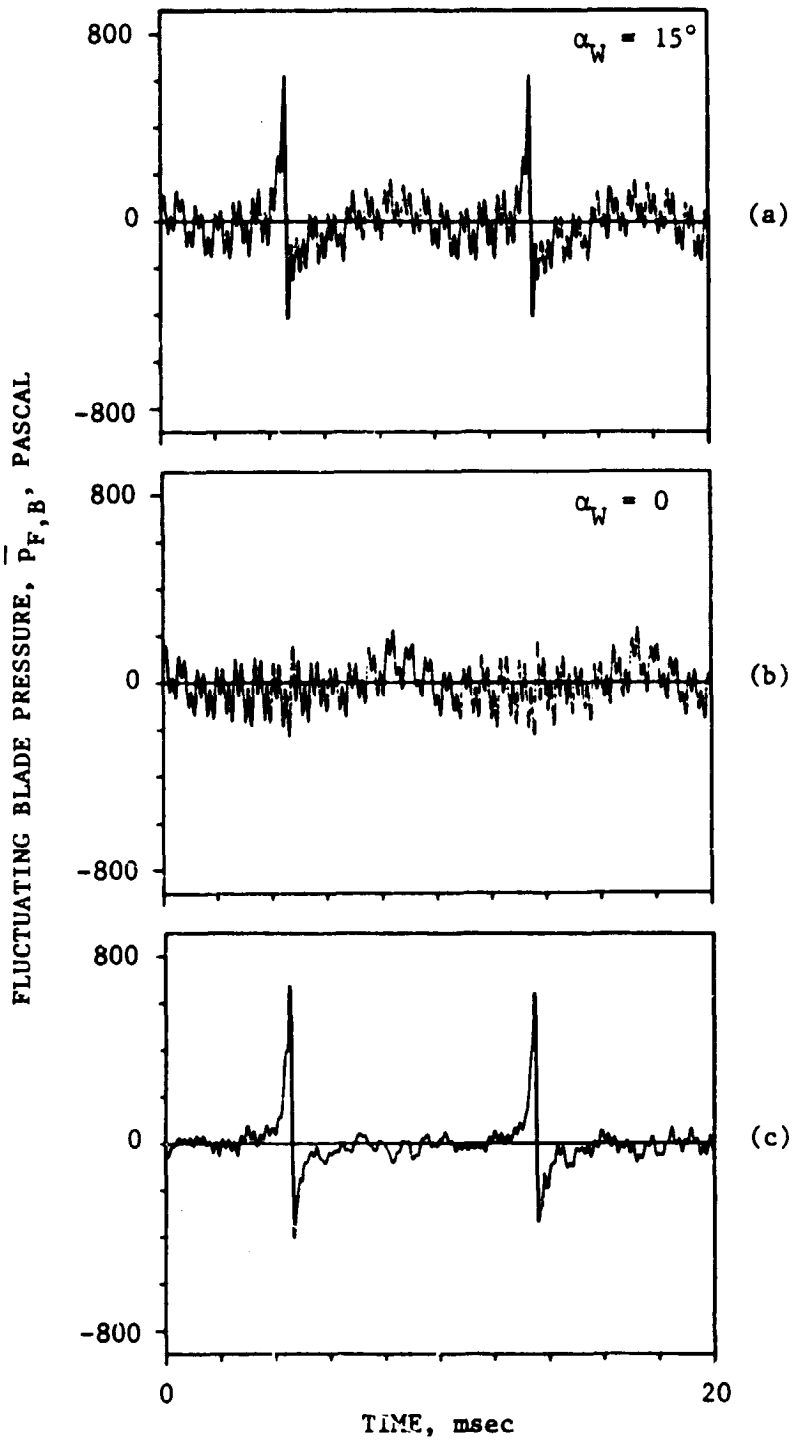

FIG. 50. UNSTEADY BLADE PRESSURE WAVEFORMS (a,b) AND THE NET FLUCTUATING BLADE PRESSURE DUE TO BLADE-VORTEX INTERACTION (c) FOR BMT 1 (r/R = 0.975, PRESSURE SIDE), TEST CONDITION 3 (r_I/R = 0.90, M_T = 0.63, U_∞ = 7.3 m/s).

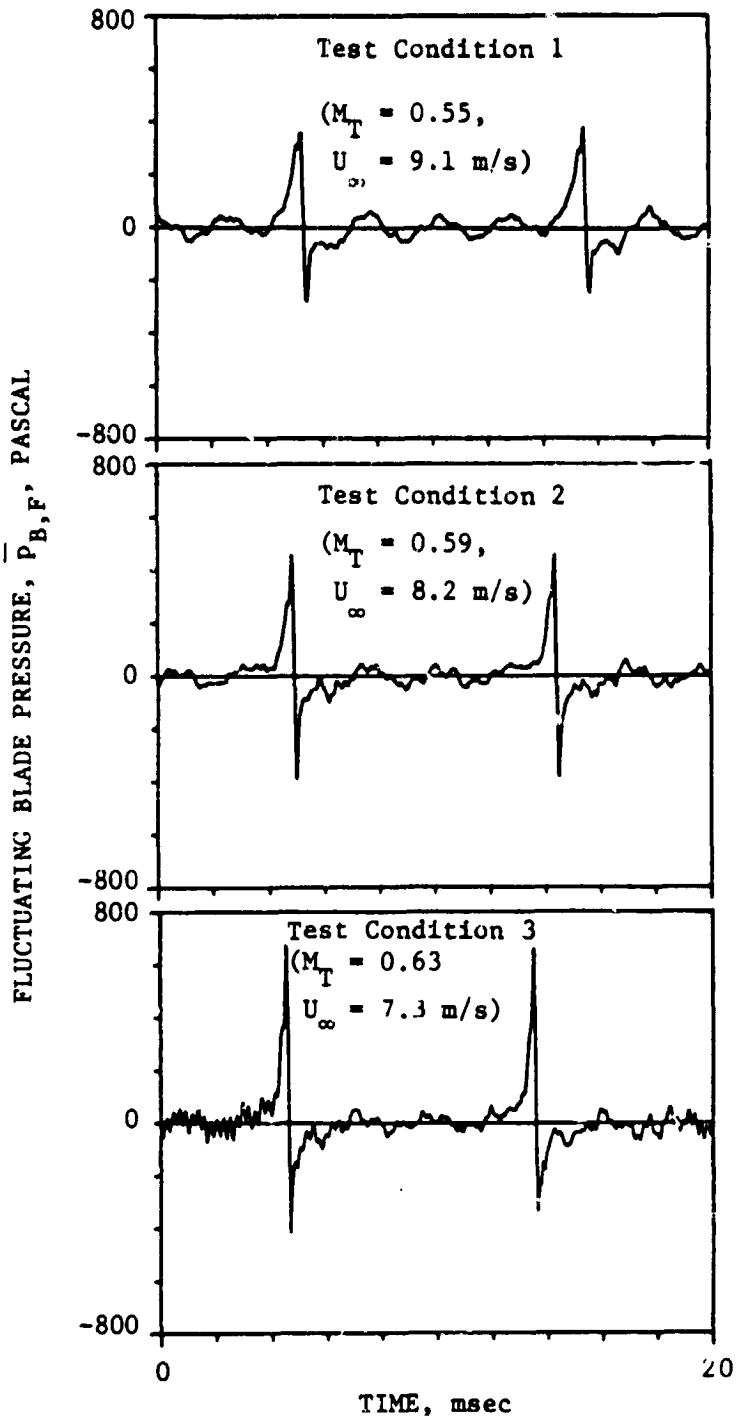

FIG. 51. FLUCTUATING BLADE PRESSURE ATBMT 1 (r/R = 0.975, pressure side) FOR THREE DIFFERENT TEST CONDITIONS, r_I/R = 0.90.

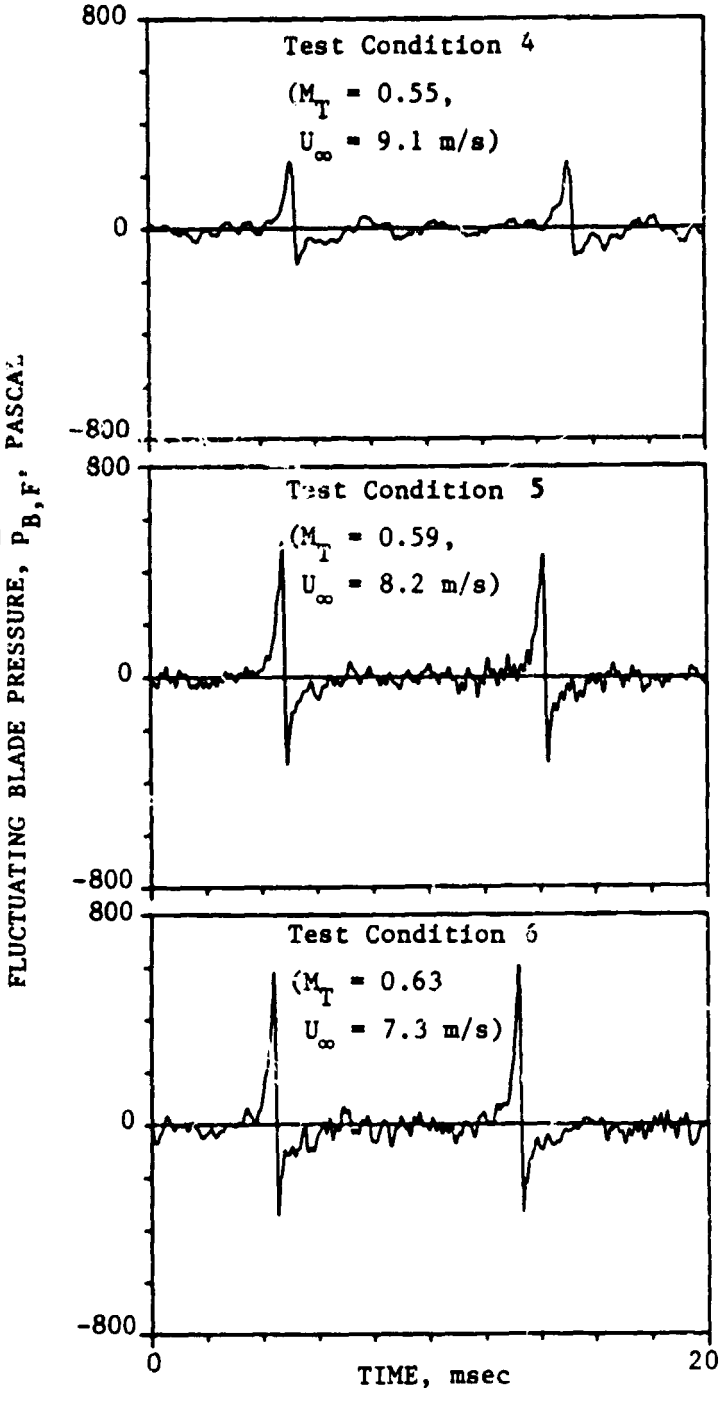

FIG. 52. FLUCTUATING BLADE PRESSURE AT BMT 1 (r/R = 0.975, pressure side) FOR THREE DIFFERENT TEST CONDITIONS, r_I/R = 0.975.

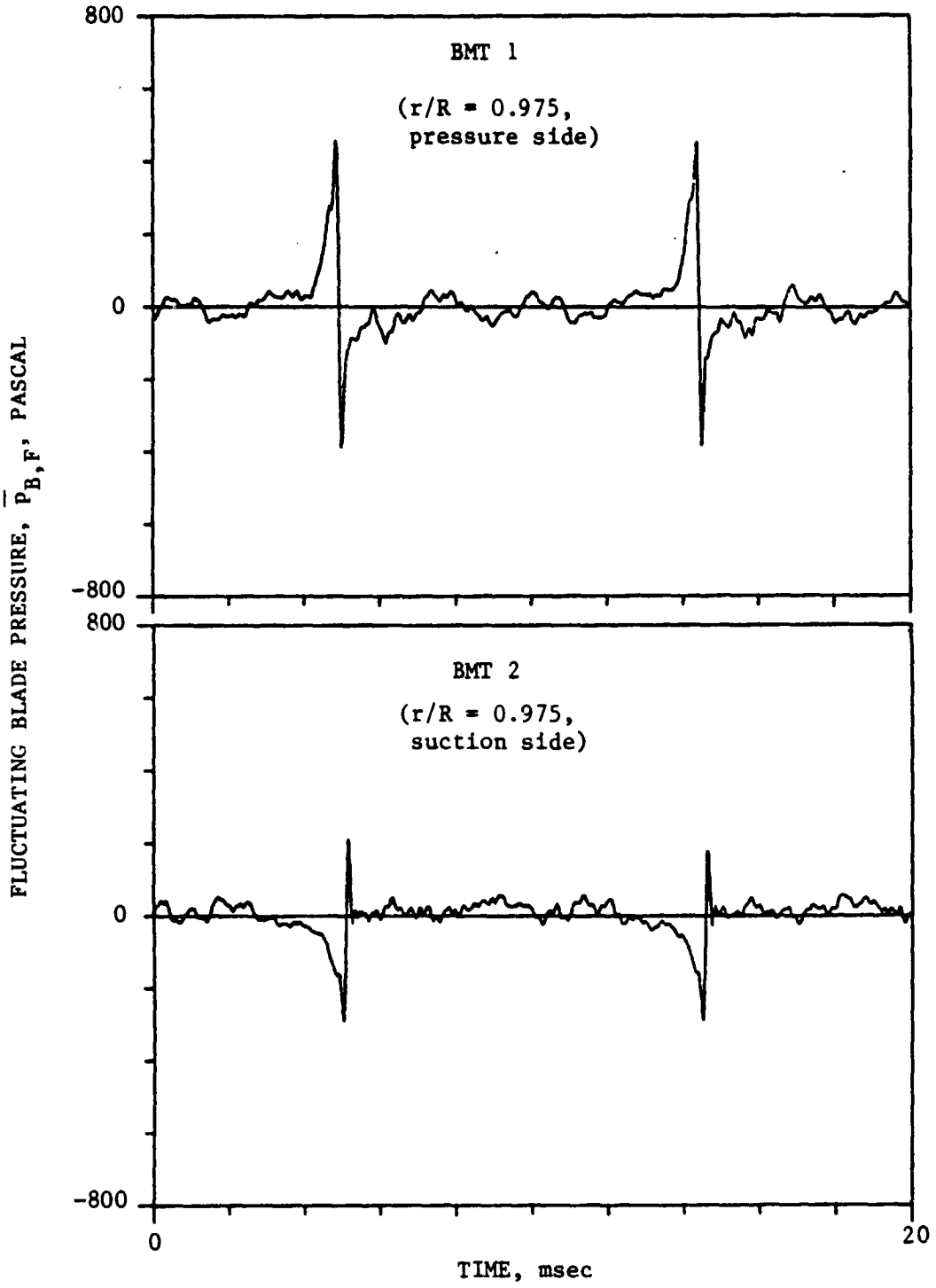

FIG. 53. FLUCTUATING BLADE PRESSURE AT DIFFERENT BMTs FOR TEST CONDITION 2 (r_I/R = 0.90, M_T = 0.59, U_∞ = 8.2 m/s).

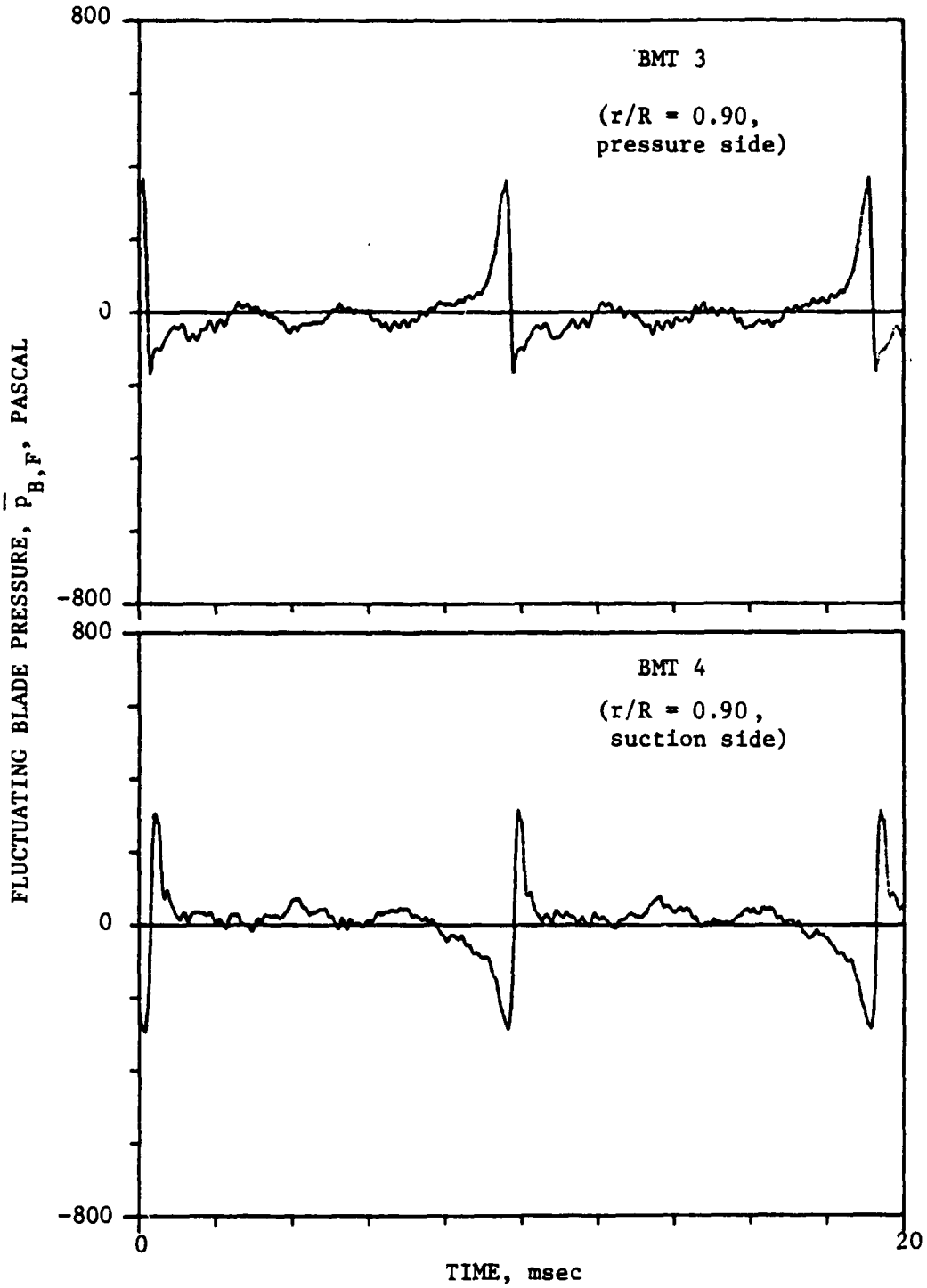
800
BMT 3
(r/R = 0.90,
pressure side)
0
-800
800
BMT 4
(r/R = 0.90,
suction side)
0
-800
0
20
TIME, msec
FLUCTUATING BLADE PRESSURE, $\bar{p}_{B,F}$, PASCAL

FIG. 53. (CONT'D.).

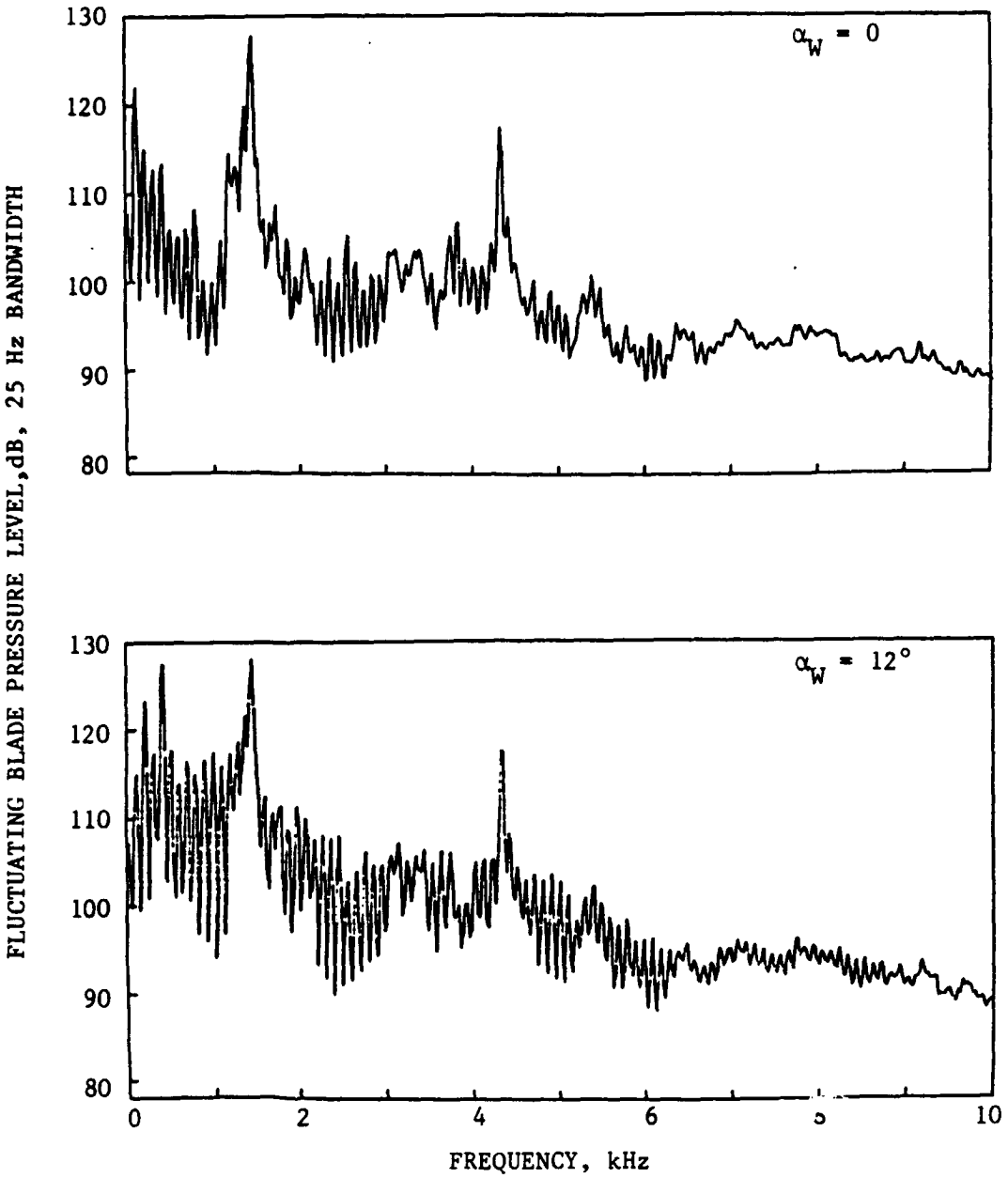

FIG. 54. EFFECT OF BLADE-VORTEX INTERACTION ON FLUCTUATING BLADE PRESSURE SPECTRA FOR TEST CONDITION 1, (r_T/R = 0.90, M_T = 0.55, U_∞ = 9.1 m/s), BMT 1 (r/R = 0.975, pressure side).

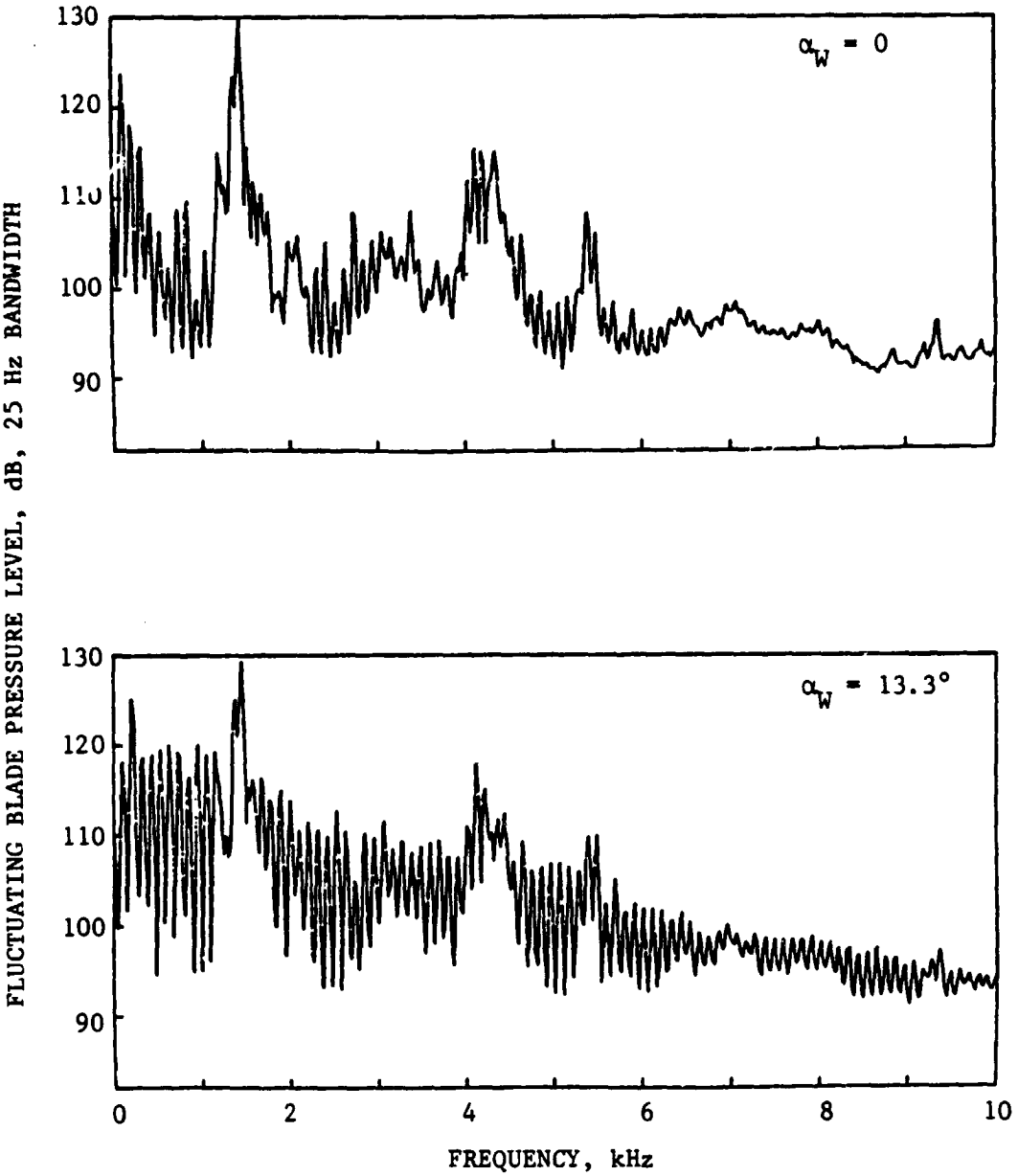

FIG. 55. EFFECT OF BLADE-VORTEX INTERACTION ON FLUCTUATING BLADE PRESSURE SPECTRA FOR TEST CONDITION 2 (r_I/R = 0.90, M_T = 0.59, U_∞ = 8.2 m/s), BMT 1 (r/R = 0.975, pressure side).

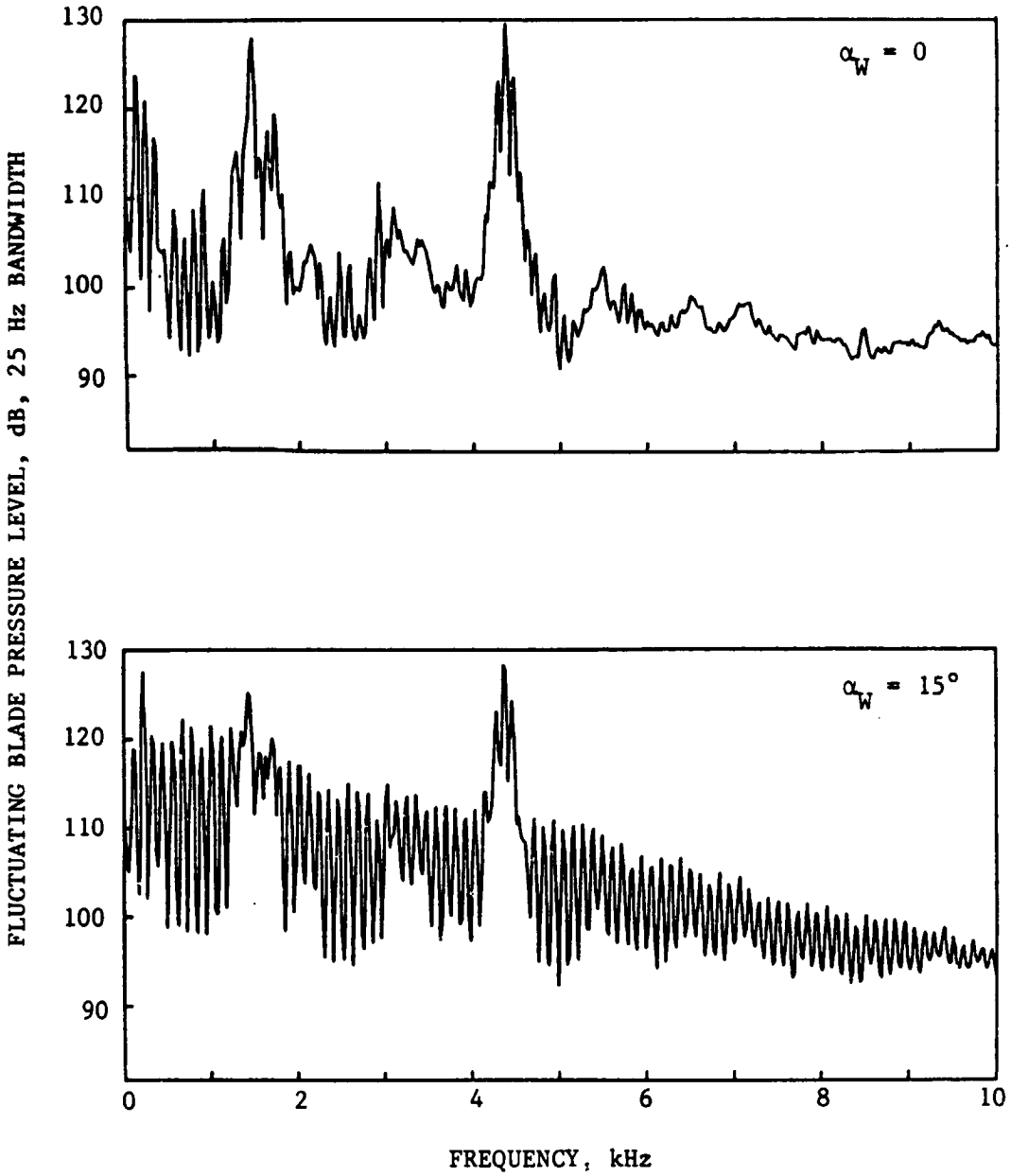

FIG. 56. EFFECT OF BLADE-VORTEX INTERACTION ON FLUCTUATING BLADE PRESSURE SPECTRA FOR TEST CONDITION 3 (r_I/R = 0.90, M_T = 0.63, U_∞ = 7.3 m/s), BMT 1 (r/R = 0.975, pressure side).

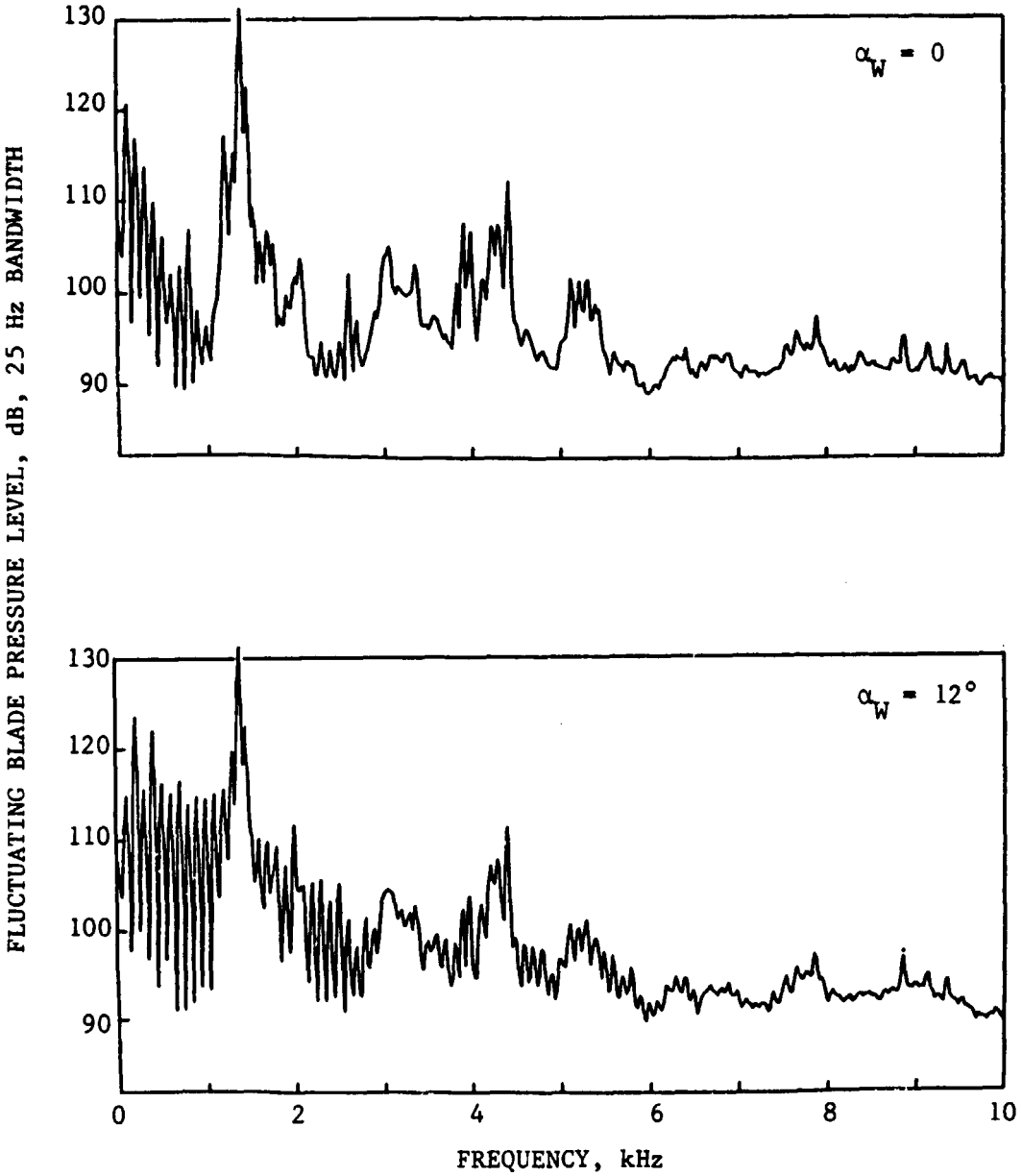

FIG. 57. EFFECT OF BLADE-VORTEX INTERACTION ON FLUCTUATING BLADE PRESSURE SPECTRA FOR TEST CONDITION 4 (r_I/R = 0.975, M_I = 0.55. U_∞ = 9.1 m/s), BMT 1 (r/R = 0.975, pressure side).

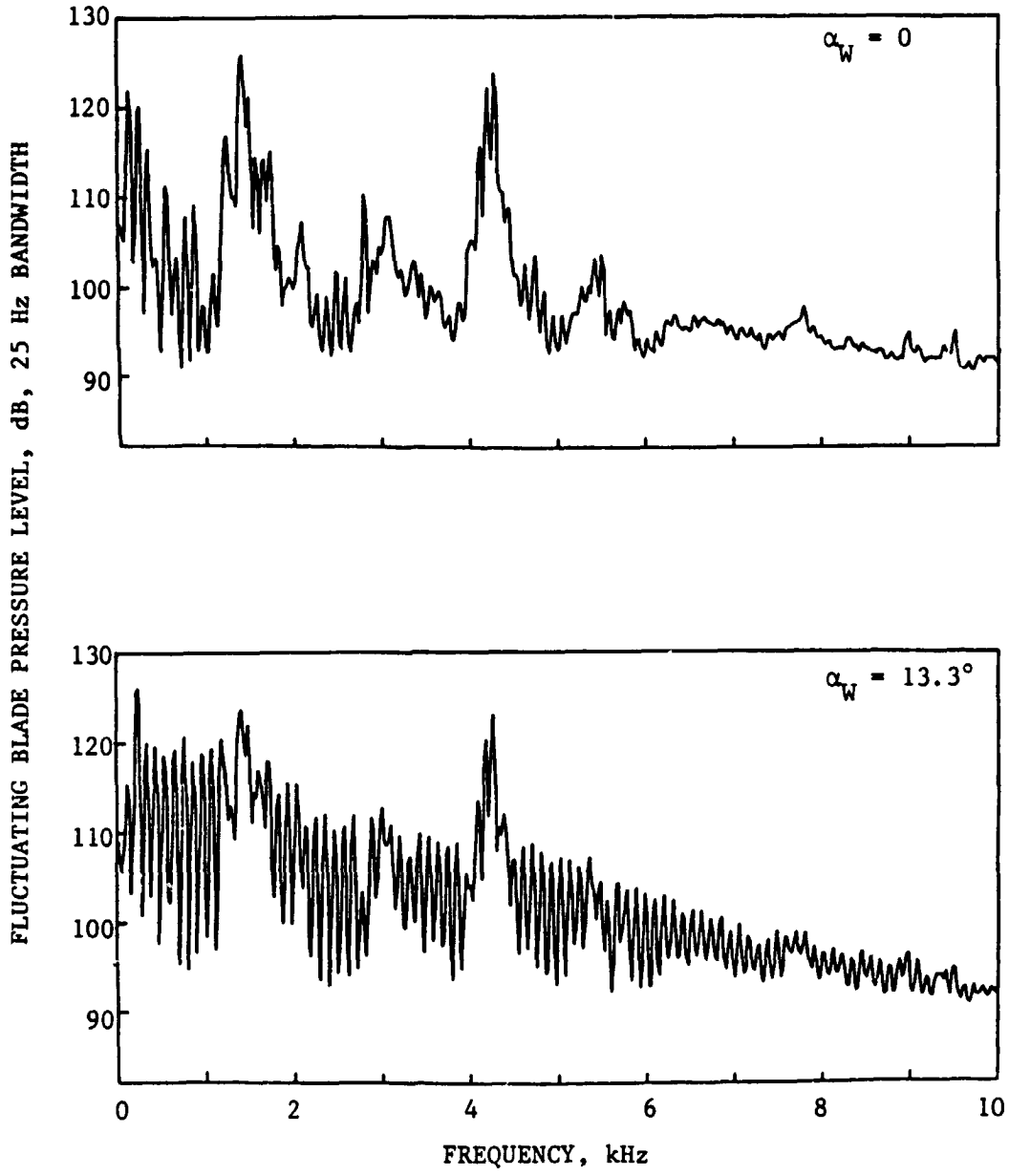

FIG. 58. EFFECT OF BLADE-VORTEX INTERACTION ON FLUCTUATING BLADE PRESSURE SPECTRA FOR TEST CONDITION 5 (r_T/R = 0.975, M_T = 0.59, U_∞ = 8.2 m/s), BMT 1 (r/R = 0.975, pressure side).

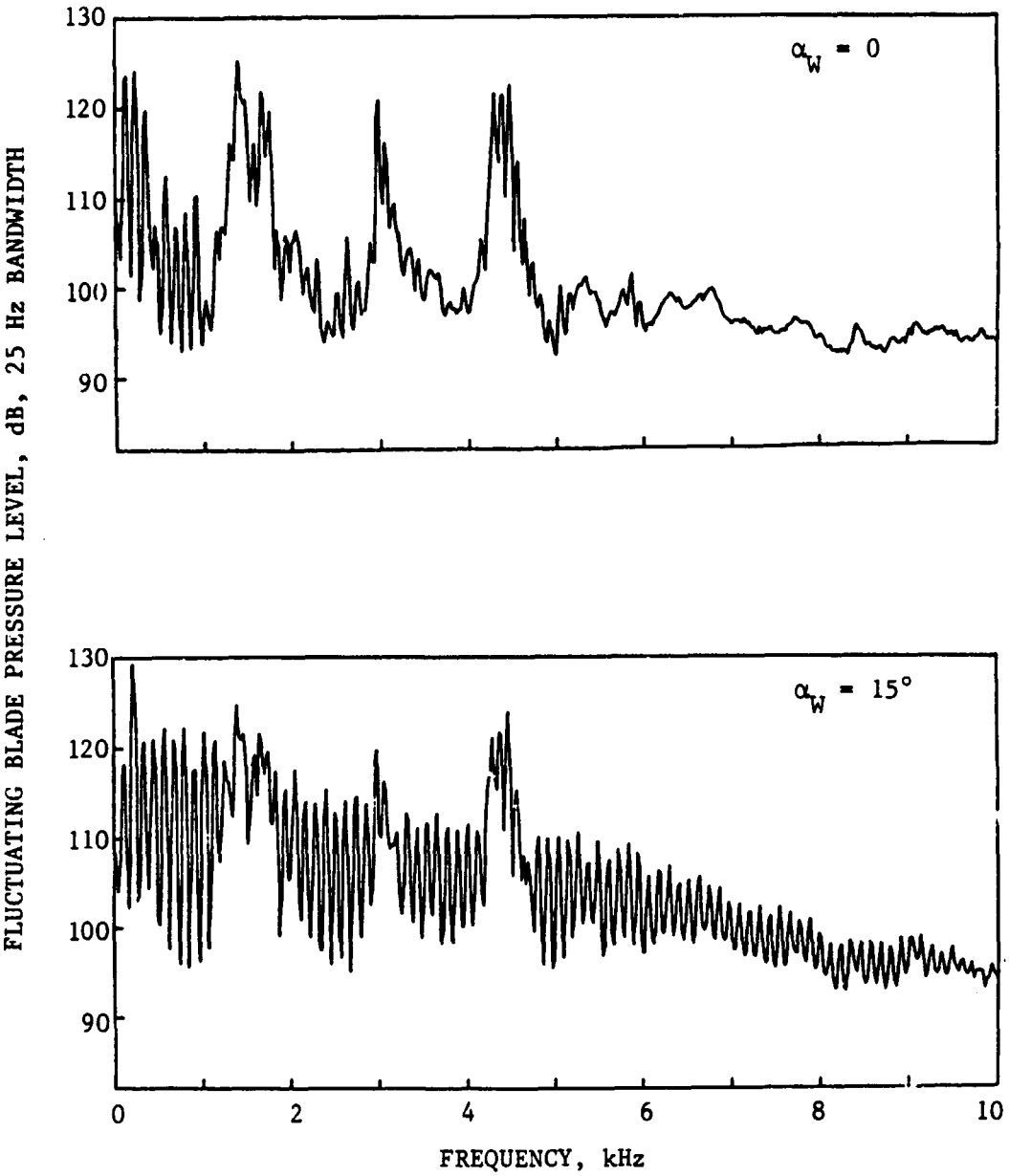

FIG. 59. EFFECT OF BLADE-VORTEX INTERACTION ON FLUCTUATING BLADE PRESSURE SPECTRA FOR TEST CONDITION 6 (r_I/R = 0.975, M_T = 0.63, U_∞ = 7.3 m/s), BMT 1 (r/R = 0.975, pressure side),

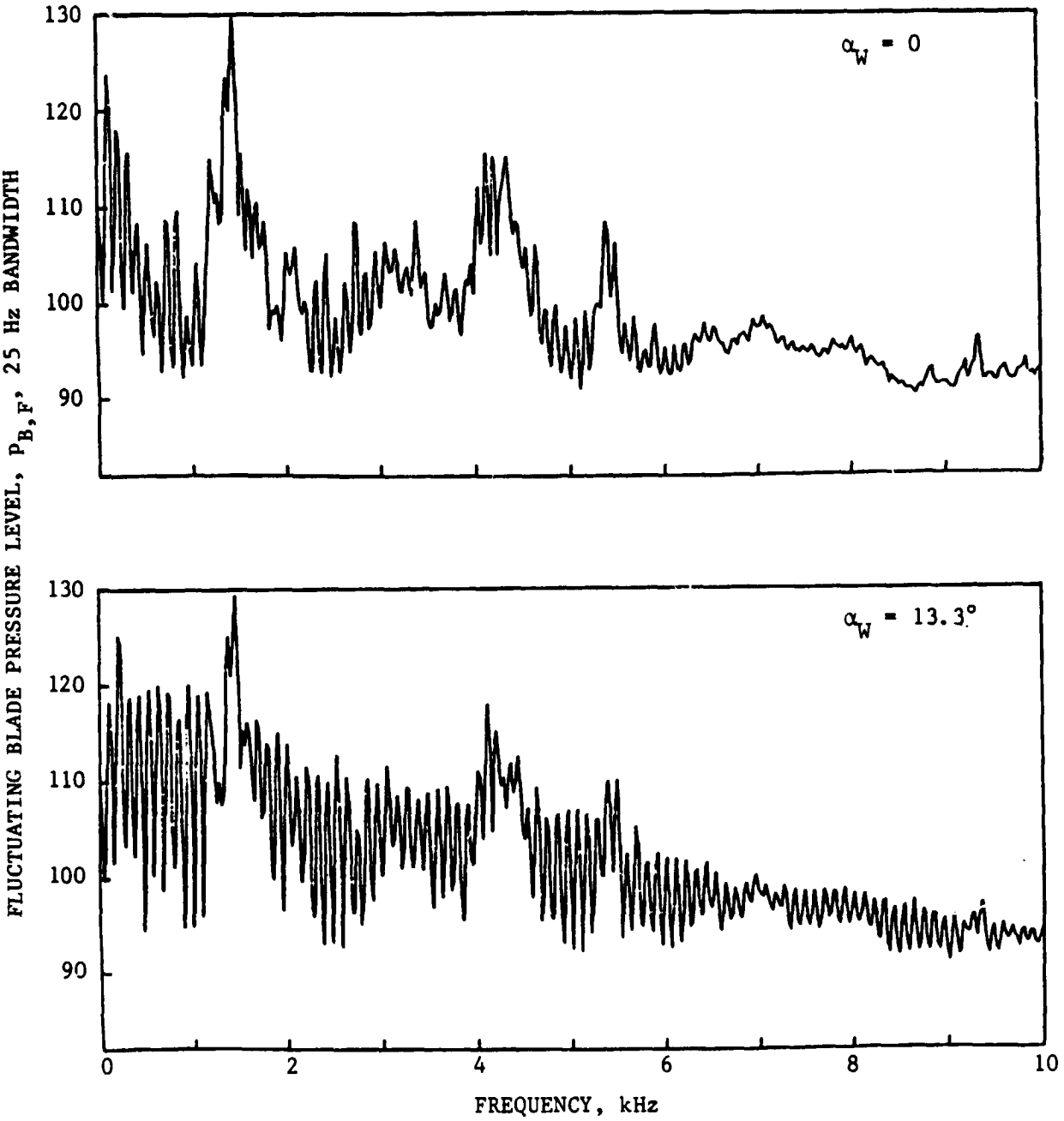

FIG. 60. EFFECT OF BLADE-VORTEX INTERACTION ON FLUCTUATING BLADE PRESSURE SPECTRA FOR TEST CONDITION 2 (r_L/R = 0.90, M_T = 0.59, U_∞ = 8.2 m/s), BMT 1 (r/R = 0.975, pressure side).

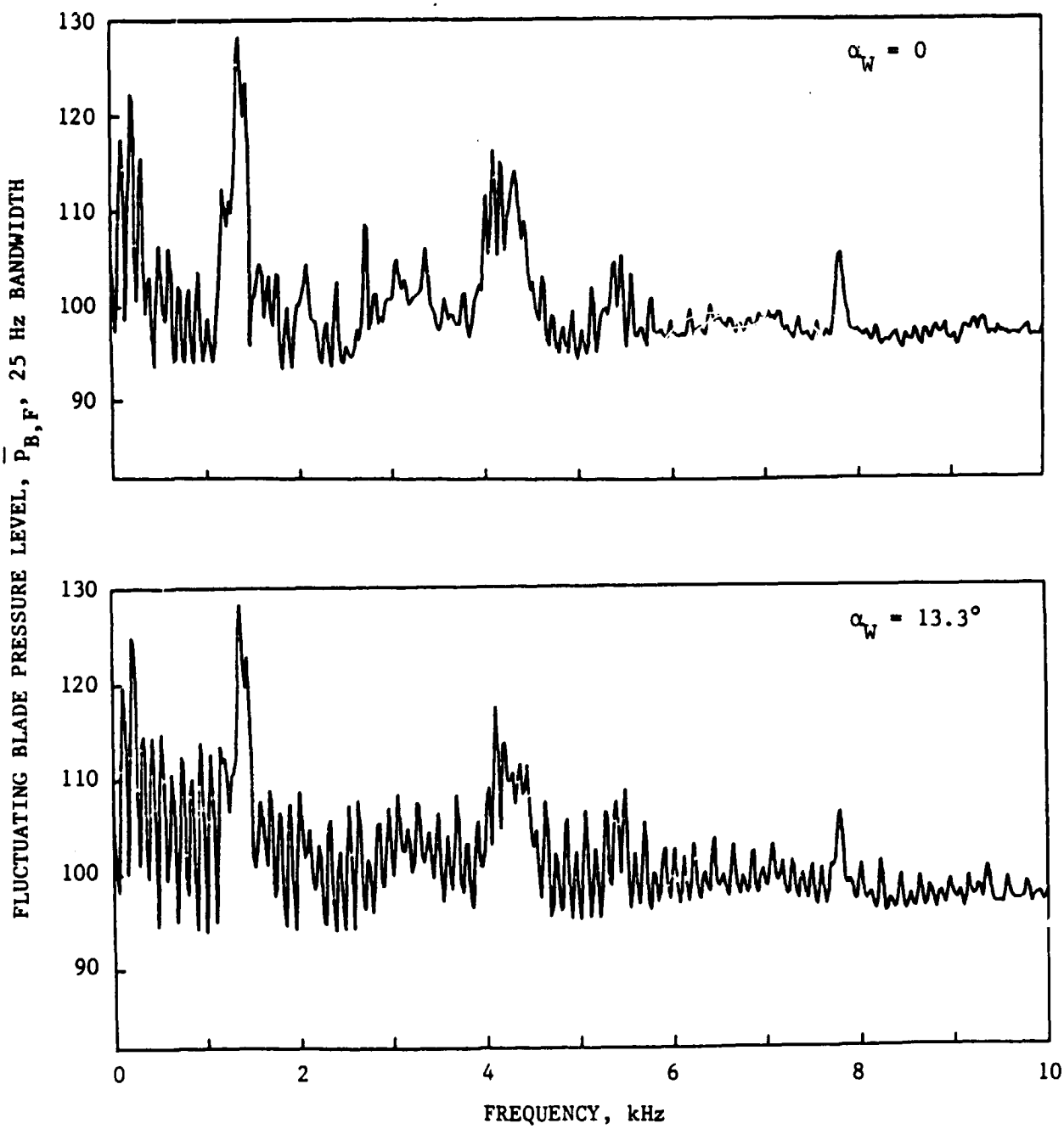

FIG. 61. EFFECT OF BLADE-VORTEX INTERACTION ON FLUCTUATING BLADE PRESSURE SPECTRA FOR TEST CONDITION 2 (r_I/R = 0.90, M_T = 0.59, U_∞ = 8.2 m/s), BMT 2 (r/R = 0.975, suction side).

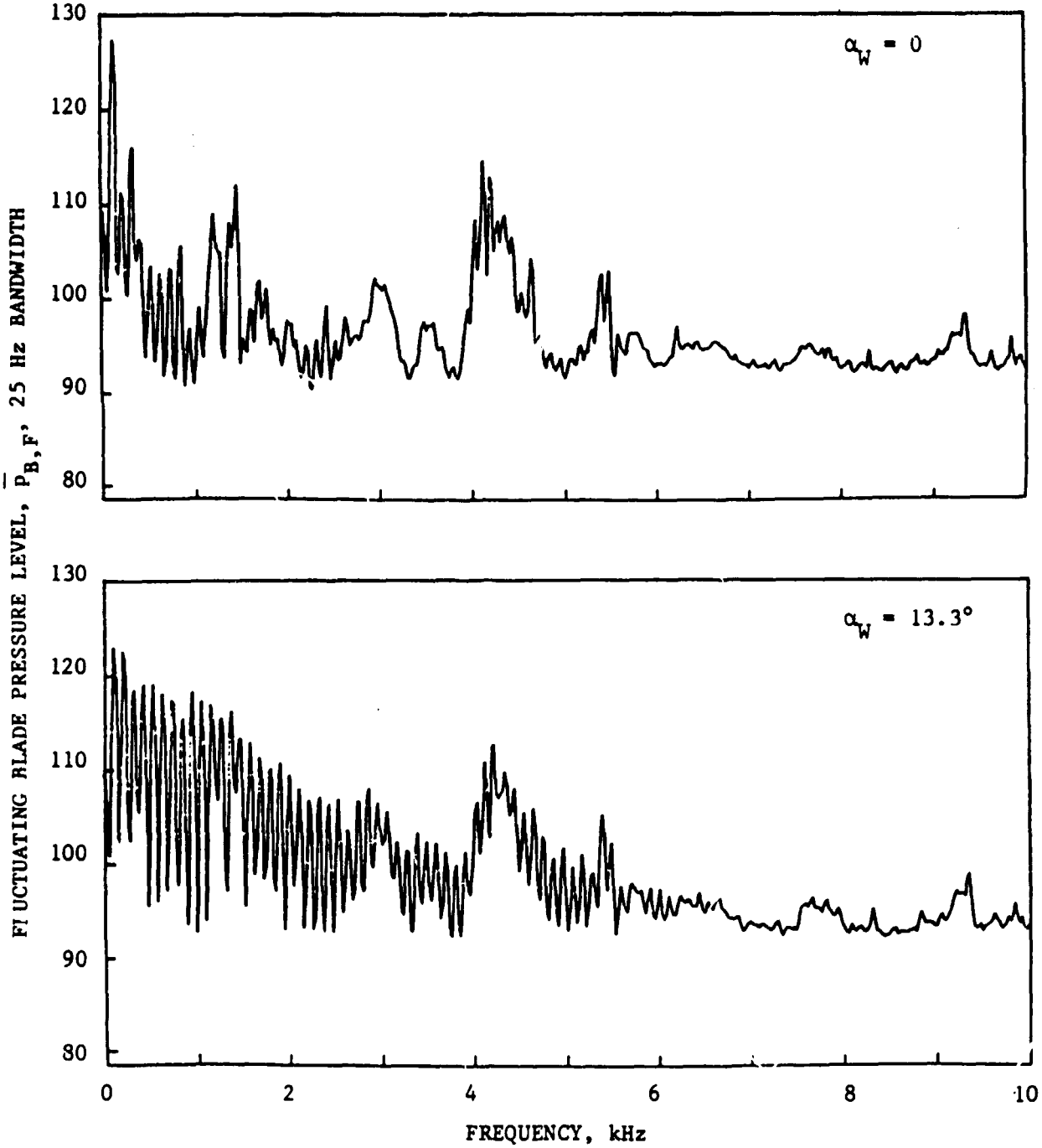

FIG. 62. EFFECT OF BLADE-VORTEX INTERACTION ON FLUCTUATING BLADE PRESSURE SPECTRA FOR TEST CONDITION 2 (r_I/R = 0.90, M_T = 0.59, U_∞ = 8.2 m/s), BMT 3 (r/R = 0.90, pressure side).

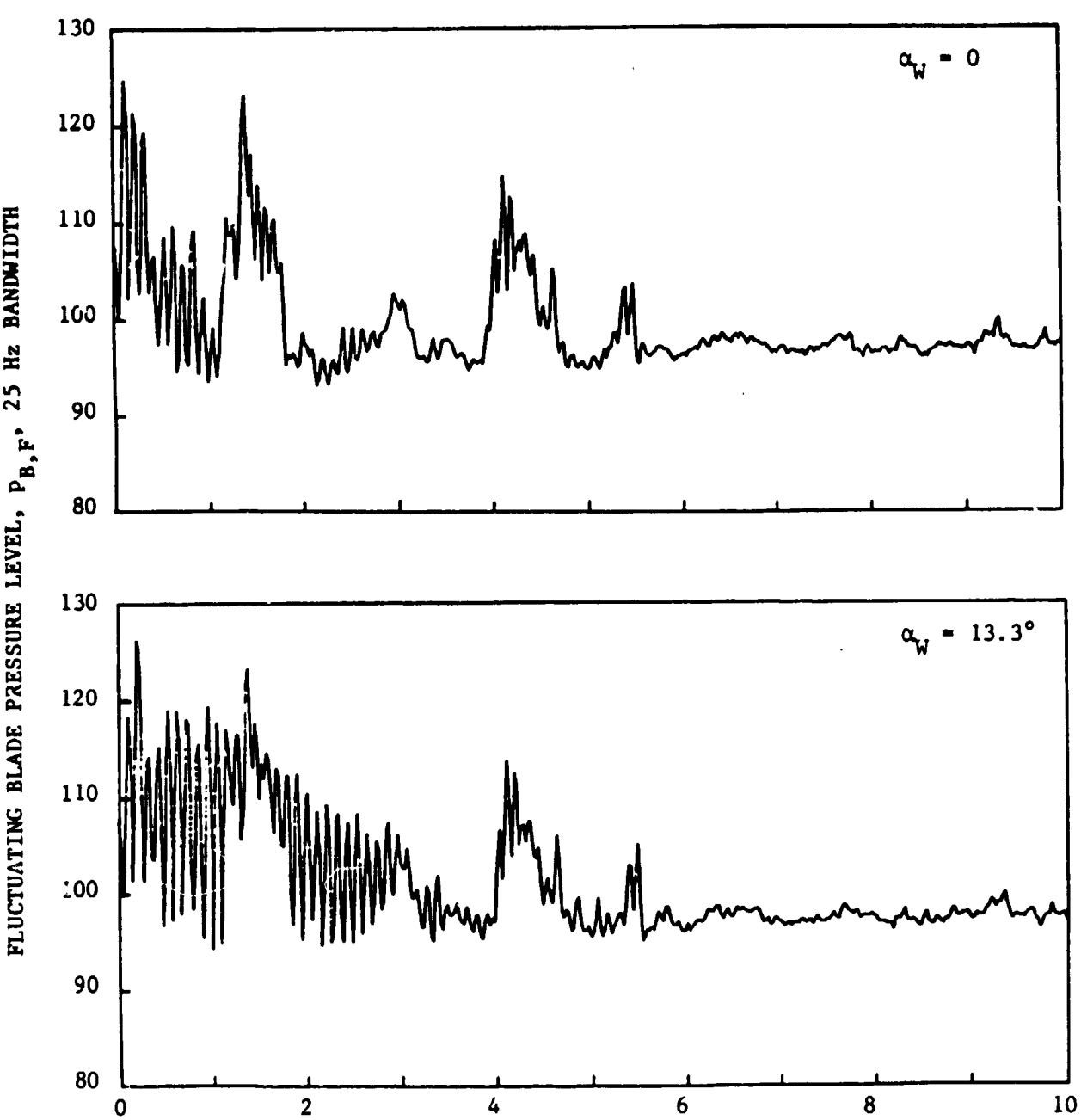

FIG. 63. EFFECT OF BLADE-VORTEX INTERACTION ON FLUCTUATING BLADE PRESSURE SPECTRA FOR TEST CONDITION 2 (r_I/R = 0.90, M_T = 0.59, U_∞ = 8.2 m/s), BMT 4 (r/R = 0.90, suction side).